Australian Government
Bureau of Meteorology

The Centre for Australian Weather and Climate Research
A partnership between CSIRO and the Bureau of Meteorology

CSIRO

Ocean Model, Analysis and Prediction System: version 2

G.B. Brassington, J. Freeman, X. Huang, T. Pugh, P.R. Oke, P.A. Sandery, A. Taylor, I. Andreu-Burillo, A. Schiller, D.A. Griffin, R. Fiedler, J. Mansbridge, H. Beggs and C.M. Spillman

CAWCR Technical Report No. 052

April 2012

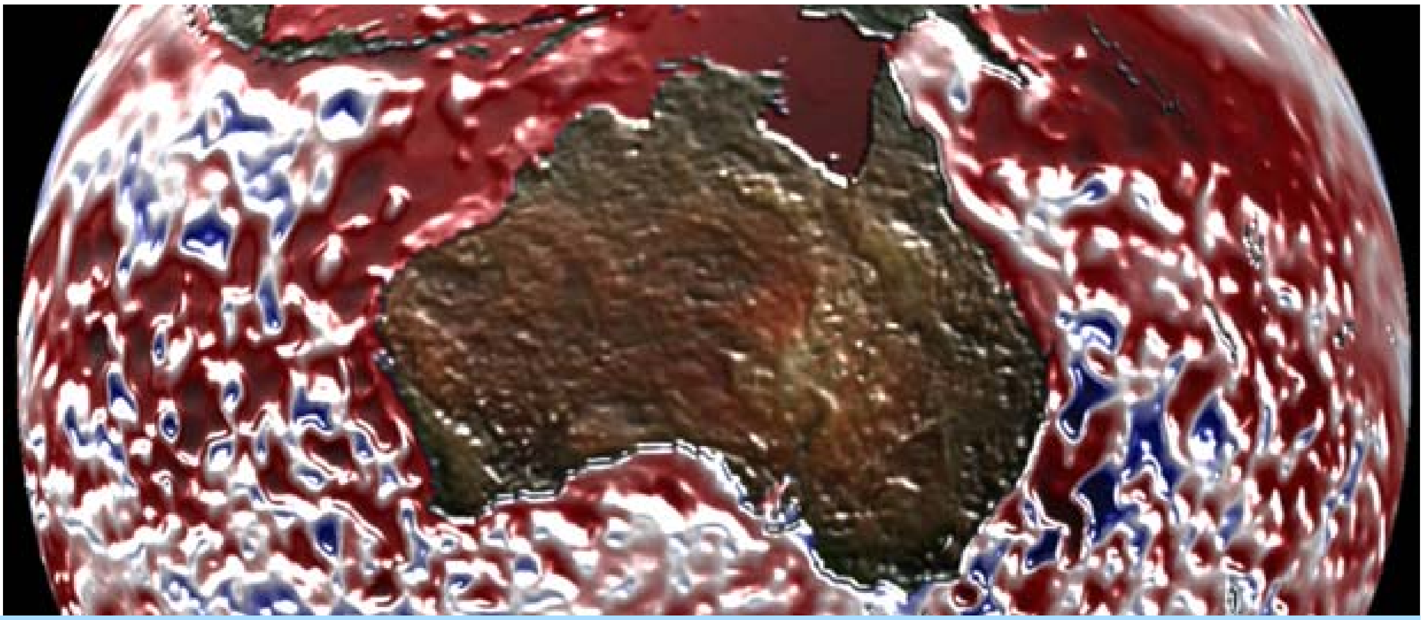

www.cawcr.gov.au

Ocean Model, Analysis and Prediction System: version 2

G.B. Brassington, J. Freeman, X. Huang, T. Pugh, P.R. Oke, P.A. Sandery, A. Taylor, I. Andreu-Burillo, A. Schiller, D.A. Griffin, R. Fiedler, J. Mansbridge, H. Beggs and C.M. Spillman

The Centre for Australian Weather and Climate Research
- a partnership between CSIRO and the Bureau of Meteorology

CAWCR Technical Report No. 052

April 2012

ISSN: 1836-019X

National Library of Australia Cataloguing-in-Publication entry

Author: G.B. Brassington, J. Freeman, X. Huang, T. Pugh, P.R. Oke, P.A. Sandery, A. Taylor, I. Andreu-Burillo, A. Schiller, D.A. Griffin, R. Fiedler, J. Mansbridge, H. Beggs and C.M. Spillman

Title: Ocean Model, Analysis and Prediction System: version 2

ISBN: 978 0 643 10843 1 (Electronic Resource)

Series: CAWCR technical report; 52

Subjects:

Notes: Included bibliography references and index

Other Authors / Contributors: Day, K.A. (Editor)

Enquiries should be addressed to:
Dr Gary Brassington
Centre for Australian Weather and Climate Research:
A partnership between the Bureau of Meteorology and CSIRO
GPO Box 1289, Melbourne
Victoria 3001, Australia

g.brassington@bom.gov.au

Copyright and Disclaimer

Cover image: Sea level anomaly for the 20th January 2012 over the Australian region from the analysis cycle of the OceanMAPSv2. (J. Freeman)

Contents

List of Figures

List of Tables

ABBREVIATIONS AND SYMBOLS

Table 1 Abbreviations and Symbols

AATSR	Advanced along-track scanning radiometer
aCC	Anomaly Cross-Correlation coefficient
ACC	Antarctic Circumpolar Current, a eastward transport in the Southern Ocean that is circumpolar.
ACCESS	Australian Community Climate and Earth System Simulator which represents a range of common model software for use in short-range to climate earth simulations by CAWCR. In the context of OceanMAPS ACCESS refers to an operational NWP system at Bureau of Meteorology, ACCESS-G represents the global NWP system. The system is based on the UK Met Office unified model and 4DVar data assimilation system.
AMSR-E	Advanced microwave scanning radiometer for EOS (EOS is earth observing system)
Argo	A global array of Autonomous profiling floats
AVHRR	Advanced very high resolution radiometer
BATHY	Bathythermal observation report, a message convention used on the GTS to transit CTD messages from Argo, moorings etc.
BLUElink / Bluelink	A joint research project between the Bureau of Meteorology, CSIRO and the Royal Australian Navy to develop operational ocean forecasting systems for Australia
BODAS	Bluelink Ocean Data Assimilation System, BODAS1 (version 1), BODAS2 (version 2)
BRAN	Bluelink Re-Analysis Project
BRT	Behind real-time, a 9-day behind real-time analysis cycle that uses a symmetric window of altimetry observations
CAWCR	Centre for Australian Weather and Climate Research
CF	The climate and forecast metadata convention maintained at the Lawrence Livermore National Laboratory. A community accepted set of variable name and definitions that extends COARDS conventions. <http://cf-pcmdi.llnl.gov>

CNES	Centre National d'Etudes Spatiales
CSIRO	Commonwealth Scientific and Industry Research Organisation
DAC	Data assembly centre, a national data management for Argo data
EAC	East Australian Current, a poleward boundary current along the east coast of Australia
ECMWF	European Centre for Medium-Range Weather Forecasts
Envisat	ESA's successor to the ERS carrying AATSR and altimetry
ERA	ECMWF ReAnalysis which reconstructs the global atmosphere. There are several reanalyses, ERA-40 and ERA-interim which is routinely updated
ESA	European Space Agency
FGAT	First-guess at appropriate time, a technique used in 3DVar to compute innovations at the time of the observation.
FOAM	Forecast ocean assimilation model
GASP	NWP system operational at Bureau of Meteorology across the study period
GDAC	Global data assembly centre, used to collate together Argo data from all DACs
GDR	Geophysical data record, a reference used in satellite altimetry
GFDL	Geophysical Fluid Dynamics Laboratory
GHRSST	Group for high resolution sea surface temperature, <https://www.ghrsst.org>
GODAE	Global Ocean Data Assimilation Experiment, an international experiment to coordinate the development of ocean prediction systems based on satellite altimetry. GODAE concluded in 2008 and was summarised in a special issue in Oceanography (see e.g., Dombrowsky et al., 2009)
GOV	GODAE OceanView, a follow-on science team to GODAE to continue international coordination of ocean forecasting, <https://www.godae-oceanview.org/>
GTS	Global Telecommunication System - a WMO communication system used to distribute real-time observations

HYCOM	Hybrid coordinate ocean model
IDL	Interactive data language
IGDR	Interim GDR, a near real-time estimate
Jason	A series of satellite altimeters that maintain a continuous record of climate quality measurements of ocean sea level following the Topex/Poseidon mission. Jason-1 launched in 2001 (maneuvered into an interleaved tandem orbit in 2009 following the tandem calibration of Jason-2), Jason-2 launched
L2P	Level-2 pre-processed GHRSST metadata rich format, for satellite SST data following CF conventions
LC	Leeuwin Current, a poleward ocean boundary current located along the west cost of Australia
MOM4	Modular Ocean Model version 4
NAVOCEANO	Naval Oceanographic Office
NetCDF	Network Common Data Form, is a set of software interfaces for self-describing, array-oriented data access (http://www.unidata.ucar.edu/software/netcdf/)
NCODA	Navy coupled ocean data assimilation
NOAA	National Oceanic and Atmospheric Administration
NRT	Near real-time, a 5-day behind real-time analysis cycle performed with an asymmetric window of altimetry observations
NWP	Numerical Weather Prediction
OceanMAPS	Ocean Model, Analysis and Prediction System: OceanMAPSv1 (version 1.0), OceanMAPSv2 (version 2.0)
OFAM	Ocean Forecast Australia Model, OFAM1 (version 1), OFAM2 (version 2)
OGCM	Oceanic General Circulation Model
OMv1, OMv2	OceanMAPSv1, OceanMAPSv2 respectively
OPeNDAP	Open-source Project for a Network Data Access Protocol

QC	Quality Control
RMSE	Root Mean Square Error
SEC	South Equatorial Current
SLA	Sea Level Anomaly, (see SSH)
SLP	Sea Level Atmospheric Pressure
SPCZ	South Pacific Convergence Zone
SSH	Sea surface height (or sea surface height above sea level)
SST	Sea Surface Temperature, a range of definitions for SST dependent on the instrumentation and diurnal effects (refer to <https://www.ghrsst.org/ghrsst-science/sst-definitions/>)
TAO/TRITON	Tropical Atmosphere Ocean/Triangle Trans-Ocean buoy Network, an array of mooring located along the Pacific equatorial wave guide.
TESAC	Temperature, Salinity, Current report, a message convention used on the GTS to transit CTD messages from Argo, moorings etc.
USGODAE	A data server that hosts one of the Argo GDAC's and other products used by GODAE systems
XBT	eXpendable BathyThermograph, an instrument used to profile the oceans temperature stratification.

1. ABSTRACT

The Bureau of Meteorology established operational ocean forecasting in August 2007 through the Ocean Model, Analysis and Prediction System (OceanMAPS). OceanMAPS was developed through the BLUElink project an Australian government partnership between the Australian Bureau of Meteorology, CSIRO and the Royal Australian Navy. A major upgrade to this system OceanMAPS version 2 (OceanMAPSv2) was implemented operationally in December 2011 developed through a follow-on BLUElink-2 project. The new system is based on the latest GFDL Modular Ocean Model version 4 and the BLUElink Ocean Data Assimilation System. The area of high horizontal resolution, 0.1°× 0.1°, has remained confined to the Australian region, 90E-180E, 7S-75N however, the vertical resolution in the surface layer was refined to 5 m. OceanMAPSv2 shows approximately a 30% reduction in root mean square error over OceanMAPS for both sea surface temperature and sea surface height anomaly. In particular, the root mean square error for sea surface height anomaly shows that the worst forecasts from OceanMAPSv2 have lower error than the best forecasts from OceanMAPS. A major contributor to the improved performance is the implementation of a new initialisation scheme that more efficiently introduces the BODAS analyses into the ocean model. OceanMAPSv2 has also introduced a daily forecast schedule compared with the twice per week schedule of OceanMAPS. A new four-cycle design was introduced where four independent forecast cycles each time-lagged by one day over four consecutive days are each repeated on a four day period. This system is referred to as a multi-cycle lagged ensemble, as it is demonstrated to have higher cycle-to-cycle independence compared with a traditional time-lagged ensemble. OceanMAPSv2 therefore introduces a range of ensemble diagnostics for each ocean forecast.

2. INTRODUCTION

The Bureau of Meteorology now supports a wide range of environmental information services beyond its traditional atmospheric origins. Coinciding with a global trend toward the development of ocean forecasting the Australian government, through a partnership of the Bureau of Meteorology, CSIRO and the Royal Australian Navy, initiated the BLUElink project in 2004 to develop the first ocean forecasting system for Australia. The Ocean Model, Analysis and Prediction System (OceanMAPS; Brassington et al., 2007) was implemented operationally in August 2007 (Bureau of Meteorology, 2007). A major upgrade to this system OceanMAPS version 2 (OceanMAPSv2) was implemented operationally in December 2011 developed through a follow-on BLUElink-2 project. In this report, we describe the new system and compare the performance to OceanMAPS.

The target for ocean forecasting systems is the mesoscale or "ocean weather", which is the dominant scale of circulation in the mid- and high-latitudes. At this scale the motion is characterised by geostrophic turbulence where eddies and fronts are in quasi-geostrophic balance and undergo multiple interactions converting potential energy and redistributing heat and mass. The ocean weather provides information on the ocean state and circulation that can be skilfully forecast for periods up to 1 month. This information is used by a growing range of applications including: weather forecasting (e.g., sea fog, tropical cyclone intensity), defence, search and rescue, hazardous chemical spill response, shipping (e.g., optimised routing, bilge discharge, towing operations), offshore industrial operations (e.g., drilling operations, offshore oil and gas terminals), fishing and fisheries management (e.g., by-catch), eco-tourism operations, marine park management, coastal hazards (e.g., under keel clearance, inundation/erosion, hypothermia risk) as well as many recreational and research applications (e.g., Brassington et al., 2010; Davidson et al., 2009; Taylor et al., 2010; Sandery et al., 2008). OceanMAPS in particular has had a positive impact on specific events (e.g., the Montara wellhead oil spill, 2009). The Bureau of Meteorology provides ocean forecast information to the Australian public via a graphical service (www.bom.gov.au/oceanography/forecasts/) as well as a data service to registered users and the research community through an OPeNDAP server (godae.bom.gov.au).

An ocean prediction system comprises: ocean observations, an ocean general circulation model, an ocean data assimilation system that merges observations with a model background, an initialisation procedure to reintroduce the information into the model and forcing (e.g., atmospheric fluxes) for deterministic integration. Ocean observations are retrieved in near real-time from the Global Ocean Observing System through a variety of communication networks. The observational requirements for ocean forecasting have been summarised in Brassington et al., (2010), which have spatial resolutions comparable to the model resolution, temporal resolutions hrs-days and low latency. All available ocean profile observations and remote sensing are assimilated. Modelling of ocean geostrophic turbulence requires <1/8° horizontal resolution. Studies have shown that further performance gains can be obtained at 1/32°, Hurlburt and Hogan, (2000). Global ocean prediction is therefore a high performance computing application. The modelling and data assimilation requirements for ocean prediction cannot be met by present super-computers. Contemporary global systems use resolutions of 1/10° (OceanMAPS; Brassington et al., 2007; Oke et al., 2008); 1/12° (HYCOM-NCODA; Cummings, 2005; Chassignet et al., 2009) and 1/4° (FOAM; Martin et al., 2007 and Mercator, Brasseur and Verron, 2006; Medec, 2008) and use three dimensional data assimilation methods. A recent summary of all the international ocean prediction systems at the time of publication is given by Dombrowsky, et al., (2009).

Throughout this report we will refer two versions of OceanMAPS and will adopt the following shorthand labelling convention OMv1 and OMv2 respectively. OMv1 was composed of the

Ocean Forecast Australia Model (OFAM; Schiller et al., 2008) based on the Modular Ocean Model version 4 (Griffies, et al., 2008), the BLUElink Ocean Data Assimilation System (BODAS; Oke et al., 2008), Australian Community Climate and Earth System Simulator -global (ACCESS-G Puri et al., 2010), regridding software, real-time ocean observations and quality control software. OMv1 used a global model with the high resolution, 0.1°× 0.1°, confined to the Australian region, 90E-180E, 7S-75N. OMv1 was run on a regular schedule of twice per week (Monday and Thursday). Each cycle included a 9 (or 8) days behind real-time analysis and a 5 days behind real-time analysis to improve the robustness of the system.

The new system is based on the latest GFDL Modular Ocean Model version 4 and the BLUElink Ocean Data Assimilation System. The area of high horizontal resolution has remained confined to the Australian region however, the vertical resolution in the surface layer was refined to 5 m. OMv2 retains the 9days and 5 days behind real-time analysis cycle however, a forecast cycle is performed daily. A novel four-cycle design is introduced to avoid over-fitting of altimetry. Four independent forecast cycles each time-lagged by one day over four consecutive days are each repeated on a four day period. The four-cycles are demonstrated to have higher cycle-to-cycle independence compared with a traditional time-lagged ensemble. OceanMAPSv2 therefore introduces a range of ensemble diagnostics for each ocean forecast including forecast range, mean, and variance.

Coinciding with the development of a new system for operations a demonstration of its function and performance improvements over an existing operational system is undertaken. In the case of OceanMAPS, there are three stages of testing: (a) prototype demonstration of ocean general circulation model and data assimilation system upgrades, (b) research trial of the forecast system and (c) operational trial of the system. This report is based on an operational trial period, Dec 2010-Mar 2011, which corresponds to the Austral summer. This report reviews the changes between the two systems, OMv1 and OMv2 in section 3, documents and compares the performance during the operational trial period in section 4 and provides a conclusion in section 5.

3. SYSTEM DESCRIPTION

The OMv2 system is composed of a real-time ocean observing system, a quality control system, the Ocean Forecast Australia Model (OFAM), the BLUElink Ocean Data Assimilation System (BODAS), an adaptive initialisation scheme and air-sea fluxes from the Australian Community Climate and Earth System Simulator (ACCESS). We summarise each component of the system and highlight new features relative to OMv1, which provide a basis for interpreting the differences in performance presented in section 4.

3.1 REAL-TIME OCEAN OBSERVING SYSTEM

The quality, volume and latency of ocean observations have been on a steady positive trend over the past few decades thanks to significant efforts in the international community summarised in Koblinsky and Smith, (2001) and Hall et al., (2011). The coverage remains temporally and spatially sparse (particularly below the surface) for ocean forecasting applications and there is a motivation to make use of a maximum of observations. However, the use of any observation in data assimilation requires an estimate of its error and this error relative to all other errors determines the impact on the analysis. Typically the error models adopted are simplistic and frequently optimistic assuming they are normal, stationary and uncorrelated all of which apply only to a subset of the observations. Adoption of such error models introduces the notion of "good" / "bad" observations where "good" can be defined as those that have errors within the population of the specified error model. Experience shows that the majority of real-time ocean observations are "good" and once identified the lower error introduces a greater weighting in the data assimilation. However, the price paid in this paradigm is the need for a quality control procedure to pre-filter the "bad" observations. Oceanography has typically established highly sophisticated methodologies, some that are very labour intensive to extract the maximum number of "good" observations, so-called delayed quality control (QC). This quality control paradigm was developed when data volumes were low and the objectives were climatological in nature. Maintaining this paradigm is a significant challenge with the increased data volumes and an emphasis has been on developing real-time quality control procedures, so-called automatic QC, to reduce the volume of profiles requiring human attention. Automation of QC decisions is a challenging task, which is discussed in Cummings et al., 2011 and Cummings, 2011. The simplest decisions are those that are obviously bad, e.g., a reported location that is over land or values that exceed physical bounds. Other tests search for properties that occur infrequently such as large gradients and spikes and are identified as potentially bad. For operational oceanography, there are resources or time to go beyond the automatic QC step so a more conservative approach is required for those identified as potentially "bad". The risk in this strategy is that extreme conditions might be missed and would rely more on the model forecast. However, the inclusion of "bad" observations in ocean prediction systems can have significant consequences. At the extreme end they can induce numerical instabilities and a model crash but in less extreme case (possibly more dangerous) they can provide seemingly valid anomalous values and false warnings. The strategies used in OceanMAPS are described below against each major data type. In general the choices are conservative to maximise system robustness. We acknowledge that there is significant room for improvement in all aspects, the selection of data, the specification of error models and automatic QC procedures.

3.1.1 Satellite altimetry

Altimetry measures to high precision the distance from a satellite in orbit to the earth surface. The shape of the ocean surface is determined by a full spectrum of time and space scales including the geoid, the mean dynamic topography, ocean tides, tide loading and a range of phy2sical ocean dynamic processes. The component of this signal that is of interest to the OceanMAPS is the so-called sea surface height anomaly (SSHA), or sea level anomaly (SLA), which are used interchangeably. As denoted by Desai et al., (2003) (pp3) the SSHA is determined from the removal of 10 correction terms and a bias as,

$$\begin{aligned} \mathrm{ssha} = (\mathrm{orbit} - (\mathrm{range}_{\mathrm{ku}} + \mathrm{iono} + \mathrm{dry} + \mathrm{wet} + \mathrm{ssb}) \\ -(\mathrm{mss} + \mathrm{setide} + \mathrm{otide} + \mathrm{pole} + \mathrm{invbar}) + \mathrm{bias}) \end{aligned}$$

where $\mathrm{range}_{\mathrm{ku}}$ is Ku band range, iono is an ionospheric correction, dry/wet is a dry/wet atmosphere correction, ssb is sea state bias, mss is mean sea surface with respect to ellipsoid, setide/otide/pole is solid earth/ocean/pole tide, invbar is inverse barometer correction.

At the time of operational trial, there were three altimeters in orbit as summarised in **Error! Reference source not found.** Each of these satellites are a narrow swath altimeters providing measurements along track. These orbits are specifically selected to have repeating orbits to permit several corrections to be computed to high precision and reduce the observation error. The Jason series have an inclination of 66.05°, which has the positive impact of reducing the cycle period to ~9.9 days but no coverage for high latitudes and a track separation of 360°/127 orbits = ~2.8°, which is ~315 km at the equator crossing. Envisat has an inclination of 98.5°, which has the positive impact of providing coverage for high latitudes and a reduced track separation of 360°/501 orbits = 0.72° which is ~80 km at the equator crossing but has a longer cycle period of ~35 days.

Table 2 Satellite orbit properties as defined by space-track (https://www.**space-track**.org/)

Common Name (NORAD)	**Country**	**Launch Date**	**Period**	**Incl.**	**Apogee**	**Perigee**
JASON1 (26997U)	US	2001-12-07	112.42	66.05	1344	1332
ENVISAT (27386U)	ESA	2002-03-01	100.54	98.55	768	766
JASON2 (33105U)	NASA/NOAA	2008	112.42	66.05	1344	1332

There are several techniques that can be used to determine the position of the satellite which vary in accuracy and latency. Each estimate forms the basis of a different Geophysical Data Record (GDR) product. The Interim GDR (IGDR) targets a fast orbit determination that is less accurate than GDR but can be delivered with a latency of a few days.

Data from the Jason1 satellite is processed in near real-time at the Jet Propulsion Laboratory and distributed through the Physical Oceanography Distributed Active Archive Center (PO.DAAC) via the OCEANIDS service. Jason2 delayed-mode processing occurs at Centre National d'Etudes Spatiales (CNES). The IGDR product is accessed from NOAA's Comprehensive Large Array-data Stewardship System (CLASS). Both Jason1 and Jason2 IGDR products are available with a latency of 2-3 days.

The Envisat IGDR product is processed and distributed by ESA's French Processing and Archiving Centre (F-PAC) with a latency of 3-5 days. F-PAC also distributes corrections for Envisat's Ultra Stable Oscillator (USO) that has had degraded performance since 2006.

In summary, the complete orbit of the Jason1 and Jason2 IGDR product is available between 3-13 days behind real-time, the complete orbit of Envisat IGDR product is available between 5-40 days behind real-time.

The performance of OMv1 and v2 is sensitive to the coverage of satellite altimetry with a measurable deterioration in performance when satellite tracks are absent. This relationship is discussed further in section4.5. The sensitivity is related to the observed spatial sampling relative to the spatial and temporal decorrelation scales of the mesoscale variability. Figure 1a shows the spatial coverage obtained from the three contemporary satellites Jason1, ENVISAT and Jason2 on the 15th March 2011 in the Tasman Sea. The tracks are overlayed on the sea surface height anomaly (relative to the modelled mean dynamic topography) from OFAM2 as part of the behind real-time analysis of OMv2. The model field shows a spectrum of large (~200 km) through to small scale (~50 km, resolved by the model) eddies and fronts that are typically present during March. The increase in the associated geostrophic turbulent energy during this season follows from the increased volume and heat transport of the East Australian Current during the Austral summer (figure 7 in Schiller et al., 2008), which is a source of potential, kinetic and rotational energy. A single day coverage from the three altimeters is insufficient to observe all of the larger eddies.

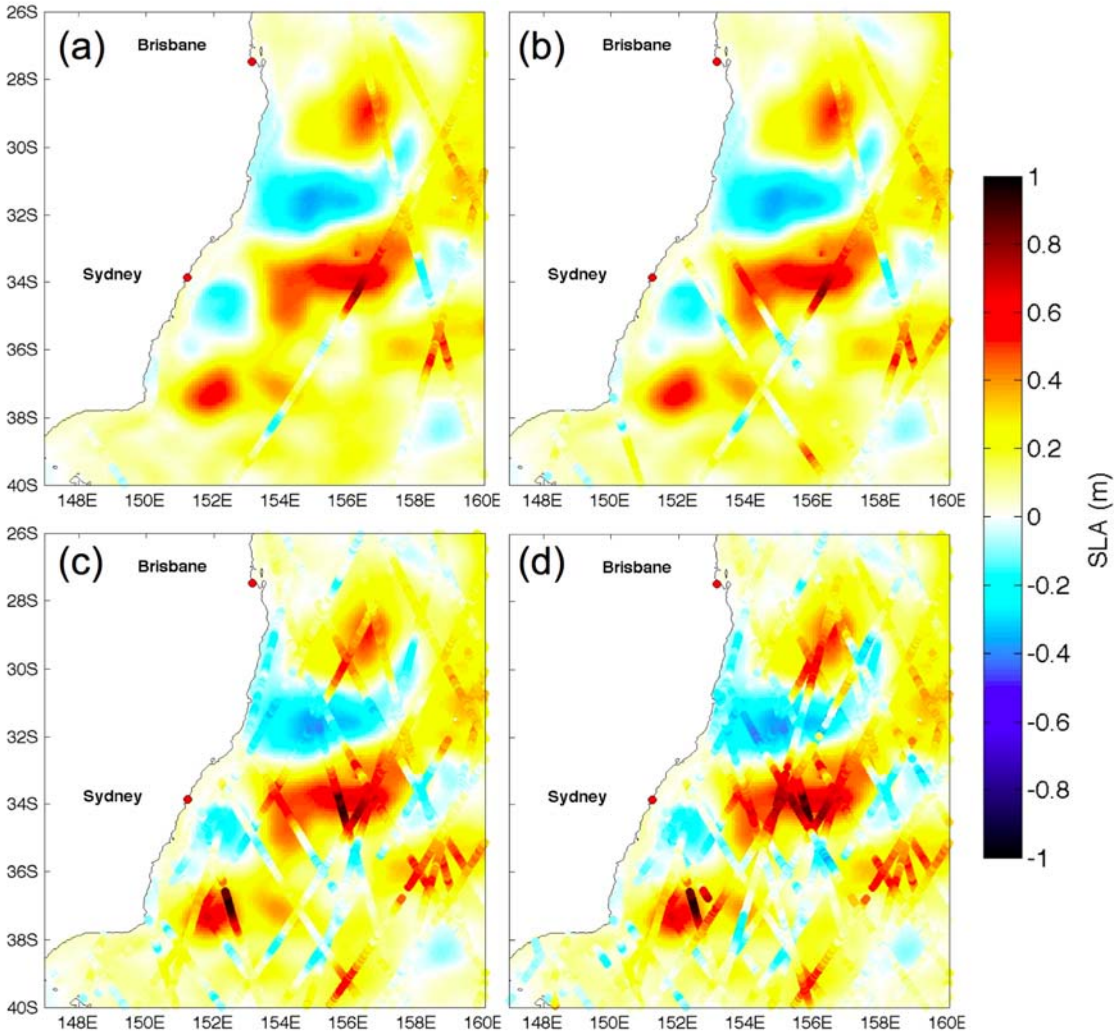

Fig. 1. The spatial coverage of three narrow-swath altimeters (Jason1, ENVISAT and Jason2) over the Tasman Sea for the 15th March 2011. The tracks are plotted using a colour for the observed SSHA and overlayed on a background field of the 24hr average SSHA from the behind real-time analysis cycle relative to the modelled mean dynamic topography. The four plots represent the coverage for different symmetric time windows from the target date, (a) +/- 0 days, (b) +/- 1 days, (c) +/- 3 days and (d) +/- 5 days.

It is evident from observations and modelling that ocean eddies contain a core of water mass that evolves relatively slowly and frontal boundaries that can change rapidly. In addition, the eddy cores can occupy a large proportion of the domain (i.e., space filling), therefore there is a large proportion of time-lagged observations that are correlated with the analysis target date. Based on these properties we claim that a larger time-window of SSHA observations can be adopted for the analysis step. Figure 1 b-d show the tracks that are included by successively increasing the window by +/- 1 day, +/- 3 days and +/- 5 days respectively. Figure 1b shows that with three altimeters +/- 1 day remains insufficient to sample all of the large eddies. At +/- 3 days the coverage for this specific date is sufficient to sample each of the large eddies. However, the most reliable coverage is obtained for the +/- 5 days, which ensures a complete cycle of tracks for both Jason 1 and Jason 2. It is this latter time window, which is adopted for the behind real-time cycle for OMv1 and v2. Complementary to this strategy however is the assignment of an error penalty for the age of the observations relative to the target analysis date, which is discussed in Oke et al., 2008 and section 3.4.4.

It is worth pointing out that during the lifetime of OMv2 both the Jason1 and Envisat satellites will cease operations. There is a medium level risk that for a period of time operational ocean prediction systems will be reliant on Jason-2 only. The coverage obtained from Jason-2 based on a +/- 5 day window for the same region of the Tasman Sea is shown in Fig. 2. In this example the coverage is sufficient to observe all of the peak features, however, it is clear that the scale of the diamonds are of the order of the eddies so that features will have a high likelihood of either not being observed or being aliased. It has been shown that for delayed mode a minimum of two satellites is required, whilst for real-time systems a minimum of three altimeters are required with four altimeters showing a positively statistical impact, (Pascual et al., 2009). The sensitivity of the performance to altimetry coverage discussed in section 4.5 is consistent with these conclusions. The performance of OMv2 will therefore substantially decrease should this scenario eventuate.

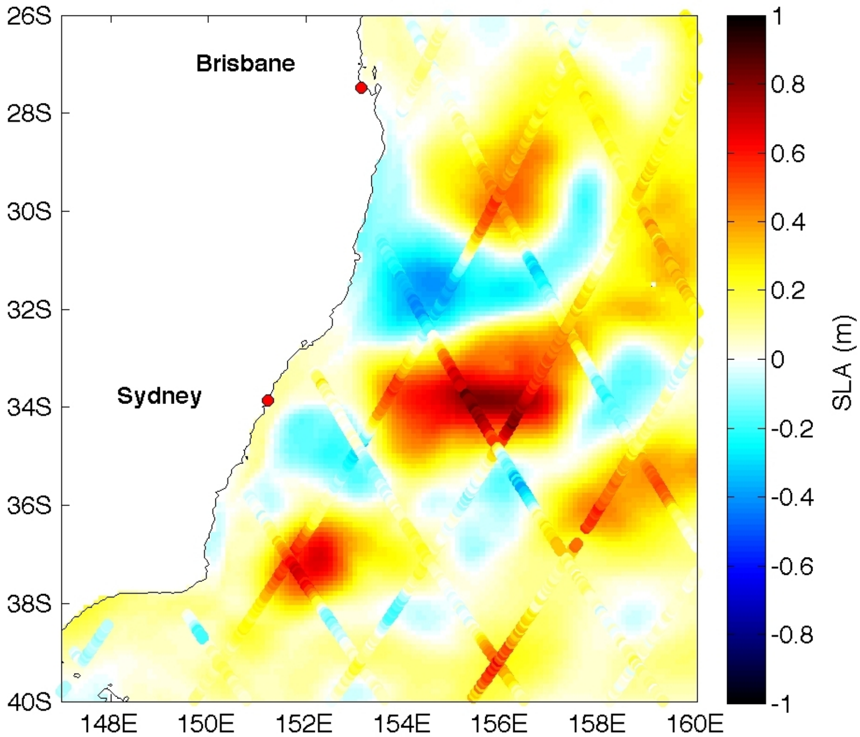

Fig. 2. The spatial coverage for Jason 2 using a window of +/- 5 days over the Tasman Sea for the 15th March 2011. The tracks are plotted using a colour for the observed SSHA and overlayed on a background field of the 24hr average SSHA from the behind real-time analysis cycle relative to the modelled mean dynamic topography.

3.1.2 Satellite Sea Surface Temperature

Sea surface temperature (SST) is observed from multiple satellites, with varying orbits, sensors, accuracy and swath coverage. SST therefore provides the largest coverage, lowest error and lowest latency dataset of any ocean variable. At the same time, SST is a complex interfacial variable that requires substantial pre-processing to correctly select representative data for use in a particular ocean data assimilation application. There are also a number of specific properties of the ocean prediction system that define what SST product will best match that represented by the modelled variable. The first is the resolution of the top cell of the model which in this instance is $0.1°\times0.1°\times5$ m in the Australian region. The second is the temporal averaging used to estimate model error (innovations), which is 24hrs. Lastly, is the choice of background error covariance discussed in section 3.4.3.

Much of the important work has been undertaken by the Global High Resolution Sea Surface Temperature (GHRSST) science team (Donlon et al., 2009) including: definitions for SST, calibration/validation, bias estimation, quality control procedures, metadata standards and data product types. GHRSST have introduced definitions to the concepts of skin (microns), sub-skin (mm) and foundation (1 m) temperatures, (http://www.ghrsst.org/SST Definitions.html). Foundation SST is defined as the ocean surface temperature in the absence of diurnal warming/cooling and is the most representative of a 24hr mean ocean model SST. The skin temperature, which is observed by satellite infrared sensors, can acquire values in excess of 1°C greater than foundation SST through diurnal warming. That is the temperature at a few micrometers depth within the ocean surface. The ocean model for OMv1 and v2 has surface cells of 10 m and 5 m respectively and cannot represent the skin temperature, without the inclusion of a specific diurnal/skin model. However, when the upper layer of the ocean is well mixed through momentum or buoyancy fluxes the skin temperature is more directly related to the foundation temperature. In particular, GHRSST have established algorithms for accounting for warm and cool skin biases, (Donlon et al., 2002) and to identify observations of foundation SST through wind-stress. It is noted (and subsequently exploited here) that the maximum cool skin bias is observed to be much less than the warm skin bias. The algorithm for foundation SST presented by Donlon et al., (2002) accounts for this by imposing a higher threshold for 10 m wind (>6ms^{-1}) for the warm-bias.

AMSR-E is a wide-swath microwave SST sensor on board the TERRA satellite with a sun synchronous orbit. As a microwave sensor, it measures temperatures close to the subskin temperature, obtained within a few millimeters from the air-sea interface. The ascending swath crosses the equator at the local time of 1.30pm, which is therefore biased warm in weak wind conditions. Similarly the descending swath crosses ~12hrs later, at approximately 1.30am local time at the equator. A microwave sensor has the advantage over infrared that it can observe SST under cloudy conditions (except when there is also precipitation) providing greater coverage. The microwave band however provides a reduced spatial resolution of ~10 km. The coverage around land boundaries is further reduced to ~50 km through interference of the sensors by the land. An estimate of magnitude and distribution of the diurnal variation in SST can be obtained by comparing the ascending and descending observations. Figure 3 shows the diurnal range for the Austral summer and Austral winter seasons. Each pixel represents a binned average of the differences from collocated pairs from each orbit cycle in 24 hrs. As expected there is a clear hemispheric bias to the distribution of the diurnal range. There is some evidence that the swatch pattern is effecting the statistics but there is generally good agreement with known locations of high evaporation, the warm pools in the tropics. There are large regions where the warm bias can exceed 0.5 °C and many regions in the tropics where this can exceed 1 °C. We note that an interesting cool bias appears in Austral winter in the western Bay of Bengal, the sub-tropical gyre in the Pacific and the western boundary of the South Atlantic. In the mid-latitudes the prevalence of storms reduces the percentage of matchup to 10% of the possible number which brings the number of samples to ~10. Therefore in these regions the undersampling could be responsible for the misfits shown where through random chance the daytime SST was effected by surface mixing and cooled the surface. However, the large spatial scale of the cool bias in the South Pacific is suggestive that perhaps this is a real effect. During the Austral winter the western part of the Bay of Bengal is well sampled which suggests that the bias found there must be related to a real physical effect. One hypothesis is that in these regions the daytime pixels may be effected by small fractions of precipitation that are close to the threshold used to flag observation quality. Another hypothesis is that the day time winds are stronger leading to a systematically larger overturning. Repeating the calculation over more years would help to remove the sampling error and determine if this was indeed systematic in these regions.

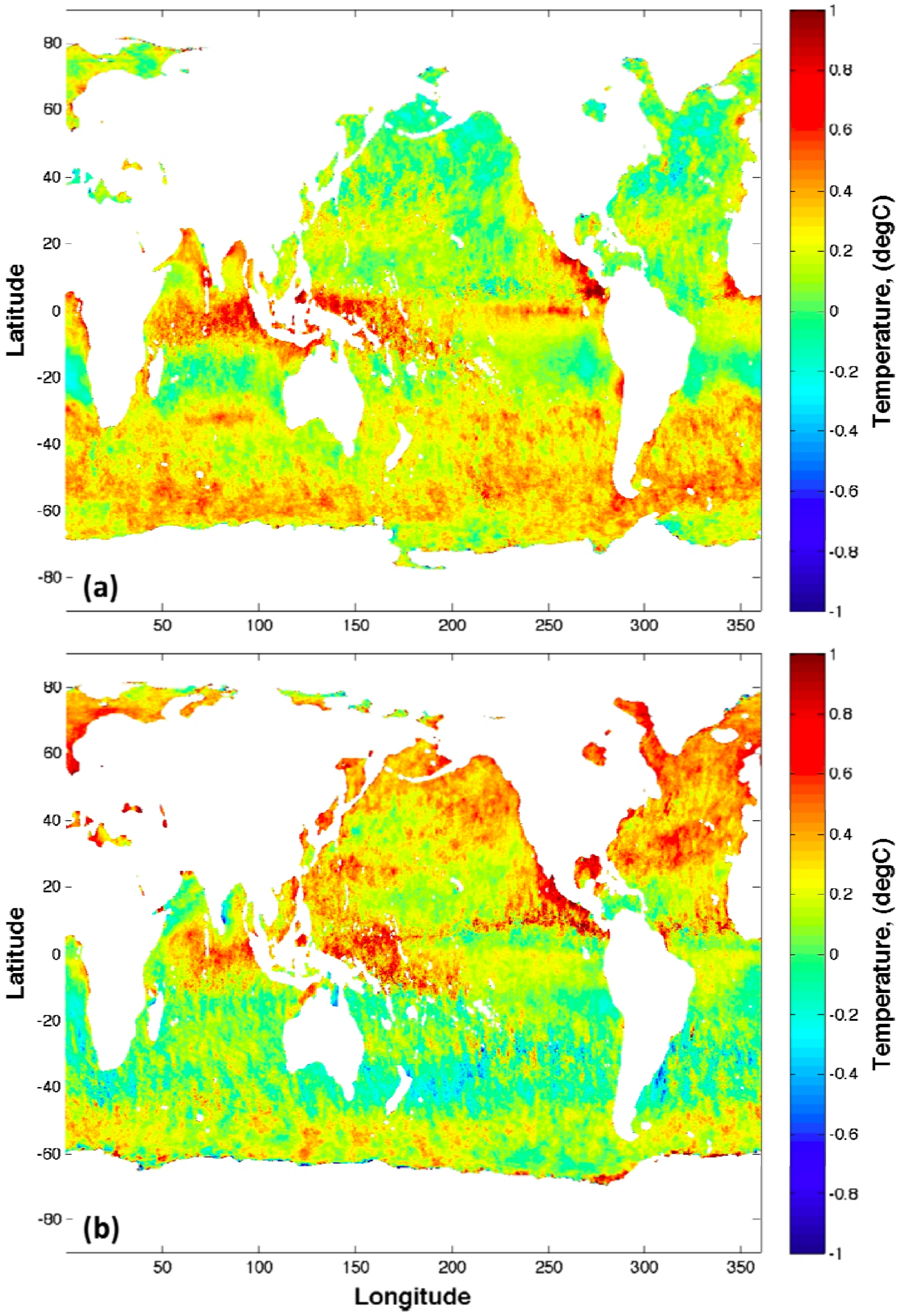

Fig. 3. Estimation of the mean diurnal bias (ascending minus descending) between collocated pairs of AMSR-E observations from the ascending and descending passes, (a) Austral summer (1 Nov 2006 - 28 Feb 2007) and (b) Austral winter (1st June 2006 - 31st August 2006).

The added value of including the ascending swath observations from AMSR-E has been assessed using two criteria. The first criterion is the number of times that an ascending observation is available when a descending observation is absent. The second criterion is to retain only observations for which the absolute bias is less than 0.2 °C. Figure 4 shows the pixels where criterion 1 exceeds 30% and criterion 2 is satisfied for both Austral summer and Austral winter. During Austral winter the added value from the ascending tracks using this criterion is limited to a narrow band approximately following the South Equatorial Current in the Indian Ocean and South Pacific. During Austral summer a similar pattern occurs in the Australian region but the zonal band is wider and shifted to the south. There are two features along the dateline and along the Greenwich meridian that are artifacts of the difference in orbit period and the 24 hrs used for matchups. In OceanMAPS we exclude the ascending swath observations in order to remove the diurnal warm bias. However, there are regions and periods throughout the year where their use could be optimized.

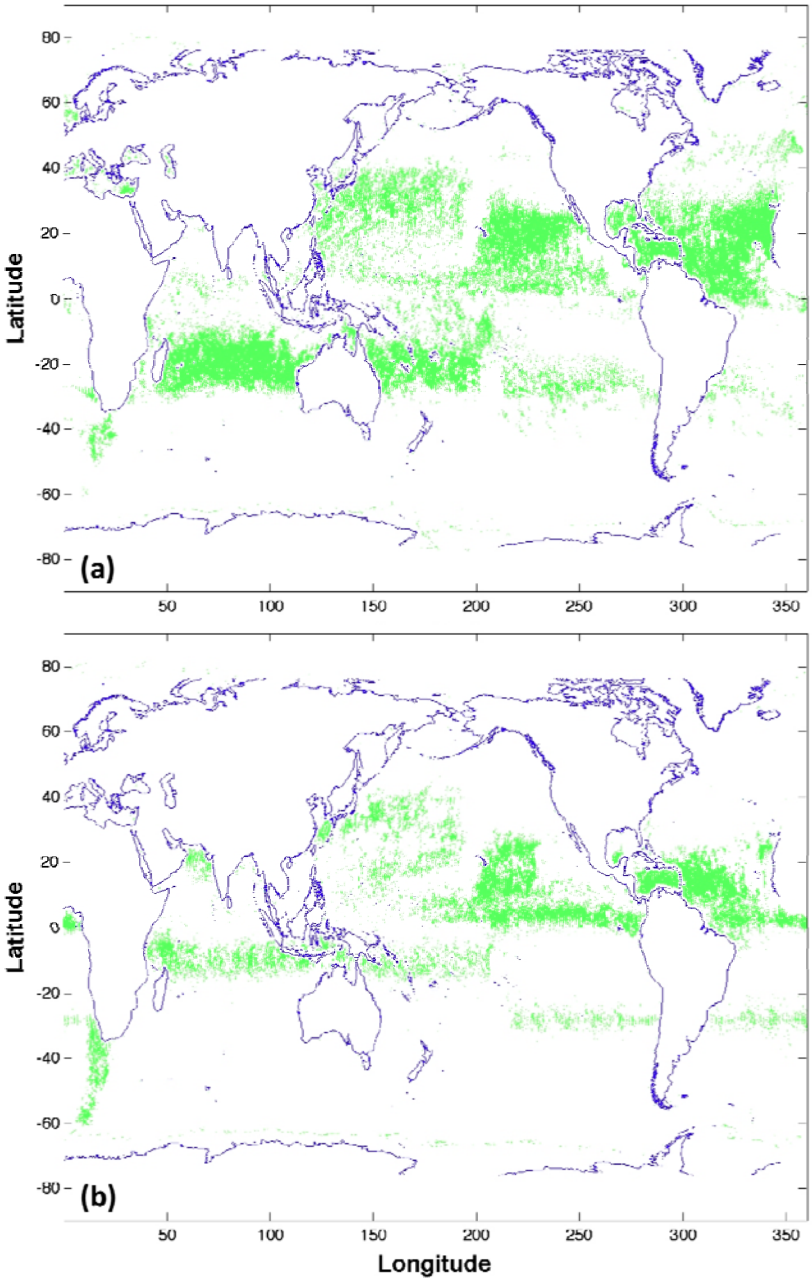

Fig. 4. Bins that satisfy the ascending swath contribution criterion, >30% of the time the ascending is the only observation and the mean absolute bias of ascending minus descending is <0.2 °C. (a) Austral summer (1 Nov 2006 - 28 Feb 2007) and (b) Austral winter (1st June 2006 - 31st August 2006)

The NOAA AVHRR series has been sustained as an operational platform with wide−swath infrared sensors and multiple satellites in sun−synchronous orbits. The resolution ~1 km is greater than that of current and near future ocean forecast systems (Dombrowsky et al., 2009; Hurlburt et al., 2009). This permits the construction of super−observations (Purser et al., 2000) that have reduced representation error increasing the weighting in the analysis. The higher resolution also provides observations over the continental shelf and Gulf regions compared with microwave sensors. NAVOCEANO provides a 1 m-foundation temperature, swath L2P product available in near real-time at a resolution of ~9 km (NAVOCEANO's GAC AVHRR L2P SST). An observation error for the foundation temperature can be constructed to account for residual diurnal signals based on the time from nearest local dawn−time as well as an age penalty for time from the analysis time (Andreu−Burillo et al., 2009).

The strategy adopted for OceanMAPS can be summarized as follows:

- *Only choose platforms that offer 24hr global coverage* - the rationale being to have homogenous treatment of bias (less small scale gradients/noise and simpler to post-process) as well as a reduction in computational cost. Two candidates that have not yet been implemented are MODIS and MT-SAT. The AATSR data is indirectly used through the cross-platform calibration of AMSR-E and AVHRR.
- *Include microwave and IR* - the resolution and accuracy of microwave is compatible with ocean models and is not seen as a limitation. Microwave provides greater coverage globally, although a conservative choice is required to use a smaller fraction of precipitation threshold. IR instruments when available provide observations closer to coastlines.
- *Adopt L2P products* - L2P products provide a standard format of swath observations with the additional metadata required to pre-process the observations for specific applications. This level of product provides the observations at their primitive/original horizontal resolution, allowing for case-specific processing in accordance to the scales of interest.
- *Minimise diurnal bias* - noting that the maximum nighttime diurnal bias is much smaller than daytime. Observations are preferentially sorted for nighttime temperatures. Only descending tracks are used for AMSR-E and AVHRR is sorted for observations closest to local time of dawn.

There is a significant volume of SST observations that are excluded by this strategy, either from the platforms included or from the platforms as yet not implemented. It is acknowledged that there is a high probability that many of these are "good" observations. Therefore there is considerable scope to revisit and improve this strategy. However, this requires a rigorous evaluation of new robust strategies or new platforms and will be left for future work. We note that during the time of writing this report AMSR-E ceased operations and OMv2 is currently using only AVHRR observations but with a larger observation window to improve coverage. A follow-on instrument AMSR-2 is scheduled for launch on GCOM-W1 in Feb 2012 with two repeat missions out to 2025.

3.1.3 In situ profiles and duplicate checker

The ocean state is routinely profiled in real-time by Conductivity-Temperature-Depth (CTD) and eXpendable Bathy-Thermograph (XBT) instruments. These are collected from a variety of platforms with the leading ones being the moored arrays in the tropical oceans (e.g., TAO/TRITON), autonomous Argo floats and volunteer ship XBT lines. The Argo network is the primary observing platform in the mid- to high-latitudes with a target coverage of 1 float per 3°×3° region in the open ocean (Roemmich, et al., 2001). All of the real-time observing systems are reported on the WMO Global Telecommunication System (GTS) using either TESAC (Temperature, Salinity, Current report) or BATHY (Bathythermal observation report) formatted messages. Only the Argo profiles undergo a quality control procedure prior to upload to the GTS however these do not include quality control flag meta-data.

The Argo observations are retrieved by a network of Data Assembly Centres (DAC's), which are responsible for performing an automatic quality control before uploading the processed observations to both the GTS with a low latency and the two Global DAC's (GDAC's, USGODAE and Coriolis) with a latency of approximately 3 days. The DAC's also perform an objective quality control in delayed mode.

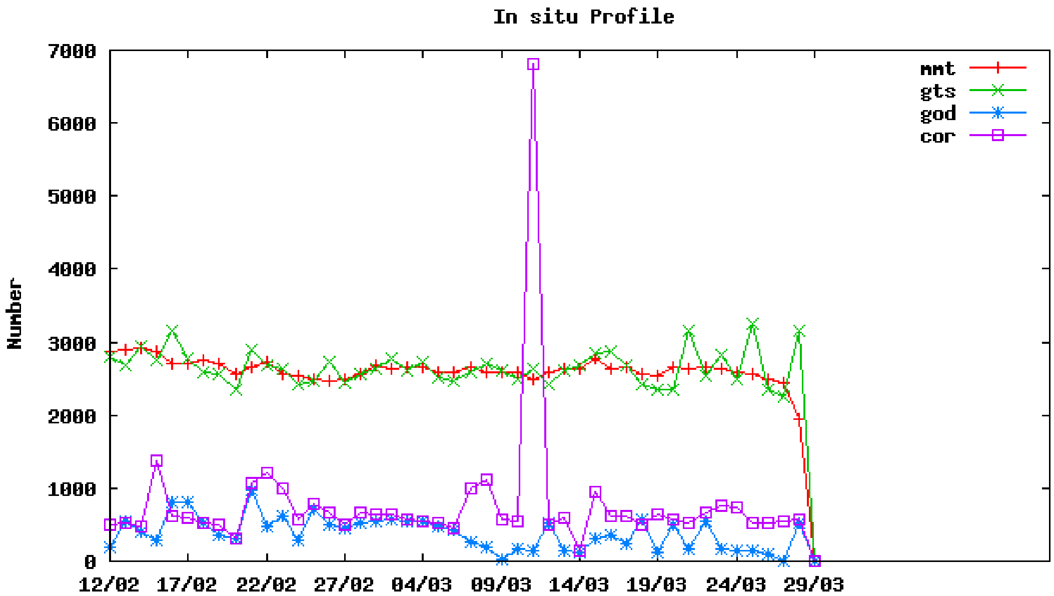

Fig. 5. A time series of the number of profiles retrieved from the three sources, GTS (green line), USGODAE (blue line) and Coriolis (pink line) for example period 12 February to 29 March 2011. The number of profiles in the corresponding merged and duplicate checked data files is represented by mmt (red line).

In practice, neither of the two GDACs or the GTS hold a super-set of the best quality Argo profiles. Figure 5 shows a time series of the number of profiles from each source and the resultant merged (mmt) file. The upload of delayed QC profiles to the GDACs appear as spikes in numbers of available profiles. More recently the GDACs have separated the real-time and delayed QC profiles into two data streams although this has not eliminated all spikes. Coriolis typically contains more profiles than USGODAE as it also includes Argo floats that have non-standard profiling missions.

The Bureau of Meteorology has adopted the strategy of downloading all three data streams and performing a duplicate checking strategy to create a super-set of the best quality profiles available. A duplicate checker was developed to firstly locate all duplicates profiles and secondly, create a single daily NetCDF file containing the best copy (the highest level of quality control) of each observation for each day. Profiles are processed in the source order of USGODAE, Coriolis then GTS, with best copy selection beginning with the USGODAE. This biases the profile count towards USGODAE over Coriolis as shown in Fig. 6. Argo profiles on the GTS are selected only when copies are not available on either GDAC, as these are in TESAC format and lack both metadata and quality control flags.

Initial processing of Argo profiles highlighted the differences in the file update cycles of each GDAC, in addition to the high number of duplicates occurring on each server. Figure 6 indicates the number of observations from each source the total number of duplicates and the timeliness of profile data for example period (31 January to 2 March 2011). Timeliness indicates the delay between when the profile is actually recorded in situ and when it is available from either the GTS or GDAC. The majority of profiles are generally available at the GDACs approximately 1-2 days behind real-time, with Coriolis generally more timely in uploading profiles than USGODAE. Profiles that are a more than one month old are generally scientifically quality controlled delayed mode profiles that have been resubmitted by the DACs.

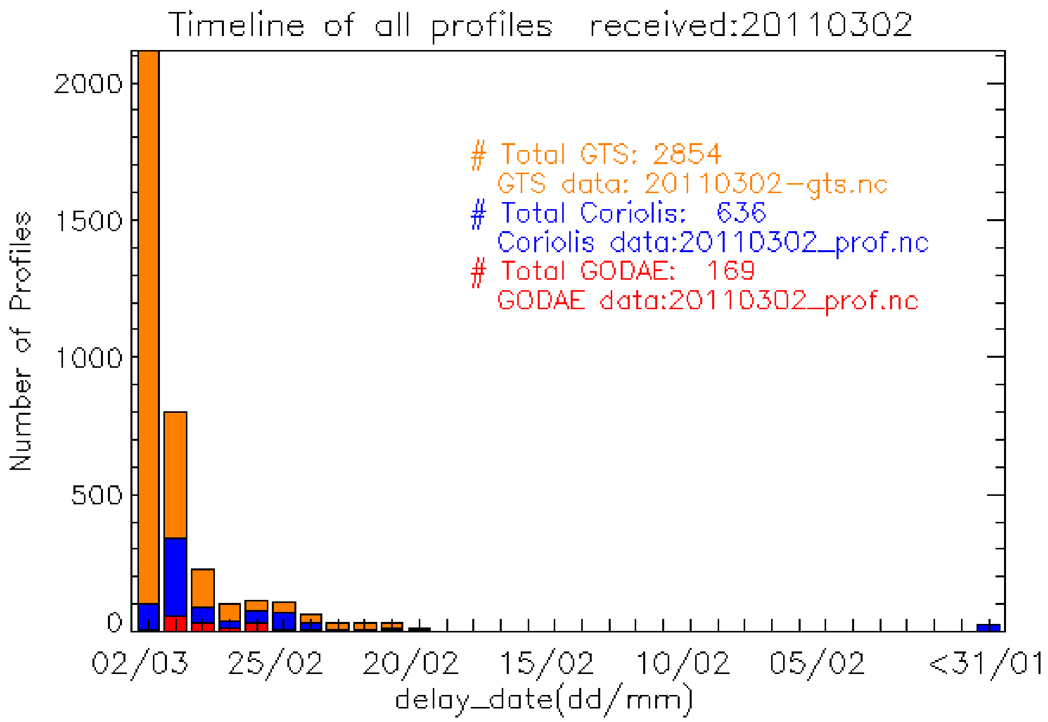

Fig. 6. The distribution of the number of profiles retrieved relative to the latency from the GTS and GDAC's (Coriolis and USGODAE) for example date 2 March 2011. Profiles received for 31 January from Coriolis are most likely delayed mode scientifically quality controlled profiles.

The duplicate checker is a suite of IDL scripts that sorts all available profiles within a time window (e.g. 7 days), selects the best copy of each profile according to a ranking system and writes it to the appropriate daily best observations NETCDF file. Firstly an identification tag is assigned to each profile to be processed, containing the profile platform number, location and measurement date. Each profile is also ranked at the same time and assigned a label composed of flags indicating the presence of adjusted/corrected data for each parameter, plus the data state or level of processing. Any profiles that do not have platform numbers or measurement dates, are outside the processing time window (e.g. 7 days) or have come from grey-listed (faulty or suspect) floats are immediately rejected.

Secondly, duplicate profiles are then identified by matching profile id tags. The best copy of each profile with multiple copies is then selected, based on their rank and date of arrival at the GDACs or GTS. If a profile has corrected data or has been subject to more processing than other copies, i.e. has a higher rank, it will be selected and duplicates rejected. If the ranks of the observation and duplicates are the same, the profile which was last received by the source (i.e. USGODAE, Coriolis or GTS) is selected. If two profiles are both received on the latest date, the first profile is arbitrarily selected. The location and source of the best observations selected from those available at all three sources for example date 2 March 2011 are shown in Fig. 7.

A secondary duplicate check is also employed to catch multiple copies of Argo profiles that have slightly different measurement times. Discrepancies between measurement dates of duplicate profiles usually occur between profiles on the GTS and copies at a GDAC and are generally of the order of minutes to a few hours. This check is performed by searching for Argo profiles with the same platform name with measurement times within 12 hours of one another. If any profiles are located, the best observation is selected based on rank and arrival date as detailed above.

Selected profiles for each measurement date are then written to new daily NetCDF observation files which follow the same format as Argo GDAC daily files. If no data is available for a particular field in the new files, it is filled with the appropriate fill value. The history fields are updated for each profile to indicate it has passed through the duplicate checker, the date of processing and the original data source i.e. USGODAE, Coriolis or the GTS.

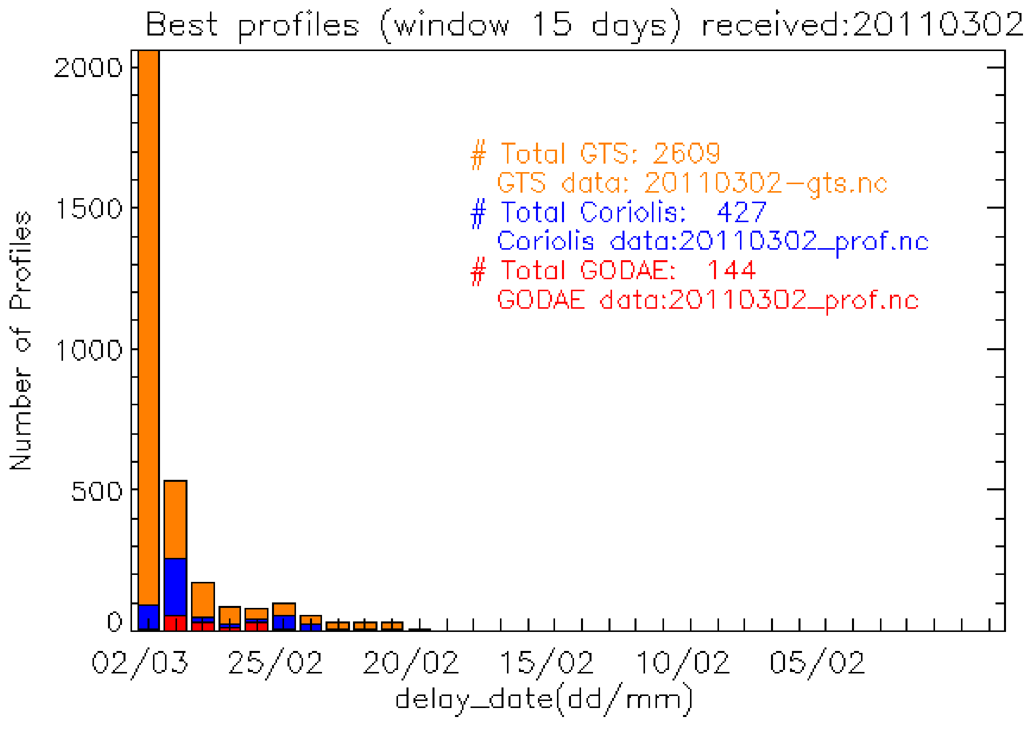

Fig. 7. The distribution of the number of profiles relative to latency from the duplicate checker processing for the best profile for example date 2 March 2011.

3.2 IN-SITU QUALITY CONTROL SYSTEM

The quality control procedure applied to the duplicate checked profiles described in section 3.1.3 is based on several tests that are grouped into two stages: 1. Internal stage – tests based upon the values and attributes self-contained within the duplicate checked file and 2.

External stage – quality control tests that require additional information external to the file. The quality control procedure assigns a status based on three states described in Table 3. The full algorithm and variables used in the quality control of profile data is summarised in Appendix D .

Table 3 Real-time quality control flags and definitions used to assign values

Flag value	Quality status - False/True/Undefined
0	True(Pass) (a) Argo QC flag <=2 or (A or B) (b) Passes internal or external tests
1	False(Fail) (a) Argo QC flag >=3 or (C,D or E) (b) Fails internal or external tests
-999	Undefined – 1. if the value is undefined in the profile due to padding 2. the external parameter used in the test is undefined (e.g., climatology)

3.2.1 Internal stage: Analysis of current in situ profile.

Test 1a: Pre-processed quality control attributes assigned with the data

Each duplicate checked mmt-profile is provided in Argo format [Carvel et al., 2003] which contains attributes for pre-processed quality control. Argo quality control flags are assigned by digits, ranged from 0 (no quality estimation) to 9 (very bad quality) or letters, ranged from A to G (Argo flag scale [described in reference table 2, Carvel et al., 2003]. Increasing parameter values or letters correspond to deterioration of its quality. If QC parameters greater than or equal 3 (or equivalently C) the corresponding profile or value is assigned a flag of fail.

The quality control attributes examined include: (a) flag for the entire profile and (b) flag attributed to individual values. The specific profile flags examined are shown in Table 4 in the sequential order and the entire profile is assigned a flag of fail if Argo flag is assigned fail (refer Table 3).

The native values (PRES, TEMP and PSAL) are merged with replacement by any adjusted profiles if they exist (PRES_ADJUSTED, TEMP_ADJUSTED and PSAL_ADJUSTED). Adjusted variables are used during the manual quality control e.g., corrections for salinity drift. In real-time it is expected that there will be no value assigned to these variables. Each adjusted profile is associated with an adjusted QC variable. The adjusted QC also replaces the corresponding flag in the merge. Only the merged QC flags are used.

Table 4 Argo profile quality control variables

Argo QC attribute name	Description	RTQC
POSITION_QC	Quality flag on the horizontal position	1 (assigned if bad_profile =.true.)
JULD_QC	Quality flag for the date and time	2
PROFILE_PRES_QC	Global quality control flag for PRES profile	3
PROFILE_TEMP_QC	Global quality control flag for TEMP profile	4
PROFILE_PSAL_QC	Global quality control flag for SALT profile	5

Test 1b: *Monotonicity test*

Strict monotonicity of pressure is applied to each profile. If this condition is violated all values of QC_pressure at the depth of the violation and below are assigned a fail.

Test 1c: *Quality control data by verifying their possible range and missing values*

Each temperature, salinity and pressure profile is checked against physical limits defined in Table 5. All failures are assigned against the individual values for the variables QC_pressure, QC_TEMP_missval. QC_PSAL_missval. If TEMP, PSAL are equal to the FillValue they are assigned as undefined. If there are values that correspond to missing_value the above flags are assigned fail.

Table 5 Physical limits applied to observations

Variable	**Physical limits**
Pressure	0 < PRES < 6500 (decibars, ~m)
Temperature	-2 < TEMP < 39 (degC)
Salinity	0 < PSAL < 40 (%o, PSU)

3.2.2 External stage: Analysis of current in situ profile

Test 2a: *Bathymetry test*

Each profile depths (PRES) are compared against the depths of bathymetry defined by an external source. All profile values that lie below the bathymetry are assigned a fail. The topographic height is defined by bath_mom_5.nc, which is based on US Navy ETOPO2 and Geoscience Australia data sets (prepared by CAWCR). This global bathymetry is defined for a resolution of 1/30°x1/30°. The current position of profile is compared with average over 4 adjacent bathymetry points. If the depth of profile is greater than the average depth, all points at this depth and below are assigned a fail in QC_bathymetry.

Test 2b: *Gradient test*

Profile values (temperature and/or salinity) are rejected if the vertical gradient of value exceeds a priori threshold value. The gradient is defined as

$$f(i) - (\alpha_1 f(i+1) + \alpha_2 f(i-1)) < \text{tol}$$

where

$f(i),\ f(i-1),\ f(i+1)$ are values of temperature and/or salinity on ***i***-level, respectively and the nondimensional weights are given by,

$$\alpha_1 = \frac{z_{i+1} - z_i}{z_{i+1} - z_{i-1}}, \alpha_2 = \frac{z_i - z_{i-1}}{z_{i+1} - z_{i-1}}$$

If the gradient test is not satisfied then all three valid values are assigned a fail. In the case of boundary points or points adjacent to undefined values then the gradient is computed linearly and tested against the same tolerances. The tolerances have been taken from earlier documentation for QC.

Table 6 Tolerances used in the gradient test

Variable and depth range	**Tolerance (tol)**
Temperature (PRES<=500)	10 degC
Temperature (PRES>500)	3 degC
Salinity (PRES<=500)	1.5 psu
Salinity (PRES>500)	0.5 psu

Test 2c: *Spike test*

The spike test follows the method outlined in Ingleby and Huddleston (2007; their appendix B), and is composed of three tests (A-C), described below, that are applied to the differences of adjacent profile values defined by DT(k)=T(k)-T(k-1) where this definition generalises to PSAL. The residual part of the profile from either temperature or salinity is rejected if one of the following conditions, written in pseudo code, holds:

<u>Test A</u>:
if
(| DT(k-1) | < Ttol OR | DT(k) | > Ttol) AND | DT(k-1) + DT(k) | < 0.5*Ttol,
then
T(k-1) is rejected as a spike,
end

<u>TEST B</u>: Only applied if k+1, k, k-1 have valid values.

if
(| DT(k-1) | > 0.5*Ttol OR | DT(k) > 0.5 Ttol) AND
there exists k where GRAD(T(k))> 0.05 degC/m AND
| DT(k-1) + DT(k) | < 0.25 * | DT(k-1) – DT(k) |,
then
T(k-1), T(k) and T(k+1) are rejected as spike,
end

<u>TEST C</u>: Applied if depths <250m

if
| DT(k-1) | > 0.5*Ttol AND | TR | < 0.5*Ttol AND -3*Ttol < DT(k) < 0,
then
T(k) and T(k-1) are rejected as spikes,
end

where DT(k) = T(k)-T(k-1), GRAD(T(k)) = T(k) – T(k-1) /(z(k) – z(k-1))

TR = $(\alpha_1 T(k+1) + \alpha_2 T(k-1))$ where $\alpha_1 = \dfrac{z_{i+1} - z_i}{z_{i+1} - z_{i-1}}, \alpha_2 = \dfrac{z_i - z_{i-1}}{z_{i+1} - z_{i-1}}$

Tests A-C are applied to temperature using the Ttol specified in Table 7. Only Tests A and C are applied to salinity using Stol also specified in Table 7.

Table 7 Tolerances used in the spike test

Variable and depth range	Tolerance
Temperature (PRES<=500)	Ttol = 5 degC
Temperature (PRES>500)	Ttol = 1.5 degC
Salinity (PRES<=500)	Stol = 1 psu
Salinity (PRES>500)	Stol = 0.2 psu

Test 2d: *Climatology*

A comparison of in situ temperature and salinity with a seasonal climatological value and annual standard deviation defined as,

$$\left|T(k) - T_{\text{clim}}(k)\right| < \sigma STD_{\text{clim}}(k)$$

where σ is assigned 5 for both temperature and salinity. The climatology test is based on the CSIRO Atlas for Regional Seas (CARS; Ridgway et al., 2002) which provides annual and semi-annual components.

3.3 OCEAN GENERAL CIRCULATION MODEL

The ocean model for both OMv1 and v2 is based on the Ocean Forecast Australia Model (OFAM), version 1 and version 2 respectively, which is a specific implementation of the GFDL Modular Ocean Model version 4.1 (MOM4p1; Griffies et al., 2010). OFAM2, developed under the BLUElink-II project, is an implementation of MOM4p1 with enhancements for preferred parameterisations for the mixed layer and penetrative solar radiation (see Appendix A) as well as a grid specification focused on Australian regions of interest.

3.3.1 Grid specification

OMv2 is based on OFAM2, which is designed as a global model with higher (eddy-resolving) horizontal resolution 0.1°×0.1° in the Australian region (90E-180E, 75S-16N). Below we describe the changes in OFAM2 that are likely to impact the performance of OMv2.

MOM4p1 includes a generalized vertical coordinate (z*) defined as (Griffies et al., 2010; pg. 109),

$$z^* = H\left(\frac{z-\eta}{H+\eta}\right)$$

where z$\in$[-H, η], -H is the model depth, η is the free-surface height. The behaviour of this grid can be examined by re-expressing in normalised form,

$$\frac{z^*}{H} = \left(\frac{\frac{z}{H} - \frac{\eta}{H}}{1+\frac{\eta}{H}}\right)$$

where z/H$\in$[-1, η/H]. **Error! Reference source not found.**shows a singularity as η→-H (i.e., η/H→-1). The advantage of z* is that finer vertical resolution can be specified than the amplitude of the η, i.e., $\Delta z_{min}<|\eta|_{max}$. However, as shown by Fig. 8, z* is only well behaved as $H \rightarrow |\eta|_{max}$ with a rule of thumb $H>2|\eta|_{max}$. Note also that for the limit $z \rightarrow \eta$, (i.e., $z^* \rightarrow 0$), indicating that $z=\eta$ must remain a prognostic variable.

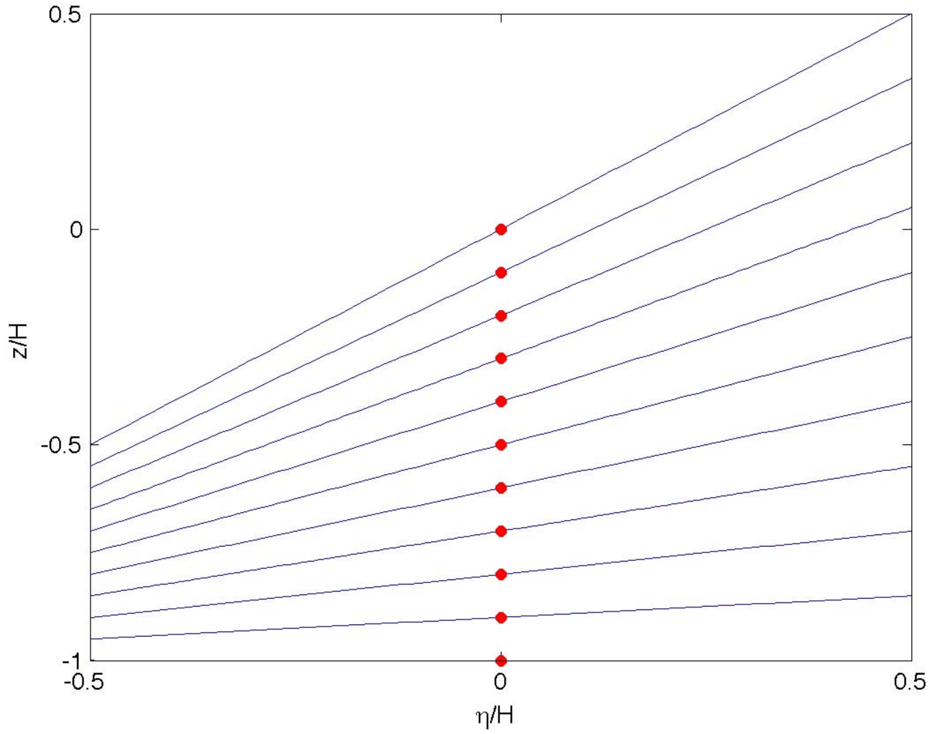

Fig. 8. Limiting behaviour of z/H as a function of η/H where $\eta \in$ [-H/2,H/2] plotted for a range of z*/H$\in$[-0.9:0.1:-0.1]. Note that z*=z for η=0 as denoted by the red dots.

The OFAM2 vertical grid has been configured with a surface cell depth of $\Delta z_{min}<5$ m. The minimum total depth is based on the top 3 cells, H=15 m. Therefore z* will be well behaved for $|\eta|_{max}<15$ m. The dynamic range of the free-surface over the open ocean for a non-tide resolving model is $|\eta|_{max}<2$ m and therefore satisfies this condition.

Over the shelf and coastal regions sea level range can be somewhat greater than over the open ocean. This is relevant operationally as OMv1 has been shown to forecast non-tidal sea level including coastal surges and coastally trapped waves with some level of skill in the mid-latitudes [4]. The dynamic range of sea level around Australia varies considerably with regions with notably large tidal ranges along the North West shelf (see Fig. 9). However, neither OFAM2 or OFAM1 represent tides and the coastal non-tidal dynamic range is typically $|\eta_{non\text{-}tidal}|_{max}<2.5$ m, which satisfies the above condition.

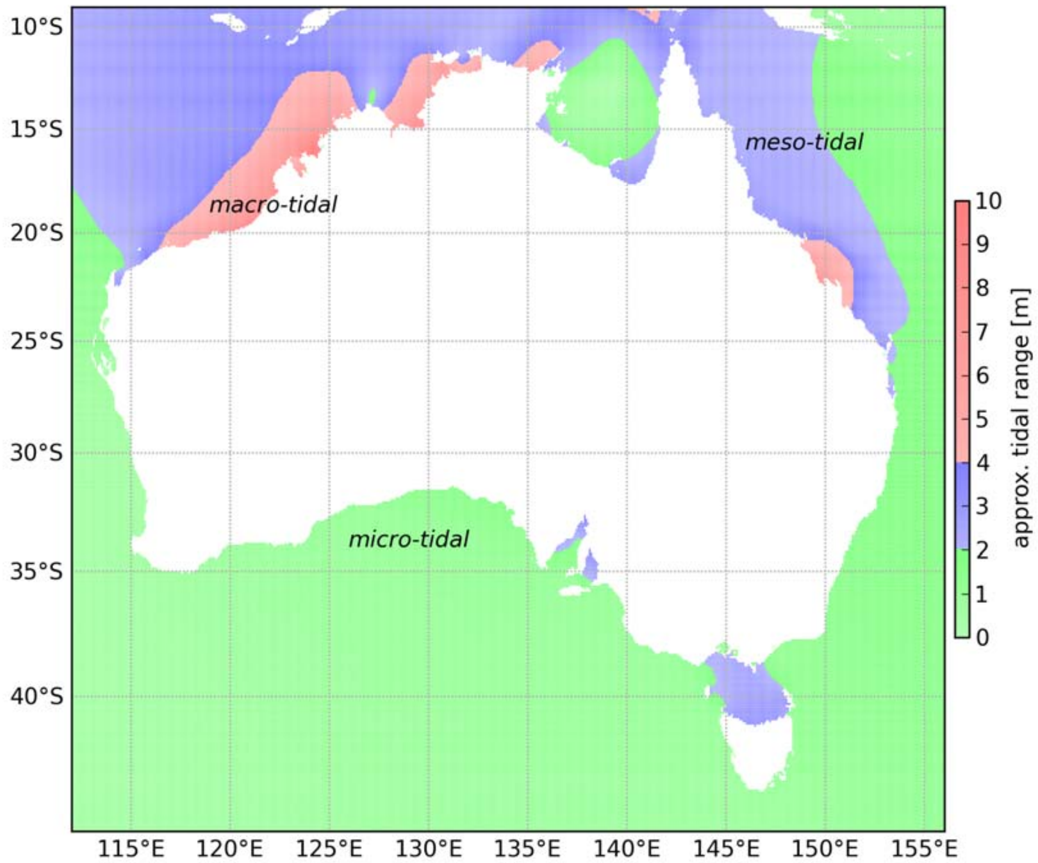

Fig. 9. Approximate distribution of sea level dynamic range across the Australia region indicated by tidal regime, micro, meso and macro tidal [source: NTC 5min regional barotropic tide model]

OFAM2 has been extended to include 51 levels for the purpose of reducing the resolution of the top 3 cells to 5 m. The resolution is smoothly graduated to coarser resolutions through a cosine function. Figure 10 shows that the two notable changes are in the upper 75 m (see Fig. 10a) and the layers below 2000m (see Fig. 10b). The latter are adjusted in order to achieve an equivalent maximum bottom depth of 5000m.

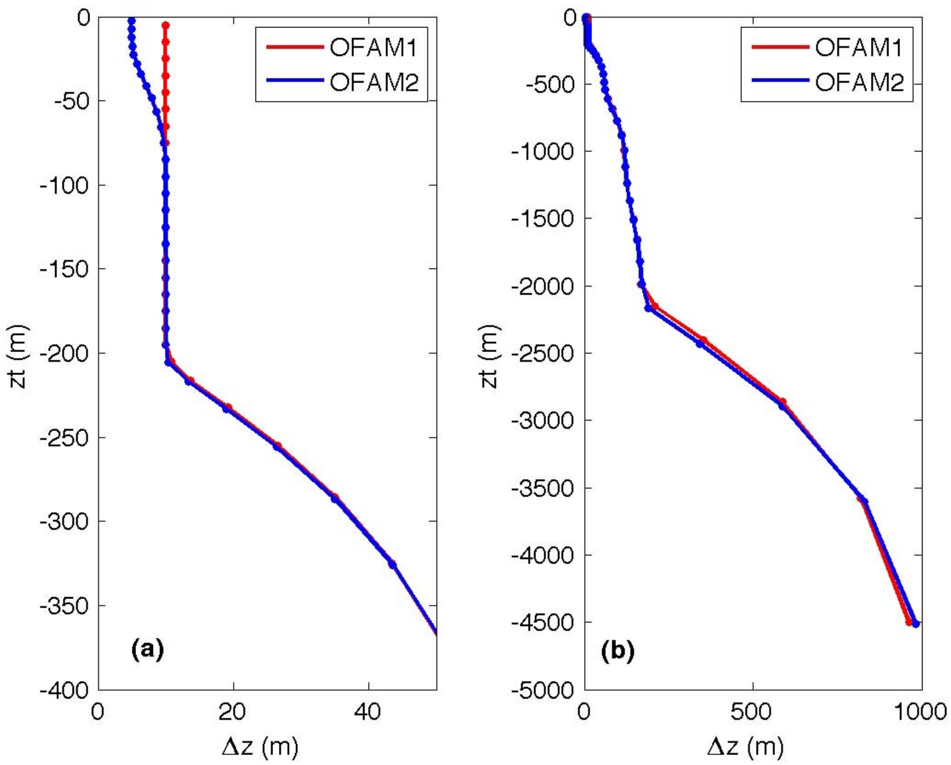

Fig. 10. Vertical resolution as a function of depth for OFAM1 and OFAM2, (a) the top 400m only and (b) the full depth.

The refinement in resolution for the surface layer permits an improved representation of diurnal warming as well as an improved representation of coastline and straits. For example the modelled bathymetry through Torres Strait, (Brassington, 2011; see figure 18.15) was identified as unrepresentative due to the 20m minimum column depth of OFAM1. The volume transport from the Coral Sea and the Gulf of Carpentaria was diagnosed to be unrealistically large. OFAM2 shows an improved representation of the shallow sections of the strait (see Fig. 11; section 142.2E).

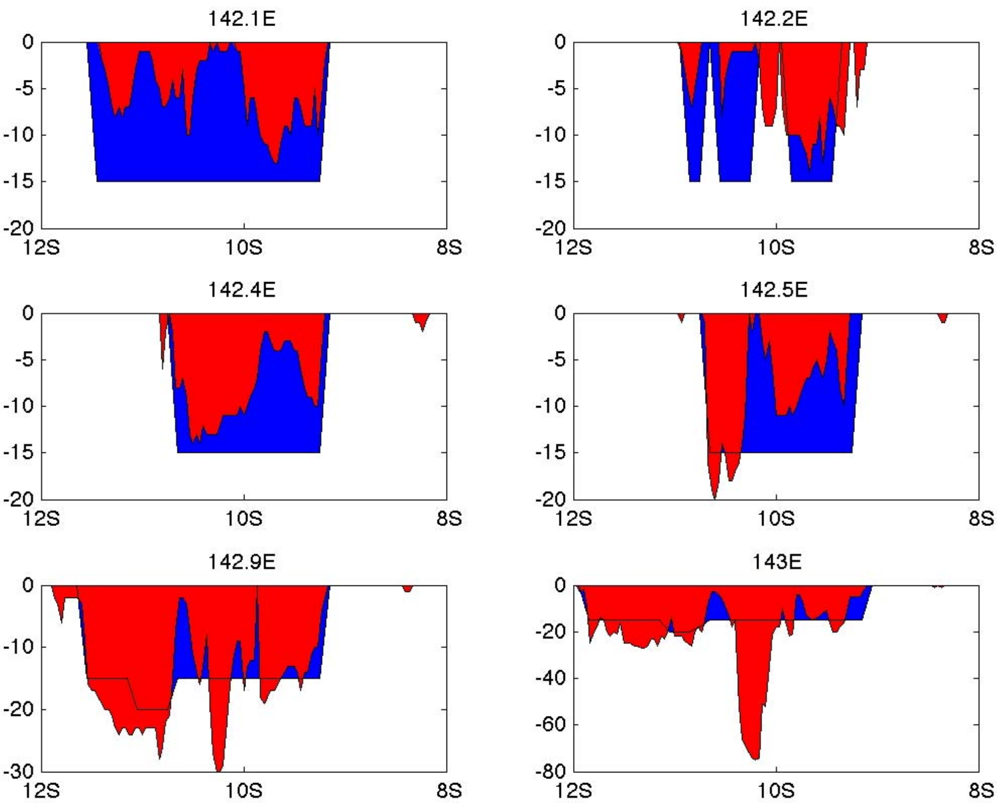

Fig. 11. Meridional-depth sections of bathymetry in the Torres Strait for a set of longitudes (between 142E and 143E) as represented by bathymetric data (red) and represented in OFAM2 (blue). The axes are chosen to correspond with (Brassington, 2011; figure 18.15).

The horizontal resolution for OFAM2 is unchanged south of 16 N with 0.1° resolution in the Australian region, 90E-180E, 75S-16N and smoothly degraded elsewhere. The only difference in horizontal resolution between OFAM2 and OFAM1 is the meridional resolution north of 16N. Specifically Fig. 12 shows the resolution is equal or less than 0.2° up to 21.9 N and equal or less than 0.5° up to 25.75 N. The purpose of these changes is to improve the latitude resolution of all of the South China Sea including the region, where the Kuroshio Current intrudes south of Taiwan in the Pacific Ocean. The latitude resolution is improved in the Red Sea, Arabian Sea, the mouth of the Persian Gulf and the Bay of Bengal in the Indian Ocean. However, the gain in the Indian Ocean is degraded by the coarsening zonal resolution which remains unchanged from OFAM1.

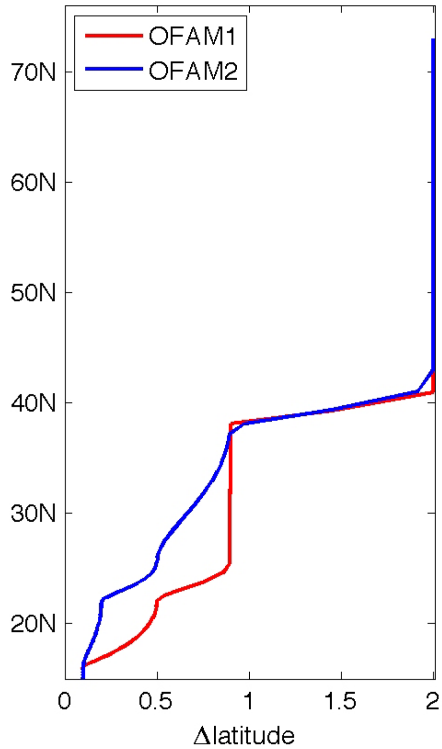

Fig. 12. Meridional resolution relative to latitudes north of 16N for OFAM1 and OFAM2. Between 74.95 S and 16 N the meridional resolution is uniform for both OFAM1 and OFAM2 (Δlatitude = 0.1°).

The strategy for bathymetry for OFAM2 was to limit the data sets to published sources only. This was a departure from the strategy for OFAM1 which involved stitching together four international and three national sources (an evaluation and merged product was developed by Jim Mansbridge, www.marine.csiro.au/~mansbrid/omas/bathymetry_gifs/). In OFAM2, the bathymetry was based on the Smith and Sandwell, version 11.1 hereafter SS (Smith and Sandwell, 1997). The SS product features a new remote sensing algorithm combined with soundings observations to improve the accuracy and resolution. The original 1 minute data is projected onto a regular 0.1 by 0.1 coarse grid as follows. A grid cell is taken to be land if the ratio of land points to ocean points is >= 0.5. Otherwise, the depth is the weighted mean of the depths (with land points replaced by zero). Thus it approximately preserves the volume of water in the coarse box. The regular coarse grid bathymetry is then projected onto the MOM4p1 grid using the MOM4p1 grid generation software. The bathymetry is then post-processed to address problems related to choke points, lakes and narrow channels.

The common horizontal resolution south of 16 N provides a close comparison between the grid_spec.nc from OFAM1 and OFAM2. Figure 13 shows the OFAM2-OFAM1 gridded bathymetry difference for the Australian region, (100E-170E, 50S-5S). It should be noted that there is a small difference of ~0.0025° in longitude which is significant near large gradients in bathymetry. The obvious large patches where the difference is zero indicate regions where the depth of the ocean exceeds 5000 m, i.e., the maximum depth of the two models is equal. To construct statistics on the distribution we exclude all land value and differences that are exactly zero. The maximum absolute difference of this sample is 3579 m. However, the differences are effectively normally distributed where 97% of the sample differences have $|\Delta H| \leq 500$ m. Figure 13 shows that the majority of large differences are related to small horizontal shifts of position for trenches and ridges. Significant changes can be seen in the Solomon Islands where deficiencies have been previously identified in

OFAM1 (private comm. Dr William Kessler, PMEL/NOAA). The majority of differences over Australia's continental shelf are small relative to the scale of the colorbar with the largest difference along the shelf break of the Great Australian Bight, the Northwest Cape and far northern Queensland.

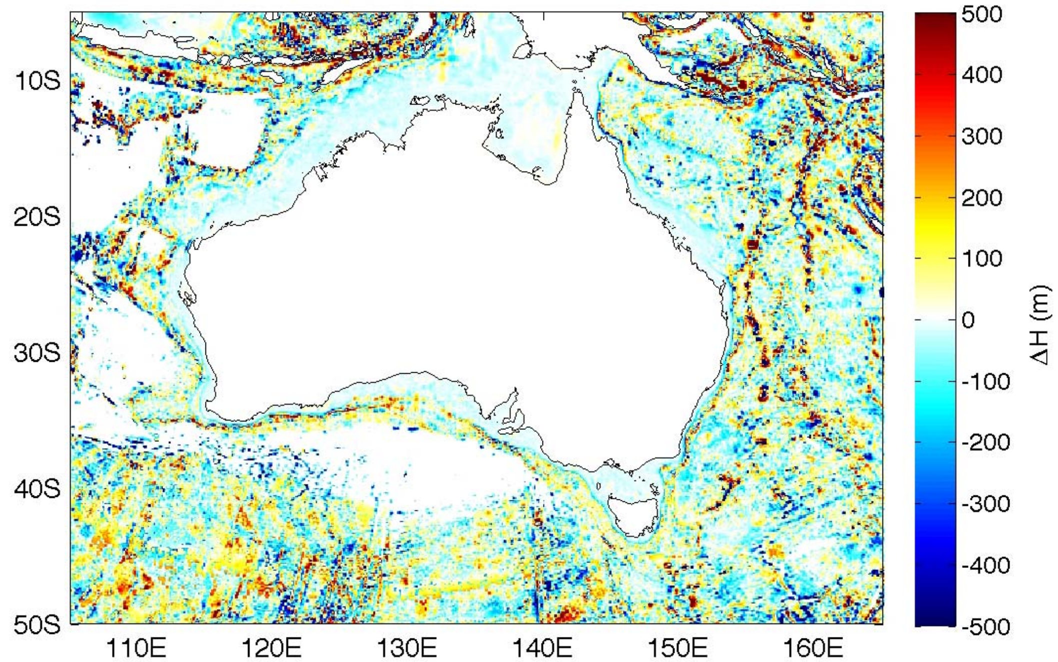

Fig. 13. Difference in depth between OFAM2 and OFAM1, (OFAM2 - OFAM1) in the Australian region. The large patches where the difference is zero indicate regions where the depth of the ocean exceeds 5000m the maximum depth of the two models.

The shelf bathymetry differences (defined by depth_t < 300 m) are shown in Fig. 14 In the shallow region we expect many cells to have differences of the two minimum column depths i.e., 20 m - 15m = 5 m. We exclude these cells from our sample. The distribution of this sample is skewed with a mean difference of $\overline{\Delta H}$ = -14.3 m, The absolute maximum difference is 2811 m which occurs at the shelf break. When we exclude cells that are land and $|\Delta H|=5$ m, 94% of cells satisfy the condition, $|\Delta H|\leq 50$ m.

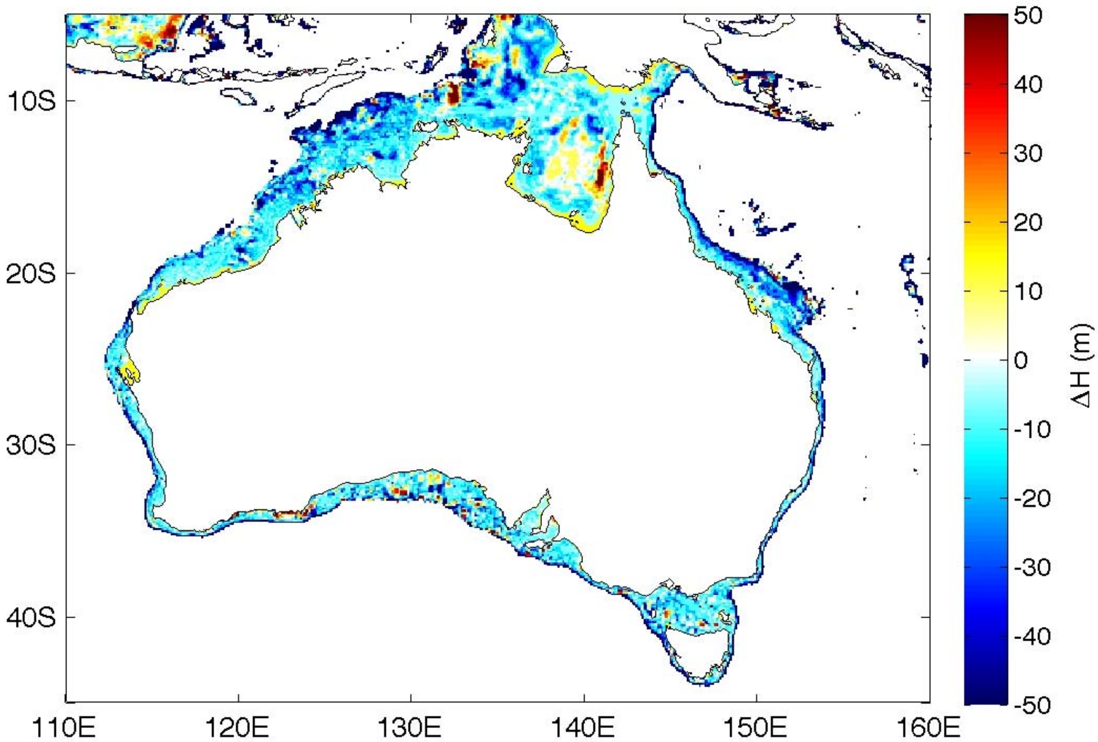

Fig. 14. Difference in depth between OFAM2 and OFAM1, (OFAM2 - OFAM1) in the Australian region for depths shallower than 300m.

The Southern Ocean is a region where the analysis in OMv1 persistently produces large increments to compensate for a model bias. Some of this model bias relates to the atmospheric winds as well as the accuracy of the bottom bathymetry. A striking feature for this region is the visible survey tracks indicating that this region is relatively poorly surveyed. The distribution of the differences is approximately normal with a mean difference of $\overline{\Delta H}$ = -6.9 m, The absolute maximum difference is 2793 m, which is a sea mount in the Tasman Sea (156.25E, 32.5S) . When we exclude cells that are land and $|\Delta H|$=5 m, 98% of cells satisfy the condition, $|\Delta H| \leq 500$ m.

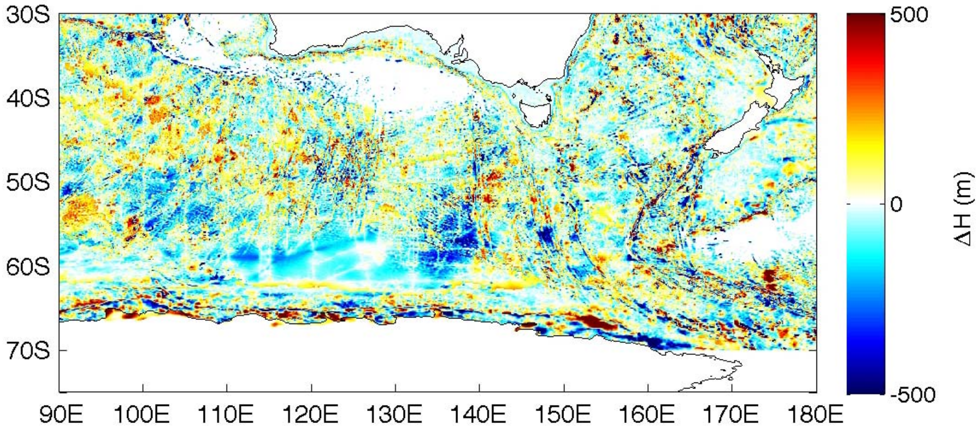

Fig. 15. Difference in depth between OFAM2 and OFAM1, (OFAM2 - OFAM1) in the Southern Ocean. The large patches where the difference is zero indicate regions where the depth of the ocean exceeds 5000m the maximum depth of the two models.

3.3.2 SPINUP mean dynamic topography

The mean dynamic topography, (MDT) of the model is an important reference from which transient mesoscale variability is a perturbation, i.e., sea surface height anomalies (SSHA). *Apriori* the MDT derived from a model will not match the observed through a combination of model biases, modelled bathymetry, assumptions for a Geoid that is a perfect sphere and errors in the applied atmospheric fluxes. We can minimise the impact of this bias by comparing the anomalies of sea surface height relative to each of the modelled and observed references rather than their absolutes. Both the construction of the background error covariances and the forecast innovations used in the data assimilation scheme, described in section 3.4, are constructed relative to the modelled MDT. Nonetheless biases in the MDT (e.g., the position of the subtropical front) have been found to contribute to biases in the data assimilation (Oke, et al., 2008; their figure 18) and will be discussed in later sections. Therefore we compare the OFAM1 and OFAM2 MDT's shown in Fig.16 to provide some guidance as to the expected biases in the data assimilation system.

Figure 17a shows the difference in MDT, MDT_{OFAM2}-MDT_{OFAM1}. There is a mean difference in the region shown of 0.37 m, which is due to the differences in the freshwater fluxes applied to the OFAM2 simulation. The largest positive differences relative to the mean lie along distinct dynamical features such as the subtropical front, the Tasman front, the Gulf of Papua Gyre, across the Torres Strait and features in the South China Sea. The largest negative differences, relative to the mean difference lie south of the subtropical front and along the edge of Antarctica. In order to improve our attribution and interpretation of these differences we apply a Hanning filter to the MDT shown in Fig. 16 to separate the large spatial scale mass distribution from the fine scale features. The Hanning filter is based on two-dimensional Gaussian weighting function with an e-folding scale of 1° and applied over a region of +/-5° with a simplistic adjustment for land points. These parameters are chosen based on a typical mesoscale scale of ~2° lying within the first e-folding scale of the weight function. It is noted that the filtering near elongated islands may introduce errors as the MDT either side may not be continuous across. Large aspect ratio islands may not be related and should be excluded from the smoothing. The difference between the two Hanning filtered MDT's is shown in Fig. 17b. There is a broad change in the distribution of mass across the subtropical front toward an increase in mass north of the front compensated by a loss of mass south of the front. We attribute this to a strengthening of the westerly wind stress over the Southern Ocean from the ERA-interim (Dee et al., 2011) reanalysis compared with the ERA-

40/ECMWF (Kallberg et al., 2004) products used for the OFAM1 spinup. There are weak but notable increases in the mass for the East Australian Current (EAC) and Leeuwin Current (LC) local to the mean separation point(s) suggesting a sensitivity in the mean separation point to the changed shape of the shelf from the bathymetry product, vertical resolution and minimum column depth. There is an increase in mass in the SEC of the Pacific Ocean, the tropics of the North Pacific, the South China Sea and Indian Ocean equatorial region which are similarly attributable to changes in the trade winds for El Nino-Southern Oscillation and Indian Ocean Dipole.

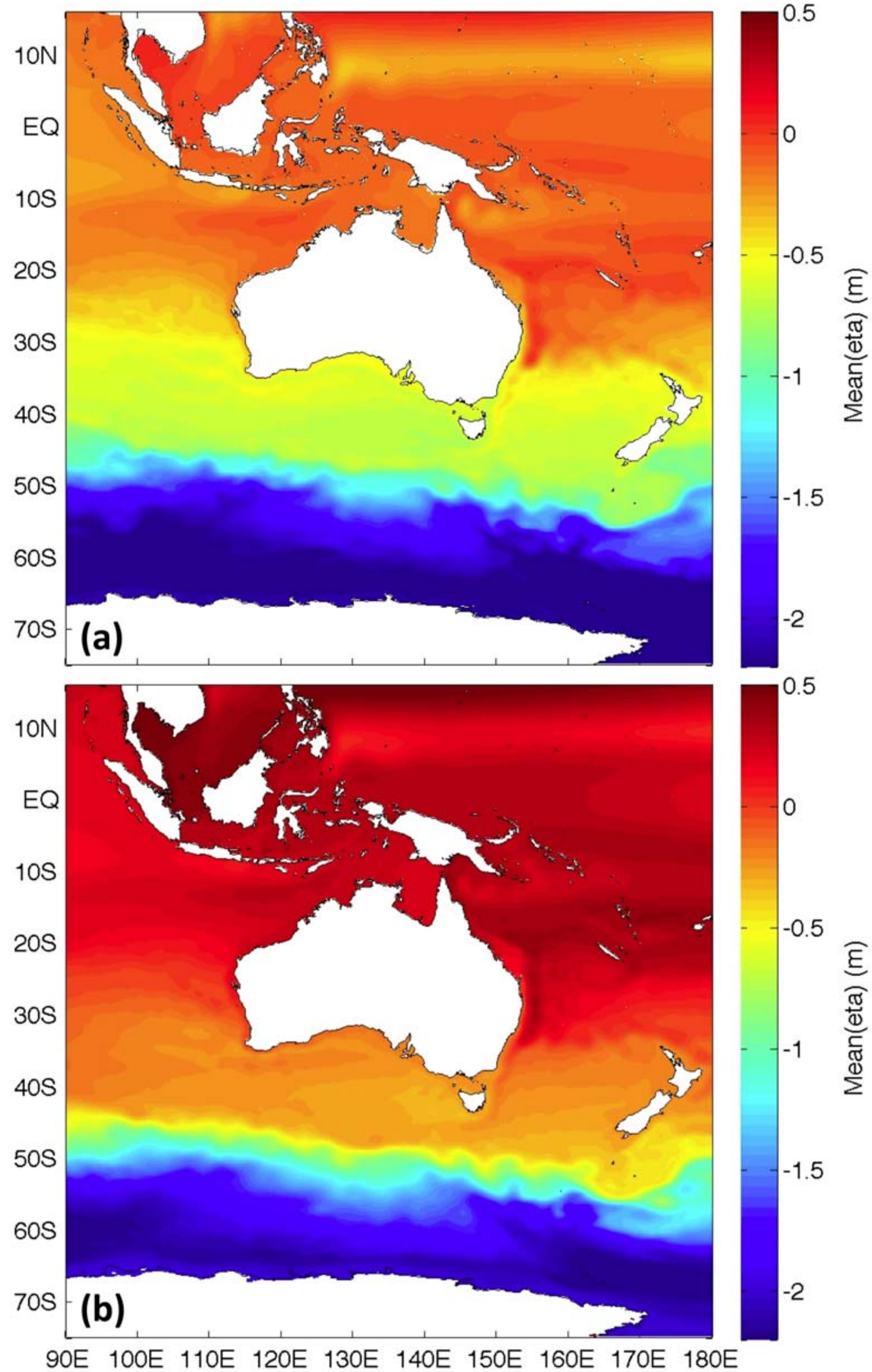

Fig. 16. Modelled mean dynamic topography (a) OFAM1 spinup (1994-2004) and (b) OFAM2 spinup (1994-2008)

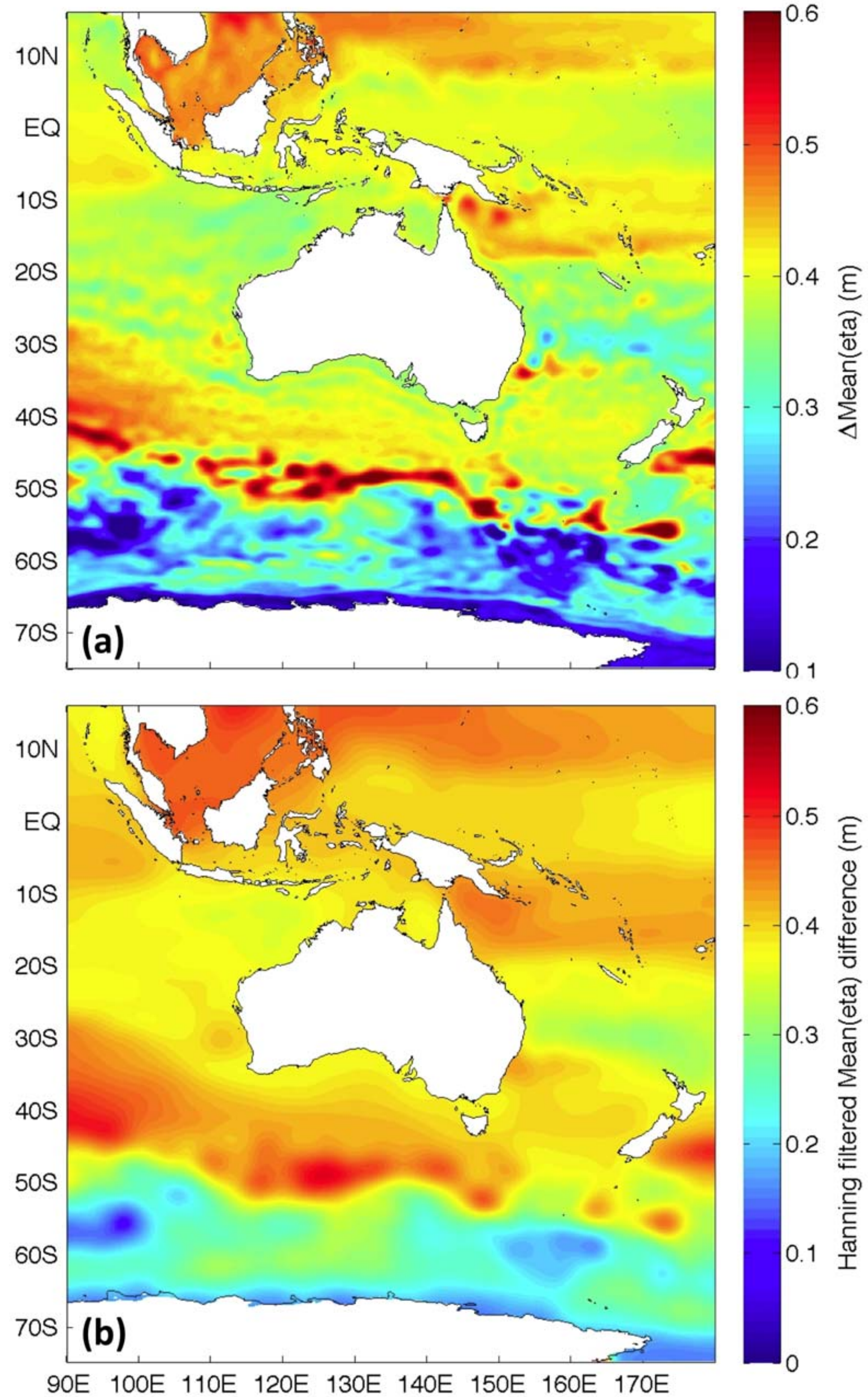

Fig. 17. A comparison of the mean dynamic topography from OFAM1 and OFAM2, (a) the difference, MDT_{OFAM2} - MDT_{OFAM1}, (b) the difference in the Hanning filtered MDT, Hanning(MDT_{OFAM2})-Hanning(MDT_{OFAM1}).

The residual "mesoscale" MDT obtained from the difference of the original MDT with the Hanning filtered MDT is shown for OFAM1 and OFAM2 in Figs. 18 a and b. Both OFAM1 and OFAM2 show clear correspondence in the majority of peak features with the main difference related to a general reduction in amplitude for OFAM2. In part, this could be explained by the additional four years averaging period for the OFAM2 MDT. Figure 18b shows an increase along the coast in the Gulf of Siam, which is sensitive to the improvements in vertical resolution and minimum column depth. **Error! Reference source not found.**b shows a reduced amplitude in negative sea surface height for the Papua Gyre indicating a reduction in the cyclonic circulation and transport through the Solomon Islands. Figure 18b shows a decline in the amplitude off the Antarctic coast indicating a weaker boundary current. Figure 18b shows a decline in amplitude along the subtropical front southeast of Australia however, the amplitude has remained comparable southeast of Australia. There are numerous small differences to the high amplitude features along the subtropical front including small changes in position, amplitude, merging and separation. The most striking new feature occurs along the edge of Campbell Plateau where a high sea surface height, anticyclonic circulation is present at approximately (173E, 55S) in the OFAM2 MDT. This occurs where the position and importantly the shape of the edge of the Campbell Plateau has changed as shown in Fig. 15.

It should be noted that OMv2 includes the Bureau of Meteorology operational ACCESS-G surface fluxes. At present OMv2 uses the MDT derived from the OFAM2 SPINUP integration and no account is made for differences in atmospheric biases. In practice the operational ACCESS-G system is only available for a short period, maximum one year, which is insufficient to diagnose an MDT for the OMv2 system. The comparison of the MDT's obtained from OFAM1 and OFAM2 indicate there is considerable sensitivity when using different atmospheric sources. It is reasonable to assume that a similar magnitude and distribution of differences will occur with the use of ACCESS-G. An alternative approach to diagnose the model bias for OMv2 is based on the data assimilation, which is discussed in section 4.1.

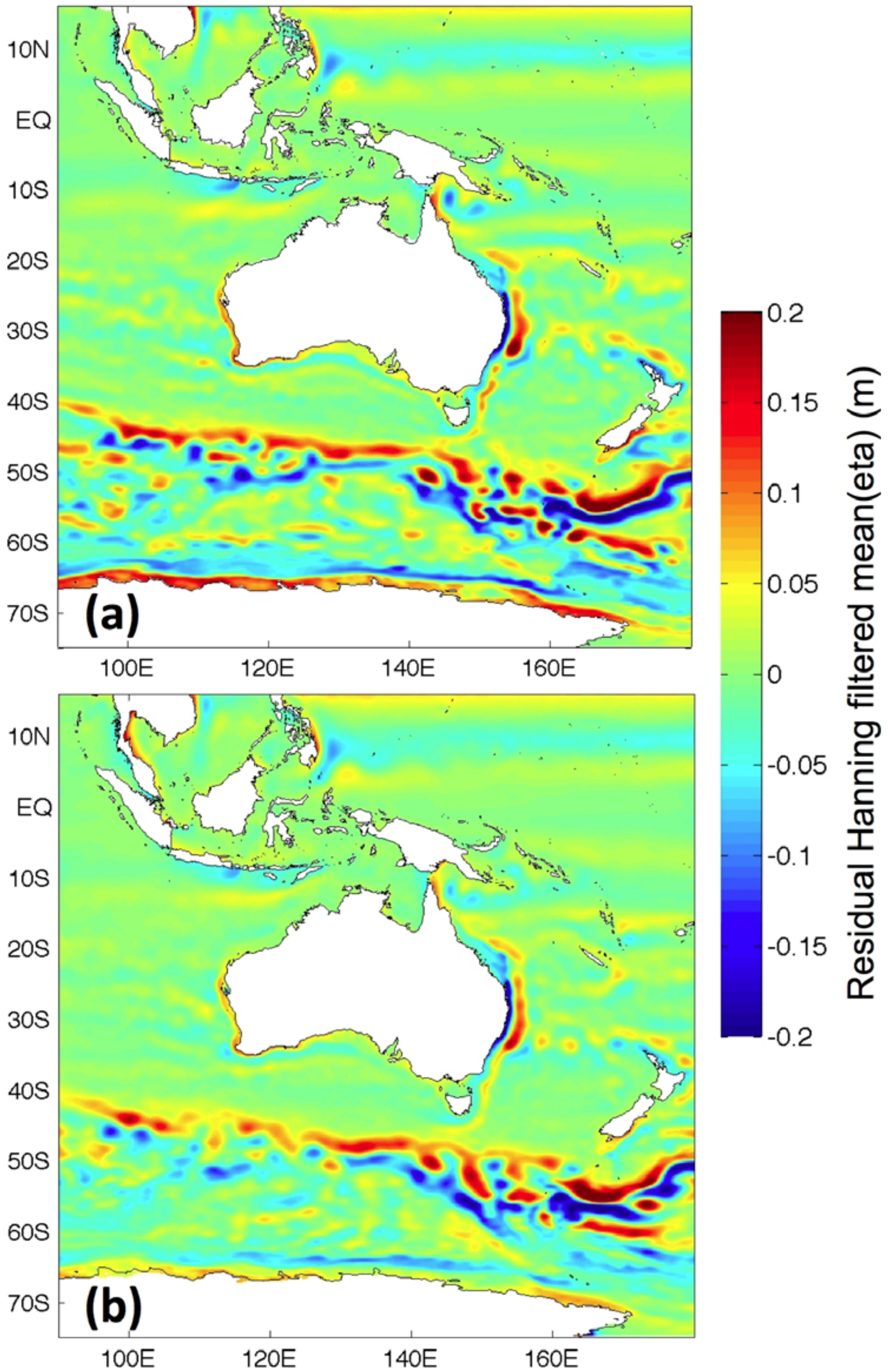

Fig. 18. Residual from the Hanning filtered modelled mean dynamic topography for (a) OFAM1 and (b) OFAM2

Recent evidence suggests that the ocean has quasi-zonal mean-jets that contribute to the mean dynamic topography such as the so-called zonal striations (Maximenko et al., 2005). In the southeast Indian Ocean these features are pronounced in not only the ocean models but also the mean dynamic topography derived from satellite altimetry (Divakaran and Brassington, 2011). We note that the residual Hanning filtered MDT for OFAM1 and

OFAM2 Fig. 19 shows a comparable distribution of alternating quasi-zonal anomalies in the Southeast Indian Ocean. However, we note that OFAM2 has a weaker amplitude indicating that the model reproduction of these features is sensitive to model configuration and atmospheric forcing. Other notable features in Fig. 19 include: a reduced amplitude for the extension of the South Australian Current to the west coast of Tasmania; greater continuity of the East Australian Current near the mean separation point ~34°S; more pronounced standing eddies along the Tasman Front; weaker South Equatorial Current in the Indian Ocean.

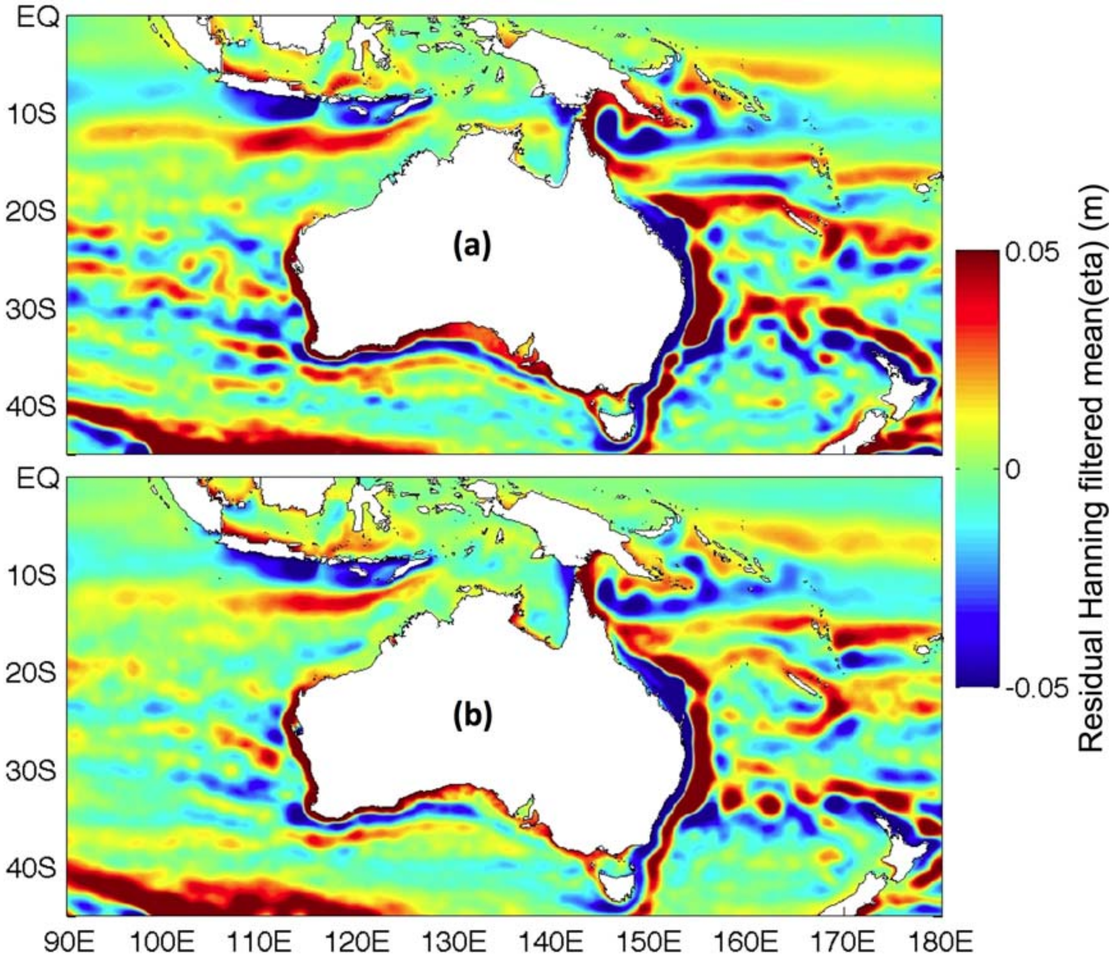

Fig. 19. Same as Fig.18 but focused on the mid-latitudes and tropics with reduced a dynamic range for (a) OFAM1 and (b) OFAM2

3.3.3 SPINUP variability

Figure 20 (left column) shows the standard deviation of the total model variability derived from the OFAM1 SPINUP in the Australian region. This field was used as a quality control step applied to forecast innovations in BODAS for OceanMAPSv1 i.e., (forecast innovation)/(standard deviation) < threshold. Figure 20 (right column) shows the standard deviation of the intra-seasonal anomalies derived from the OFAM2 spinup integration in the Australian region. The definition is consistent with the error model used in BODAS2 and is applied at the equivalent quality control step in BODAS2 and OceanMAPSv2. A comparison between the total and intraseasonal variability shows that the latter is at least an order of magnitude weaker and confined to specific regions of large geostrophic turbulence. The variability is restricted to the surface variables SSHA (Figs. 20a and b), SST (Figs. 20c and

d) and SSS (Figs. 20e and f). Figure 20b shows the highest energy regions are largely located along the coast which will be discussed later in the context of Australia. In the open ocean the highest variability occurs in the ACC and in particular along the south face of Chatham Rise. Other identifiable regions include the Tasman Sea associated with the EAC, southeast Indian Ocean associated with the LC, the tropical Indian Ocean related to the South Equatorial Current and Indonesian Throughflow, and the tropical Pacific Ocean related to the South Equatorial Current and extension through the Solomon Islands.

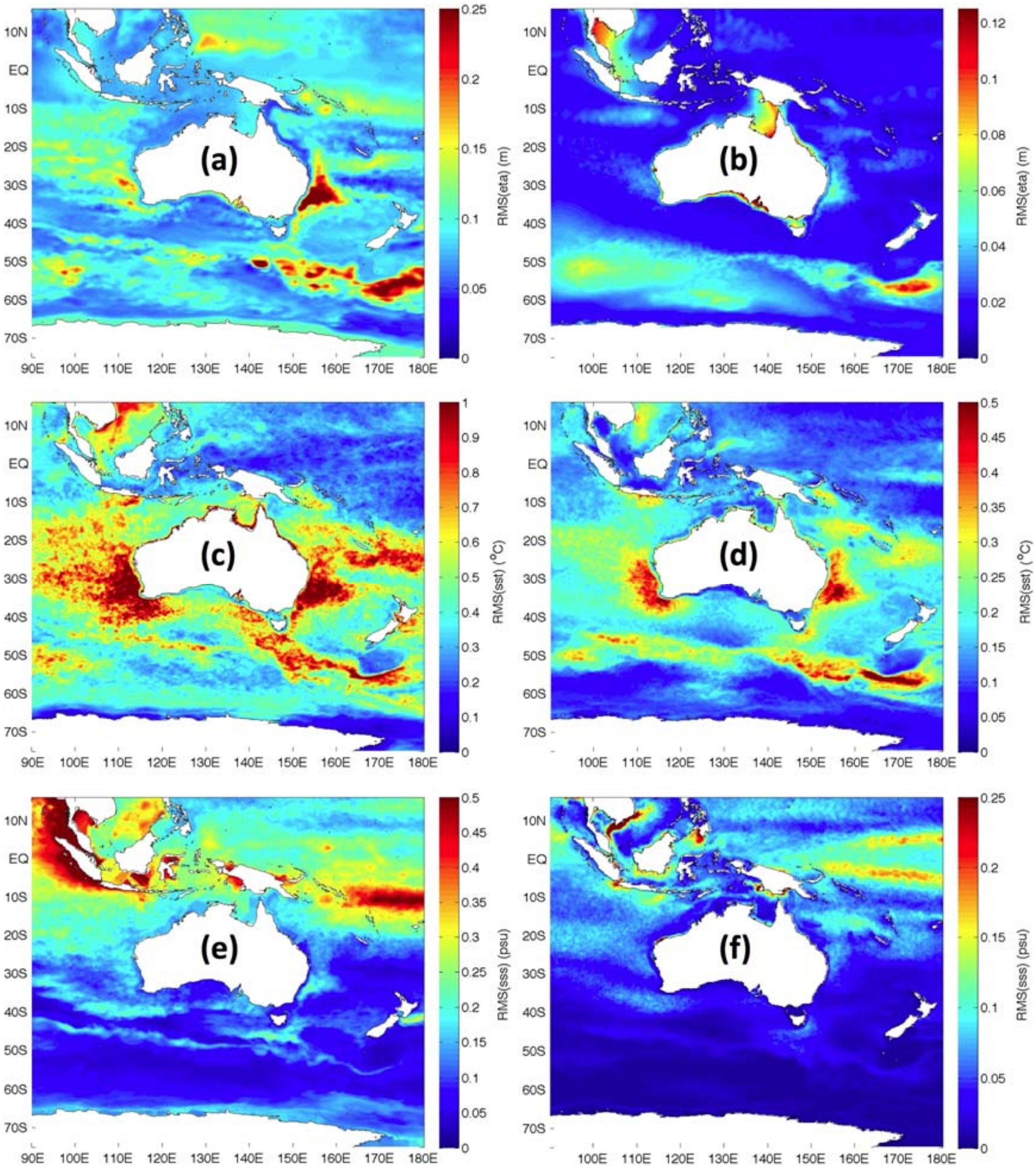

Fig. 20. Root mean square of surface variables derived from the OFAM1 spinup (1994-2006) and OFAM2 spinup (1994-2008) in the Australian region: (a) $SSHA_{OFAM1}$, (b) $SSHA_{OFAM2}$, (c) SST_{OFAM1}, (d) SST_{OFAM2}, (e) SSS_{OFAM1} and (f) SSS_{OFAM2}.

The distribution of root mean square of SST over the open ocean in the mid- and high-latitudes is comparable to that of SSHA. Additional RMS of SST is present in the tropical

Pacific which corresponds to a similar band of SSS in Fig. 20f. The largest RMS of SSS is located in the tropics corresponding to the position of atmospheric convergence zones. Other important regions of RMS of SSS include the northern extent of the EAC, southeast Tasmania, an extension of the LC between the Naturaliste and Broken Plateau and the mid-latitude at approximately 20S. Figure 21a shows the equivalent SSHA variability for the Australian continental shelf (<200 m) noting that this is non-tidal. The highest RMS is located in the Gulf of Carpentaria, Great Australian Bight, Bass Strait, which is consistent with the known regions.

The highest RMS of SST over Australia's continental shelf occurs in the tropics with visible extension along the east and west boundaries through the EAC and LC. Higher RMS is also present in Spencer Gulf, Gulf Saint Vincent and Bass Strait. The high RMS of SSS over the continental shelf corresponds to that of the climatological river discharge shown in Fig. 28 and described in section 3.6.3. We note that the RMS for SSHA and SST over the continental shelf for OFAM1 shows the same distribution as OFAM2, though larger in magnitude. The distribution of SSS RMS over the continental shelf for OFAM1 is dominated by the seasonal variability of the tropic monsoon. This variability is absent from the intra-seasonal anomalies of OFAM2, Fig. 21b.

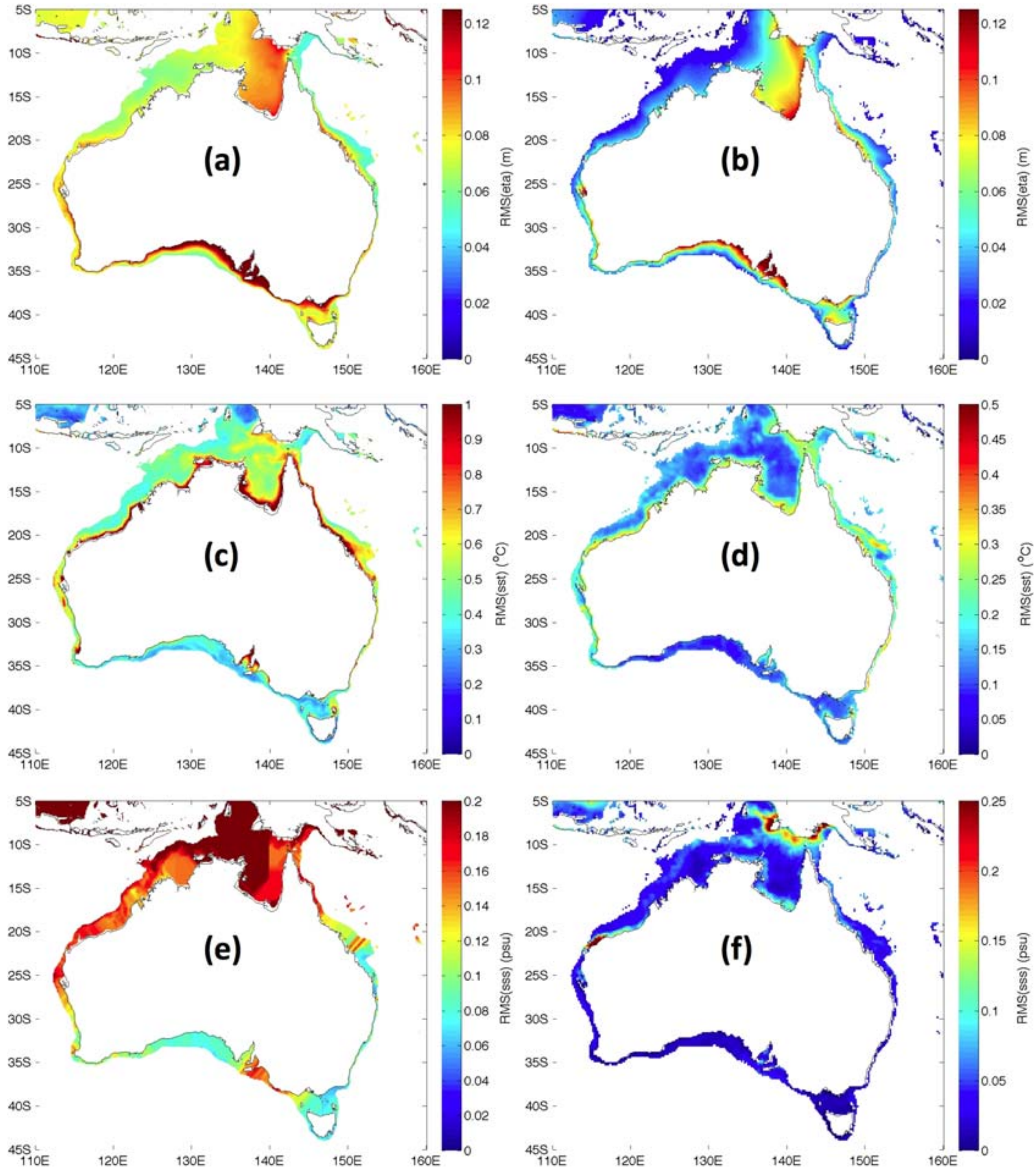

Fig. 21. Standard deviation of surface variables derived from the OFAM1 spinup (1994-2006) and OFAM2 spinup (1994-2008) over the modelled continental shelf (<200m): (a) $SSHA_{OFAM1}$, (b) $SSHA_{OFAM2}$, (c) SST_{OFAM1}, (d) SST_{OFAM2}, (e) SSS_{OFAM1} and (f) SSS_{OFAM2}.

In the open ocean and the continental shelf the intra-seasonal variability is significantly lower in magnitude requiring a refined criteria for the quality control. The criterion being used is σ=100.

3.4 OCEAN DATA ASSIMILATION SYSTEM

The BLUElink Ocean Data Assimilation System, (BODAS) is an ensemble optimal interpolation method (Oke et al., 2008; Oke et al., 2009) able to produce multivariate analyses of the ocean state, its latest version (BODAS2) has been implemented as the assimilation component of OceanMAPSv2

3.4.1 Options

The configuration of BODAS is determined by a suite of parameters that can be modified for any given application. A selection of parameters and setting for OceanMAPS follows.

Namelist what_obs: determines what observation types are to be assimilated; SLA refers to sea-level anomalies from altimetry and coastal tide gauges; tprof refers to temperature profiles from Argo, XBT, and tropical moorings; sprof refers to salinity profiles from Argo, and SST refers to satellite SST from AMSRE and/or AVHRR sources.

Namelist time_window: determines the time window of observations to be assimilated. A different time window for sea-level (eta), SST, and temperature and salinity (ts) can be set. For this example, minus_eta=5 and plus_eta=5 means that SLA from altimetry and coastal tide gauges are assimilated for the analysis day, plus and minus 5 days – totally 11 days of data. The entries sla_super_ob_file, sst_super_ob_file, and ts_super_ob_file set the nominal resolution of the super-obing, and can be set for different regions. If these files are missing, the nominal resolution of the super-observations is set to the variable default_super_ob_res_in_degrees.

Namelist data_types: determines the data to be assimilated: enact_ts, bom_ts, etc refer to different sources of in situ T/S data; ers_sla, Jason_sla etc refer to different sources of along-track altimeter data; amsre_sst, hr_rey_sst etc refer to different sources of satellite SST data; read_amsre_asc is true is both the descending and ascending swaths of AMSRE data are to be assimilated (false is only the descending swaths are assimilated).

Namelist method: sets the localising length scales, the ratio of the halo around each sub-domain to the localising length-scales (1.0 means that all data that could impact an analysis are used). There are several options for the inversion method (inv_method) including petsc (a conjugate gradient approach), svd_robust (a slow but very robust method using an SVD decomposition of the innovation covariance matrix), cholesky (a fast, but less robust method), and others.

The logical normalise_by_obs_error means that the innovation covariance matrix, M:

$$M = HA\ (HA)^* / (n_{ens}-1) + R,$$

where HA is the ensemble interpolated to the observations, R is the observation error covariance matrix, n_{ens} is the ensemble size, and the * denotes a matrix transpose, is reexpressed as:

$$M^{norm} = HAR^{-1/2}\ (HAR^{-1/2})^* / (n_{ens}-1) + I$$

prior to inversion. Similarly, the innovation vector is normalised to $dw^{norm} = R^{-1/2}\ dw$. This can improve the condition of the innovation covariance matrix, making its inversion more accurate.

The logical adaptive_domains means that the size of each sub-domain is adjusted according to the spatial density of observations, so that the number of observations for each inversion is approximately “approx_num_obs_per_inversion”.

Table 8 Comparison of the options for the behind real-time analysis for OMv1 and OMv2

Option	OMv1	OMv2
n_ens	72	144
minus_ts, plus_ts	1, 1	5, 5
zonal_loc_len_scl_in_deg, merid_loc_len_scl_in_deg	8.0, 8.0	8.0, 8.0

3.4.2 Super observations

BODAS2 introduces a tiling strategy for the calculation of super-observations. The user can specify multiple tile areas and resolutions. These tile areas must be unique and cover the whole model domain. This feature has been introduced to permit scaling of the super-observation density with the model resolution regions. This improves the computational performance with limited impact to the performance of the analysis globally and no impact to the high resolution target region (within the length scale of localisation). The distribution of super-observation resolution for SSHA and SST is shown in Fig. 22a and for profiles of T/S in Fig. 22b.

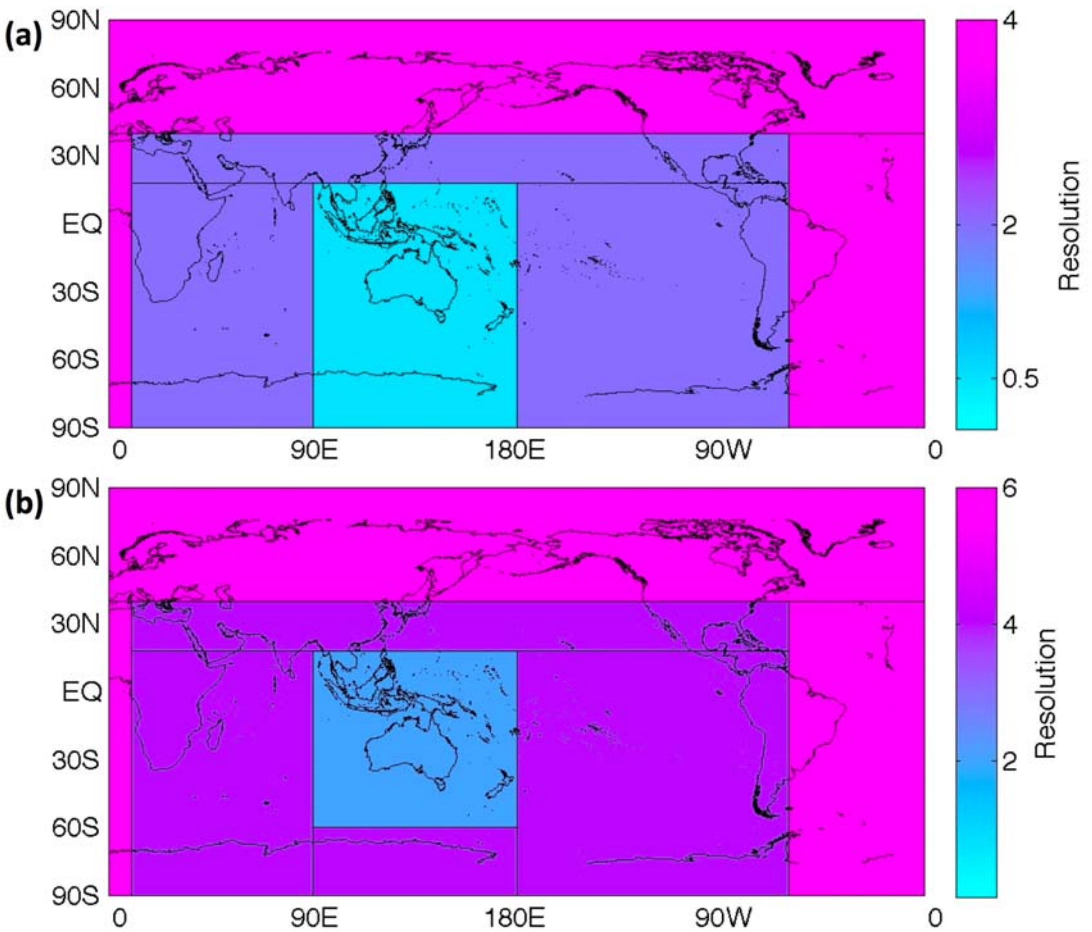

Fig. 22. The regions and corresponding resolutions (°) used to construct super-observations, (a) SSHA (same as SST) and (b) profiles.

3.4.3 Background error covariance

BODAS2 is an ensemble optimal interpolation scheme where the ensemble is defined based on the variability of OFAM2. The background error covariance is constructed from a stationary ensemble of monthly anomaly state vectors constructed from a multi-year spinup integration of OFAM2 described earlier. Specifically the anomalies are equivalent to the daily averaged model state relative to the monthly averaged model state.

$$T' = \overline{T}^{\mathrm{1day}} - \overline{T}^{\mathrm{1month}},$$

The one-day average is based on the 15th day from each month providing 12 ensemble members per year of spinup integration. The subsequent ensemble is then detrended and averaged onto a 0.2°×0.2°, half the resolution of the model grid for computational efficiency. The ensemble used in OMv1 is constructed using the same method based on the spinup integration for OFAM1 but uses a more conservative error model,

$$T' = \overline{T}^{\mathrm{3day}} - \overline{\overline{T}^{\mathrm{1month}}}^{15\,years}$$

where the 3 day average is centred on the 15th day of each month and the seasonal mean is averaged over all years of the spinup integration.

A 144-member ensemble is used in OMv2 compared with a 72-member ensemble in OMv1. The number of ensemble members is constrained by the computational efficiency of the BODAS software, both in terms of memory and computational cost, as well as the limitation of the number of years of spinup integration.

The region of positive correlation coefficient surrounding a target location indicates the area of influence represented in the ensemble. In the absence of other observations this provides an indication of how innovations from observations at the target will be projected into the analysis in the rest of the domain. This also provides a useful basis to compare the behaviour of the new ensemble. Figure 23 shows the spatial correlation for sea surface height anomaly from the ensemble of OFAM1 for different positions along 34S, Figs. 23a-c representing the points at that latitude and longitudes 153E, 154E and 155E respectively. This latitude is just to the south of the approximate mean separation point for the EAC, 32.5S, Godfrey et al., (1980). South of the separation point the EAC pinches off anticyclonic eddies that can propagate slowly along the coast. In OFAM1 the spatial scale of the autocorrelation features off the coast, Figs. 23a and b, are significantly greater than in OFAM2, Figs. 23d and e. The spatial extent of the autocorrelation features in OFAM2 is in general shorter, more symmetric (i.e., Gaussian) than the corresponding OFAM1 ensemble.

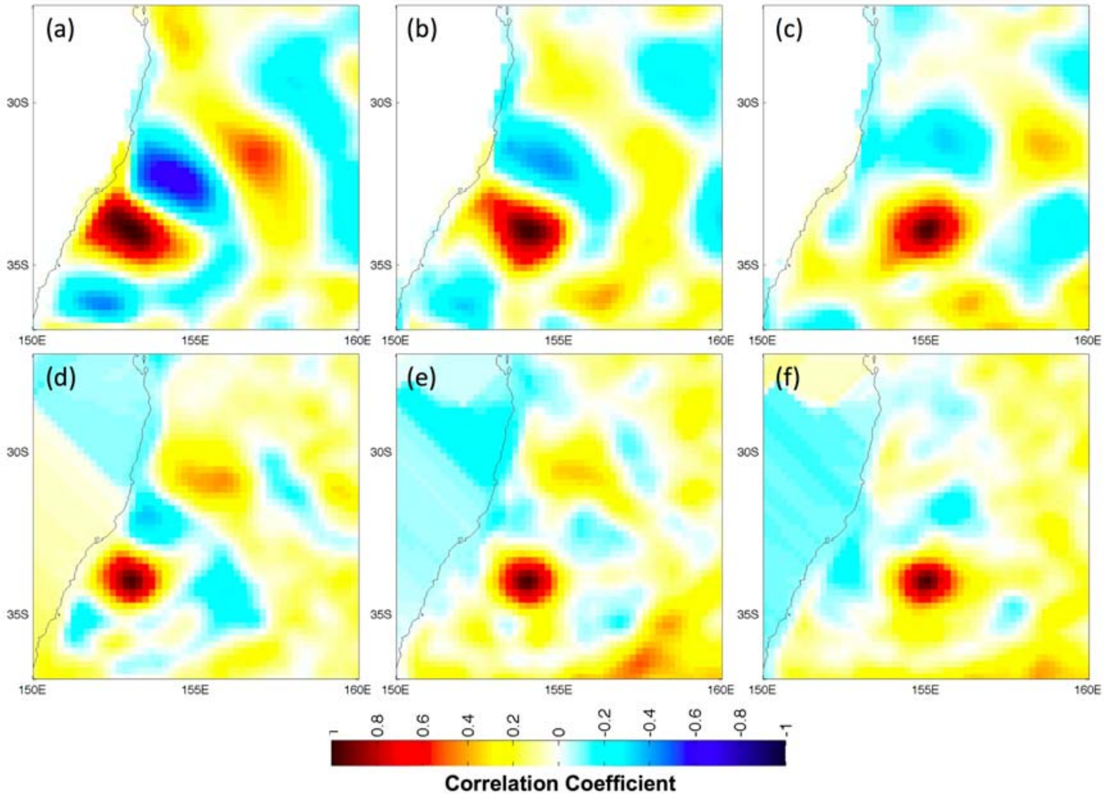

Fig. 23. Spatial correlation coefficient of the ensemble for sea surface height anomalies used in BODAS relative to a target position. The target positions in the Tasman Sea for OFAM1 are, (a) 153E, 34S, (b) 154E, 34S, (c) 155E, 34S. The corresponding target positions for OFAM2 are (d) 153E, 34S, (e) 154E, 34S, (f) 155E, 34S.

The correlation pattern obtained in the Southeast Indian Ocean, Fig. 24 shows a similar reduction in spatial extent for the OFAM2 ensemble. It is also noted that in general the spatial scale in this region is shorter than in the Tasman Sea. In this respect the requirements in terms of altimetry spatial coverage are greater and the error model used in the latest version potentially optimistic and sensitive to real-time observation drop outs that occur from time to time and the expected failures of the Jason1 and/or Envisat altimeters.

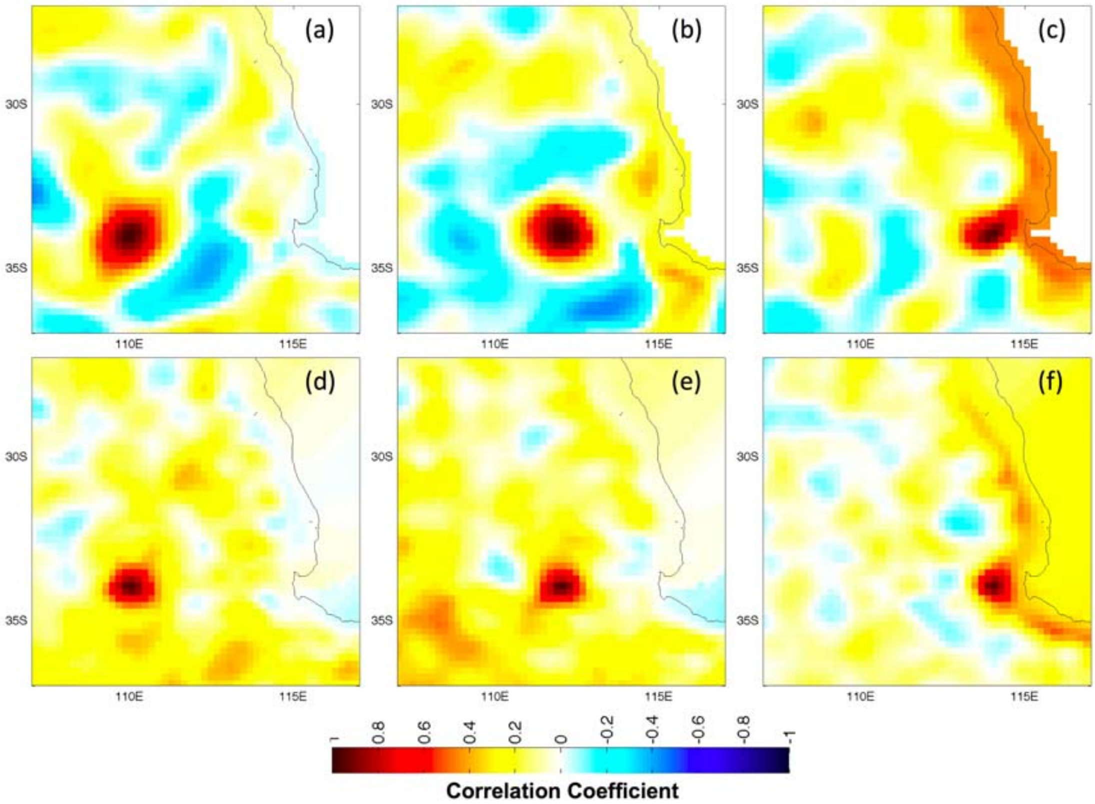

Fig. 24. Spatial correlation coefficient of the ensemble for sea surface height anomalies used in BODAS relative to a target position. The target positions in the South East Indian Ocean for OFAM1 are (a) 110E, 34S, (b) 112E, 34S, (c) 114E, 34S. The corresponding target positions for OFAM2 are (d) 110E, 34S, (e) 112E, 34S, (f) 114E, 34S.

3.4.4 Observation error covariance

In BODAS version2, it is assumed that the observation errors are uncorrelated, rendering the observation error covariance matrix diagonal. The diagonal elements of this matrix are the estimated observation error variance. Typical applications of BODAS use a relatively long time window of observations for each analysis so that most of the assimilated observations do not correspond to the analysis time. We have not yet implemented the so-called first-guess at appropriate time (FGAT) method (Huang et al. 2002). Therefore, to be consistent, we assign observations made several days before or after the analysis time a lesser weight by inflating the assumed observation error variance according to the time difference of the observation and the analysis time. We refer to this time difference as the "age", using only the absolute value of the time difference. The observation error variance e^2_o for an individual observation is here defined as:

$$e^2_o = e^2_{instr} + e^2_{RE} + e^2_{age}$$

where e^2_{instr} is the estimated variance of the instrument error, e^2_{RE} is the estimated variance of the representation error (RE), sometimes referred to as the error of representativeness, and e^2_{age} is the estimated variance of the error associated with the relative age of an observation. The estimates of e^2_{instr} are listed in Table 9, along with the range of values for e^2_{RE} and e^2_{age}.

Estimates of e^2_{age} are given by:

$$e^2_{age} = RMS_{mod}\,[1 - \exp(-0.5\,|\,t_a - t_o|\,/\,t_{ef}\,)]$$

where RMS_{mod} is the spatially dependent root-mean-square of the model fields about a seasonal cycle during the spin-up run; t_a is the analysis time; t_o is the time of the observation; and t_{ef} is an *e*-folding time scale (here 3 days), following Oke et al. (2005). Therefore, if an observation is made at the analysis time, $e_{age} = 0$; and as $|t_a - t_o|$ increases, e_{age} approaches RMS_{mod}, so that the influence of the observation on the analysis decreases. If, for example, the observation time is 4 days before and after the analysis time, the $e_{age} \sim RMS_{mod}/2$.

Estimates of e_{RE} are calculated using the method described by Oke and Sakov (2007). This method provides estimates of RE for T, S and sea-level that reflect the variance of unresolved mesoscale variability in the ocean.

Table 9 Estimates of the instrument error of different observation platforms; and the range of values for e_{RE} and e_{age}. The lower range of e_{RE} is for observations in the high-resolution region; and the upper range of e_{RE} is for observations in the coarse resolution region. The lower range of e_{age} is for observations that occur at the analysis time; and the upper range of e_{age} is for observations made 5-days before or after the analysis time in regions where the model's variability is greatest.

Platform	e_{instr}	e_{RE}	e_{age}
GFO	5 cm	2-18 cm	0-20 cm
T/P, Envisat, Jason-1, Jason-2	3 cm	2-18 cm	0-20 cm
CTG	3 cm	1-3 cm	0-4 cm
AMSR-E SST	0.25 C	0-2 C	0-2 C
CTD/Argo/TAO-S	0.05 psu	0-1 psu	0-1 psu
CTD/Argo/TAO-T	0.1 C	0-3 C	0-4 C
XBT	0.2 C	0-3 C	0-4 C

3.5 INITIALISATION

A nonlinear or adaptive relaxation procedure has been implemented where the e-folding timescale, τ, is constructed as a function of the model-target difference, $|\psi_{model}-\psi_{target}|$, following (Sandery et al., 2010b). The forcing term is defined as,

$$\frac{\partial \psi}{\partial t} = -\alpha(\psi - \psi_{target})$$

where $\alpha=1/\tau$ and the e-folding timescale is defined by,

$$\tau = \tau_{min} + \zeta \left| \frac{\psi_{target} - \psi}{\Delta \psi_{max}} \right|^{-1}$$

where τ_{min} controls the minimum timescale or maximum weighting and $\zeta = -\lambda/\ln|1-A|$ is an empirical scaling parameter and the tuning parameter *A* is within 0<*A*<1. We limit τ by a minimum threshold for stability τ_{min} that represents the maximum allowable weighting. An analysis of the restoring scheme shows that for large differences the scheme asymptotes to a linear restoring scheme with e-folding timescale τ_{min}. The timescale assumes larger values as the differences reduce to zero. Analyses of this scheme show that the regions where the model tendency is weak and in approximate dynamical balance the relaxation term is weak, whilst for regions with large tendency the restoring term remains large. An example for the

OMv2 system is shown in Fig. 25. In the mid-latitudes, the eddy core T/S is restored whilst at the fronts the restoring term remains large effectively arresting the dynamical response.

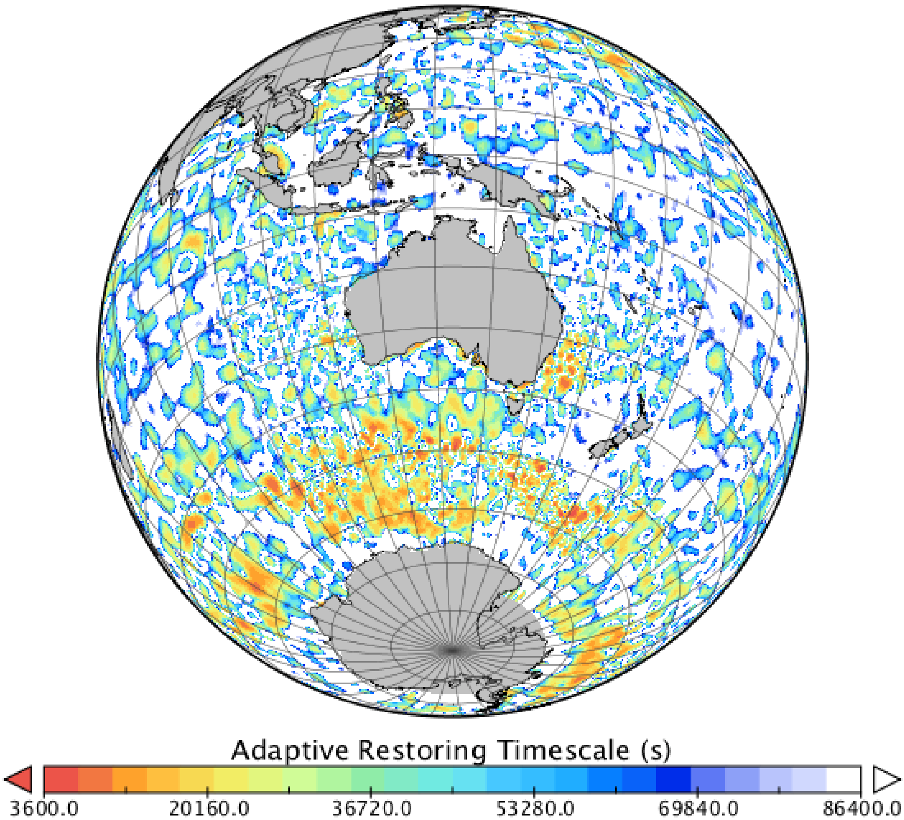

Fig. 25. An example of mean adaptive restoring timescale for the 24 h initialisation period

The favourable features of the scheme include numerical stability, a scaled relaxation timescale and minimisation of the model-target difference and shock.

In assessing suitable settings for the forecast system we looked at the amount of shock introduced into the forecast, the closeness of fit to the analysis and also compared the initialisation results against co-located BODAS super observations of sea surface temperature and sea surface height anomaly. Statistical measures that use the up-scaled super-observations reduce representativeness error compared to downscaled observations and provide a fair indication of how close the initialisation fits the observations at forecast base date. We also analyse the fifth day of the forecast against observations for that day. In general, in what we have seen in our experiments, a closer overall fit to observations at initialisation time leads to a closer fit at forecast day 5. The range of initialising experiments carried out for OceanMAPS2 is summarised in Table 10.

Experiment	Comment	A(SLA)	A(U/V)	A(T/S)	Normalise	TAU_MIN (s)	SIGMA-KE (J)	SIGMA-PE (J)	SIGMA-SST-1 (K)	SIGMA-SST-5 (K)	SIGMA-ETA-1 (m)	SIGMA-ETA-5 (m)
110313034225	No Initialisation	0	0	0	T	0	17.18	15401.50	0.460	0.565	0.099	0.103
110312234829	Option 1	0.5	0.5	0.5	T	1200	11.43	12492.80	0.355	0.451	0.086	0.093
110313001727	Option 2	0.7	0.7	0.7	T	1200	12.12	13226.40	0.333	0.440	0.083	0.092
110314223845	Option 3	0.9	0.9	0.9	T	1200	14.33	13867.35	0.312	0.429	0.080	0.091
110313011513	Option 4	0.7	0.7	0.7	T	3600	11.99	12839.25	0.335	0.441	0.085	0.093
110313014448	Option 5	0.9	0.9	0.9	T	3600	13.7	13312.15	0.314	0.430	0.082	0.092
110313031419	Option 6	0.9	0.1	0.9	T	3600	12.13	13288.48	0.315	0.434	0.082	0.093

Table 10 Statistics for the different initialisation experiments for OMv2

The main options were combinations of the adaptive tuning parameter *A* and tau_min, which sets the maximum allowable forcing. Option 3 was chosen for the behind-real-time (BRT) analysis initialisation and Option 1 for the near-real-time (NRT), based on the idea that in the BRT a greater number of observations provide greater confidence in the analysis, which justifies slightly stronger forcing in the initialisation. Figure 26 illustrates the co-located model-observation differences of global SST and SSHA for the initialisation period and for forecast day 5.

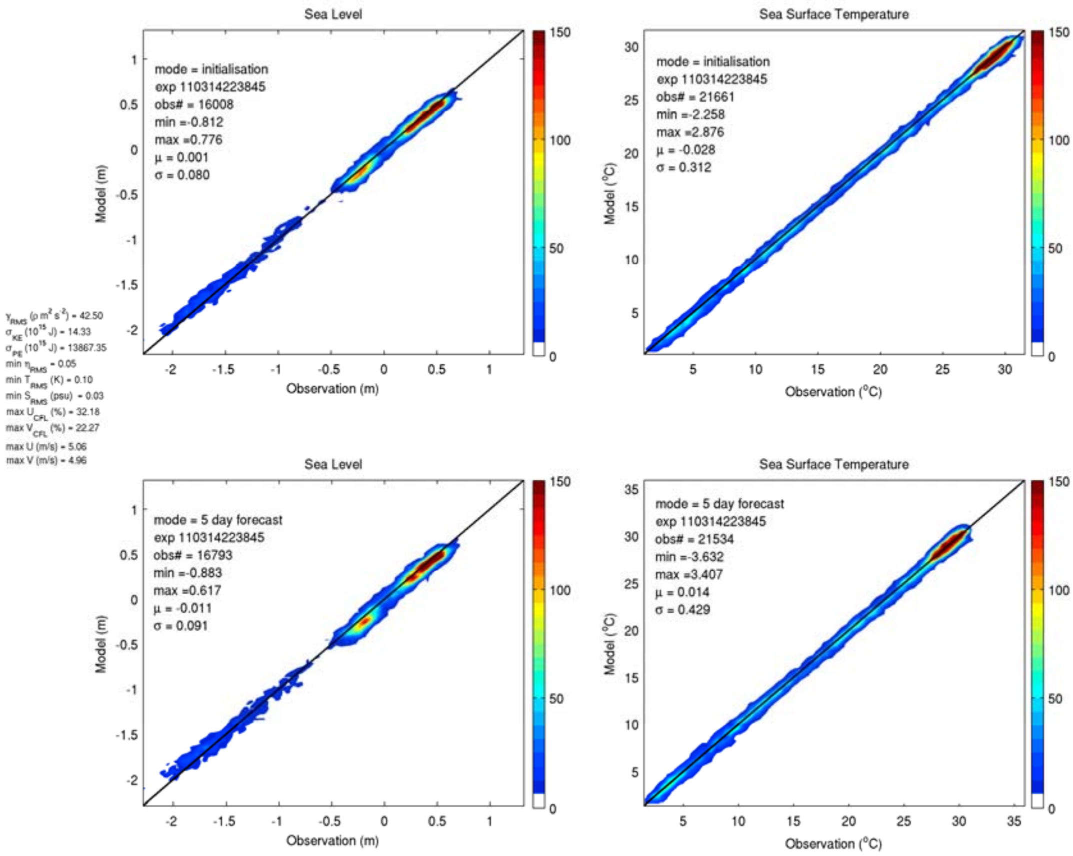

Fig. 26. Co-located model-observation differences for the initialisation period and the fifth day of the forecast for Option 3 (Refer to Table 1 for comparison of summary statistics with other experiments). Colour scale represents number of binned observations in the 2D histogram.

3.6 SURFACE FORCING

3.6.1 Atmospheric fluxes

The Bureau's operational global atmospheric system is referred to as the Australian Community Climate Earth System Simulator - Global (ACCESS-G) Puri et al., (2010). The global system uses a 6hr analysis update cycle using the 4D-Var assimilation system and its final outer loop involves a 6hr forward integration of the dynamical model from which the integral of surface fluxes can be obtained. Two of the ACCESS-G cycles are used to perform 10 day forecasts at 0Z and 12Z with the nested ACCESS-R performed on the alternate analysis cycles, 6Z and 18Z.

Two types of flux products are constructed from the ACCESS-G system for OMv2. A 24hr hindcast product composed of eight, 3hr averages with two obtained from each 6hr hindcast cycle performed in a 24hr period. The second product is based on the 0Z ACCESS-G forecast with eight 3hr averages for each 24hr period. Each product is then pre-processed for use by the ocean model integration.

The present strategy has not changed from OMv1, which is to apply the surface flux products as determined by the atmospheric hindcasts and forecasts. These flux products make use of surface boundary conditions that are independent from the surface conditions of the ocean model. There are several more sophisticated strategies that could be considered: (a) re-compute fluxes using a bulk formulae (e.g., Large et al., 1997) based on the atmospheric fields and replacement of OceanMAPS boundary conditions; (b) semi-coupled atmosphere-ocean where the boundary conditions of each system are used on alternate cycles; and (c) coupling of the atmosphere and ocean models. Both strategies (b) and (c) offer a more optimal response from the atmosphere to the ocean model state, particularly in the forecast cycle where present NWP strategies involve persistence of a nowcast SST. A regional coupled modelling system (Sandery et al., 2010a) has been developed and is being used to explore the impact of the coupling strategies on ocean prediction including the use of more complete earth systems e.g., a coupled wave model. One of the key metrics required to derive benefit to ocean prediction from coupling is the ocean model forecast skill for SST. The results presented below demonstrate a 30% improvement in performance as well as an improvement in reliability making such strategies viable. Adoption of the same strategy for NWP is not yet viable. Specific extension to OceanMAPS would be to extend the system globally and to introduce a strategy for the use of SST data assimilation between -5 days and real-time.

3.6.2 Pre-processing and regridding

The boundary conditions for surface roughness, surface albedo, surface temperature and surface moisture across the land-sea boundary can produce flux discontinuities across the land-sea interface. The continuity of the atmospheric fluxes across the land-sea boundaries was examined during the development of OceanMAPSv1 for GASP (Seaman et al., 1995). A zonal section taken through the Australian region at 25S (see Fig. 57) is used to highlight continuity across the land-sea boundary for each surface flux component for the four 6 hourly average for the 12 February 2006. The net downward shortwave radiation shown in Fig. 58, is approximately continuous across the land/sea boundary throughout the 24hrs. The nearshore values are continuous and exhibit weak gradients and sufficiently smooth to be interpolated directly. The net longwave radiation shown in Fig. 59, does exhibit gradients across the land/sea interface however, these do not exceed variability present over the ocean. Longwave flux values over the land mask are ignored. The longwave field over the ocean demonstrates discontinuities that would be best interpolated with shape preserving techniques or splines. The sensible heat flux shown in Fig. 60, exhibits significant discontinuities across the coastline during the local daylight hours. Approximately continuous during the local night-time hours. The latent heat flux shown in Fig. 61 is also discontinuous and more variable over land during daylight hours. Some weaker discontinuities remain during the night-time hours. The zonal stress is approximately orthogonal to the land/sea coastline for this section and demonstrates an example of a significant discontinuity on the east coast during the day. Approximately continuous during the night. Meridional stress, which is tangential to the coastline for this section demonstrates weaker discontinuities. Total precipitation is discontinuous over land or sea during night or day although the discontinuities are comparable to the variability over land or sea points. Total precipitation is regridded using linear interpolation.

Assuming that there is skill in the forecast fluxes a further consideration is how to minimise further losses of skill through the regridding of the fields to the ocean model. Regridding between two models introduces a number of sources of error: (1) unique distributions of high/low resolution, (2) unique definitions of land masks and (3) interpolation methods. Regridding of atmospheric model fields to force the ocean is performed so frequently that it has given rise to a number of strategies and software packages to perform the task. Regridding is a critical task built into the earth modelling frameworks such as OASIS (Valcke, et al., 2004), CCSM and FMS. All of these systems have been purpose built for coupled climate model applications and the strategies for regridding reflect that application. For example care is taken to ensure that the flux exchanged between the land-sea boundary and the atmosphere is conserved. This is ideal for a system performed in a coupled mode, however, the current version of OceanMAPS applies one-way forcing from prescribed fluxes. ACCESS-G provides relatively coarse grid information with a ratio of 0.375/0.1. Such coarse downscaling introduces a number of problems: (a) de-aliasing, (b) extrapolation for mismatch of the land-sea masks. Brassington (2011; section 18.6) outlines a conservative regridding strategy to address both of these properties. The present regridding algorithm for the operational system is however based on the less sophisticated but robust bi-linear interpolation.

3.6.3 River discharge

A portion of precipitation falling on land eventually enters the ocean via river outflows or discharge. River runoff is typically low volume, particularly in Australia, but is dynamically significant at the shelf scale. A skilful forecast of such fine scale processes is hindered by the lack of quality observation. More recently climate models have included river discharge in order close the mass budget where there is a net evaporative loss over the ocean surface. For a free-surface OGCM the loss of mass over long period integrations can result in a mean free-surface below the geopotential. The freshwater flux can also reduce the biases in the thermo-haline circulation.

MOM4p1 includes a river runoff module that can represent rivers as localised unidirectional fresh water fluxes. Specifically, rivers are represented as an additional source term to tracer concentration equations (pp 167-171: Griffies et al., 2010). Options exist within the module regarding the physical properties of the flux water, how the flux is distributed vertically and additional parameterised mixing. Table 11 summarises the river runoff module settings implemented in OMv1 and OMv2:

Table 11 MOM4p1 river runoff module parameter settings implemented in OFAM1/OMv1 and OFAM2/OMv2

<table>
<tr><td>OFAM1/OMv1</td><td>None</td></tr>
<tr><td rowspan="3">OFAM2/OMv2</td><td>Inflowing tracer properties homogeneous through river column.
• Potential temperature (theta) of river water = in situ surface ocean theta
• Salinity of river water = 0</td></tr>
<tr><td>River tracers inserted into the top 3 cells
• river_insertion_thickness = 15m</td></tr>
<tr><td>No vertical diffusivity enhancement.
• river_diffusion_thickness = 0m
• river_diffusivity = 0.0
• river_diffuse_temp = False
• river_diffuse_salt = False</td></tr>
</table>

The OMv1 did not include any explicit representation of river runoff. The OMv2 implements river fluxes from a global gridded climatology. Inclusion of the large fluxes attributed to the world's major rivers (e.g., Amazon River) is considered to be a positive step towards greater realism. The use of climatological values however has the disadvantage of not representing the temporarily intermittent nature of real river runoff; especially prominent in the Australian context. With this implementation all runoff locations have a fixed annual pattern of variation and no account of inter-annual variations is possible. The sources and implementation procedure is summarised in Table 12.

Table 12 The source and implementation procedure for climatological river runoff

<table>
<tr><td>Primary source</td><td>Global climatology by Dai and Trenberth, (2002).
• Download source: http://www.cgd.ucar.edu/cas/catalog/surface/dai-runoff/index.html
• Download file: 'runoff-2d-921River-1deg-mon.bin.gz' monthly discharge on 1x1 grid for 921 R case</td></tr>
<tr><td>Modifications</td><td>Regridding:
• projection from 1x1deg source grid onto OFAM2 surface grid
Regional modifications:
• Placement of Mekong on correct side of peninsular.
• Murray River outflow reduced.</td></tr>
</table>

Real-time and forecast river runoff would be preferred; however, such information is not yet available. It is noteworthy that during the development of OMv2 the section of the Bureau of Meteorology with expertise and responsibility for river flows and flood forecasting has undergone major organisational changes - namely the creation of the Water Division from various hydrology bodies. These changes are promising with regard to access to quality national-scope river information in the future.

The global distribution of applied river runoff is illustrated in Fig. 27 with an equivalent plot for the Australian region shown in Fig. 28. The following points highlight salient features of the runoff representation:

- The applied river runoff climatology represents a mean annual inflow of fresh water into the global ocean of ~1.12Sv, of which ~1.5% is allocated to the Australia region.
- Nearly all coastal cells have been given a non-zero value. Individual rivers are not well resolved and the flux is somewhat ‘smeared’ along coastlines.
- Dai and Trenberth [2002] describe the possibility that their data may have an incorrect distribution of runoff from continents but still achieving a reasonable total flux into each ocean basin.[Dai and Trenberth 2002: pp 676]

No runoff for Antarctica.

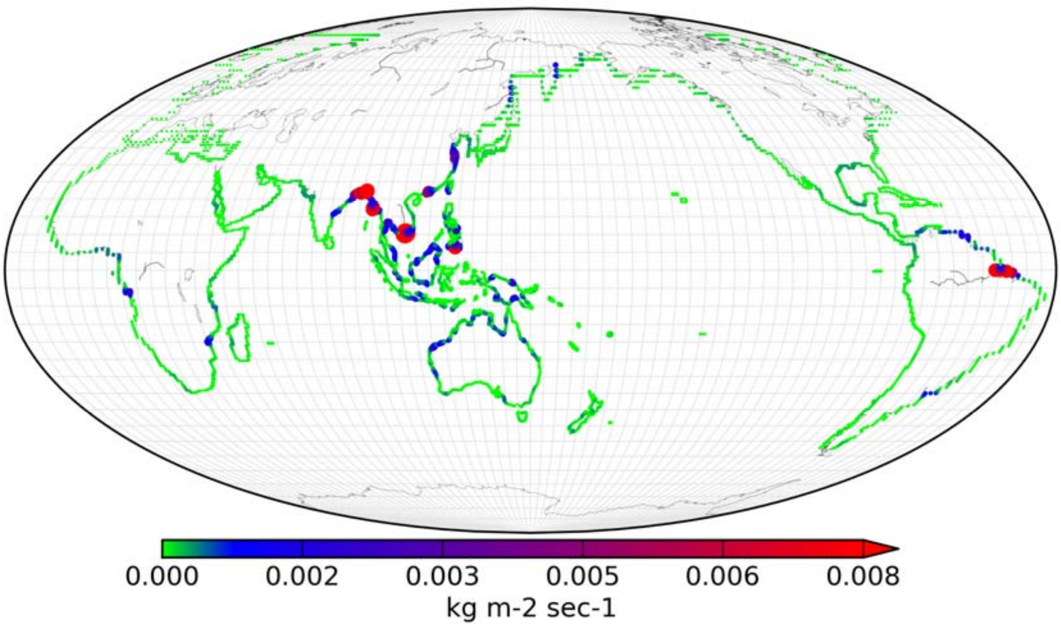

Fig. 27. Magnitude of the annual maximum mass fluxes applied along the modelled coastline. The scale of circle is also proportional to the mass flux.

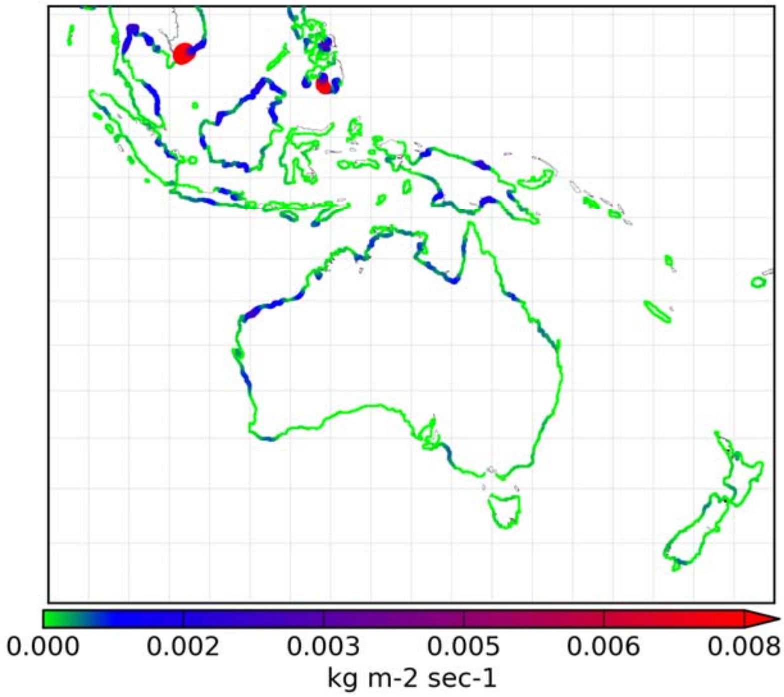

Fig. 28. Same as Fig. 27 but focused on the high resolution portion of the OFAM2 domain.

3.7 FORECAST SYSTEM DESIGN

The OMv1 forecast cycle was performed twice per week (Monday and Thursday). Each forecast cycle was composed, sequentially, of a behind-real-time (BRT) cycle, a near real-time (NRT) cycle and a forecast cycle. The BRT cycle performed an analysis 9 (or 8) days behind real-time based on the background from the 3 (or 4) day hindcast from the previous BRT cycle. Only the BRT cycle has a dependence on the previous cycle. This analysis permits a symmetric temporal coverage of altimetry when taking account of the 3 day latency of the IGDR data products and the 9.9 day orbit periods of the Jason-series satellites (see section 3.1.1). This constraint is imposed by the use of a 3D data assimilation system where all observations are effectively assumed to have been observed at the analysis time. To control the temporal decorrelation of past or future observations an age penalty is added to the observation error (Oke et al., 2008). The use of a symmetric time window provides the maximum correlated information to the target analysis time and thereby provides the optimum centred in time analysis of sea surface height anomaly. Some of these limitations can be partially overcome by the implementation of a FGAT scheme and a corresponding objective or flow dependent time decorrelated error penalty. FGAT has not been implemented into the version 2 system.

The NRT cycle for OMv1, is composed of a 5 days behind real-time analysis based on the 4 (or 3) day hindcast background from the BRT cycle. This analysis uses an asymmetric observation window of -7 days and +2 days for satellite altimetry. The SST observations are the same as the next BRT analysis excepting recovery of observation gaps from real-time communications or other operational faults. The in situ observations continue to be updated daily for near real-time QC data from the GDAC's as described in section 3.2 and will change for the next BRT cycle. The NRT analysis is initialized and hindcast for 5 days to real-time. Both the BRT and NRT cycles make use of hindcast fluxes as described in section 3.6.1. No additional constraint is given to the model state during these 5 days. A seven day model forecast was then integrated.

The OMv2 has been constructed to provide a daily forecast. However, the same constraints of altimetry coverage are expected to apply throughout the lifetime of the forecast system. Therefore the BRT/NRT/forecast cycle design is preserved but with a subtle design modification that permits greater independence between cycles. The BRT cycle is constructed to be a uniform 9 days behind real-time with a uniform 4 day hindcast. The BRT again is the only part of the system that is dependent on the previous forecast cycle. A single BRT cycle provides an analysis every four days as shown in Fig. 29a and is denoted as cycle 00. From each hindcast a NRT analysis and 5 day hindcast is performed followed by a 7 day forecast as in OMv1. An independent cycle 01 is then introduced that provides the forecast cycle on each day after cycle 00 as shown in Fig. 29b. The remaining days are completed by two further independent cycles denoted 02 and 03 as shown in Fig. 29c.

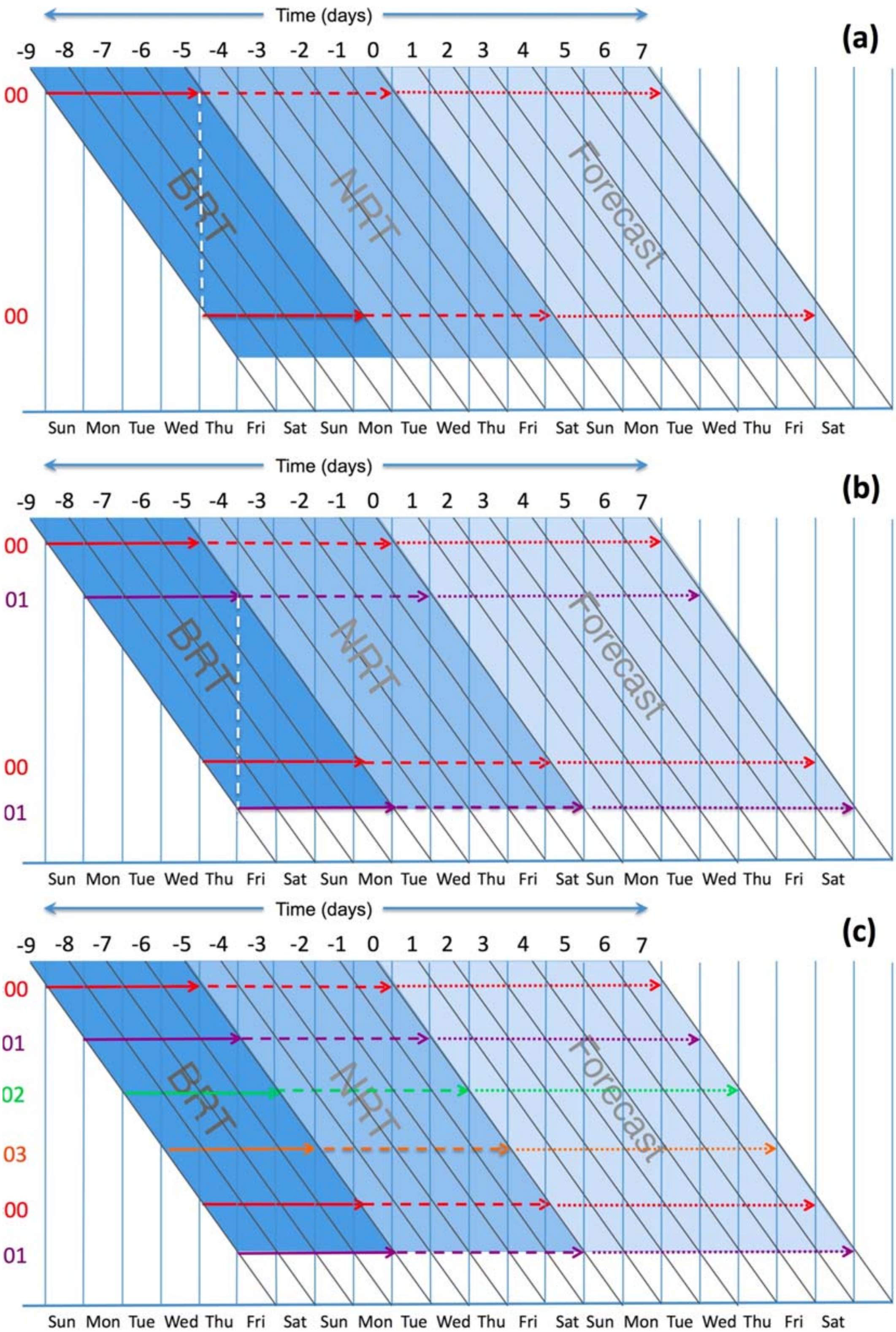

Fig. 29. Schematic of forecast cycle composed of behind real-time, near real-time and forecast cycles. There are four independent cycles labelled (00, 01, 02 and 03) that are performed sequentially over four consecutive days with a four day repeat cycle. (a) cycle 00, (b) cycle pattern for 01 and (c) full cycle pattern

Each of the BRT cycles shares altimetry and in situ profile observations through the overlapping observation windows although the error assigned to each observation is unique due to the age penalty. The BRT hindcasts also share common atmospheric fluxes. The analyses also share a common stationary ensemble. Otherwise the forecast cycles do not share background information. The resultant design therefore provides a four member time-lagged ensemble, a so-called poor man's ensemble. However, this multi-cycle, non-sequential, schedule was designed to create greater independence and greater spread compared with other studies based on sequential time-lagged ensembles (e.g., Brankovic, et al., 1990 and Hoffman and Kalnay, 1983). It should however be noted that the operational trials were initially dependent as the four cycles were bootstrapped from the OMv1 BRT hindcasts.

3.8 COMPUTATIONAL DESIGN

BODAS2 assimilates observations to produce an analysis of sea surface height, temperature, salinity and the horizontal components of currents on the OFAM2 grid. The forecast error covariance estimates are derived from a stationary 144 member ensemble of model anomalies. The global model domain is decomposed into 44 sub-domains. For computational efficiency, each sub-domain applies an adaptive decomposition algorithm using an observation vector length of 3000. The parallel solution of the analysis equations employs a Jacobi preconditioned bi-conjugate gradient stabilized method (Balay et al., 2010). Runtimes to complete all 44 subdomains (8 cores per domain) average 24.13 minutes for the analysis cycle and 22.42 minutes for the near real time cycle.

The OFAM2 grid is decomposed over 144 cores comprising 8 longitudinal and 18 latitudinal slices. The analysis and near real time cycles include 1 day of adaptive initialisation (Sandery et al., 2010b) in the 5 day run. With this model setup, the behind real time and near real time analysis cycles have an average runtime of 5.85 minutes per model day. For the forecast cycle, which does not have an initialisation period, the average runtime per model day is 5.24 minutes.

These metrics are for the two most computationally expensive processes in the OMv2 daily cycle. Combining the average runtimes for each component over each of the OMv2 steps in Fig. 29, a complete daily run takes around 2.36 hours.

The performance was measured using the Bureau of Meteorology SUN Constellation, which consists of 576 nodes, each with 2 quad-core Intel 64-bit Xeon processors (code named Nehalem), totaling 4608 CPU cores. Each node has 24 Gbytes of main memory and 24 Gbytes of flash memory instead of local disc. All of the nodes are connected by a dual-rail Infiniband network, with data rates of 40 Gbit/s per connection.

4. RESULTS

4.1 BIAS

A common problem for ocean models is so-called, "model bias", the persistent error from the true ocean state. There are many sources for model bias e.g., bathymetry errors from the source product or the gridded representation, biases in the applied surface fluxes, incomplete physics such as tides, inaccurate physical parameterisations and sub-grid scale closure. In a model simulation, the bias can be diagnosed and corrected posterior to the model integration. In a forecast system, these biases can be reflected as persistent contributions to the forecast innovations and are present in the analysis increments. One strategy to alleviate this problem is to implement a bias correction scheme as part of the analysis cycle, Dee (2005) whereby the bias plays a diminishing role. Based on the results presented below such an approach could be applied to OceanMAPS however, this remains under research and development and was not included in OMv2.

The time mean of the increment fields provides a metric for the persistent corrections being applied to the forecast system through the analyses and initialisation cycle. This bias will combine systematic errors in the observations, data assimilation and modelling system of which model bias (see section 3.3.2) appears to dominate. Figure 30 shows the mean increment for sea surface height anomaly from both the OMv1 and OMv2 over the three month trial period. We note that the sample size for OMv1 is smaller and will lead to larger estimates of the bias; however, the gross features and relative magnitude are comparable with longer period averaging (not shown). These diagnostics offer limited direct insight into the source of the model bias but capture the locations for bias and thereby we can infer potential processes that might be involved as well as the differences between the two systems. The period of averaging used in this case is that of the Austral summer which corresponds to a peak in the East Australian Current (EAC), but a decline in the Leeuwin Current (LC). A 3.5 month period is relatively short and sub-samples some of the eddy-variability so the interpretation is less suited to a detailed analysis but should capture the gross features. Figure 30a shows the analysis exhibits a large bias in the Southern Ocean, which was previously attributed to the representation of bathymetry. Figure 30b shows that the Southern Ocean remains dominant although the bias has changed structurally. It is evident in Fig. 30 that the mean increment field contains a mixture of broad scale and fine scale biases. We introduce a spatial filter to separate these signals.

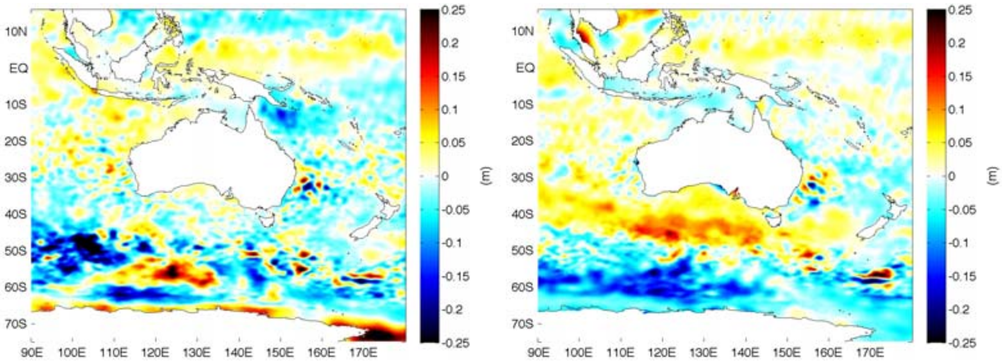

Fig. 30. Mean analysis increment of sea surface height anomaly for the period 20101201 - 20110323 (a) OMv1 and (b) OMv2

We apply a two-dimensional Hanning filter as described earlier in section 3.3.2 with an e-folding scale of 1° and applied over a region of +/- 5° with an adjustment of the area averaging for land points. This is done in a simplistic way i.e., semi-enclosed seas are not excluded from the open ocean average. The filtered and residual field for each mean increment shown in Fig. 30 is shown in Fig. 31. The broad scale bias for OMv2, Fig. 31b, is lower in magnitude compared with OMv1, Fig. 31a. Specific improvements can be seen in the Coral Sea and tropics more generally and the mid-latitudes are approximately unchanged. The largest change occurs in the Great Australian Bight region, which has introduced a broad zonal bias. Similarly south of the subtropical front there is a large negative bias of comparable magnitude. These biases correspond closely to the differences in the mean dynamic topography shown in Fig. 17. A detailed analysis has not been undertaken however, as noted earlier in addition to model differences the atmospheric forcing applied was also changed from ERA-40 for the OFAM1 SPINUP to ERA-interim for the OFAM2 SPINUP. The same atmospheric forcing, ACCESS-G, was applied to OMv1 and OMv2 during the trial period therefore the differences in mean increments cannot be attributed to this forcing.

OMv1 shows fine scale biases in the high-latitudes, Fig. 31c, which were attributed to inaccuracies in the representation of bathymetry which affected the Antarctic Circumpolar Current (ACC), which is known to interact and be steered by bathymetric features. The introduction of the updated bathymetry has improved the fine scale bias in all locations except south of the Chatham Rise. Persistent baroclinic adjustment remains present for the EAC although both the magnitude and region of bias is reduced. There is also a larger bias along the coast of Thailand, which is attributable to the new ocean cells from the shallower minimum column depth. The mean analysis increments for the new system can be interpreted as an observed broad barotropic mass distribution that is not balanced by the atmospheric winds resulting in a persistent correction.

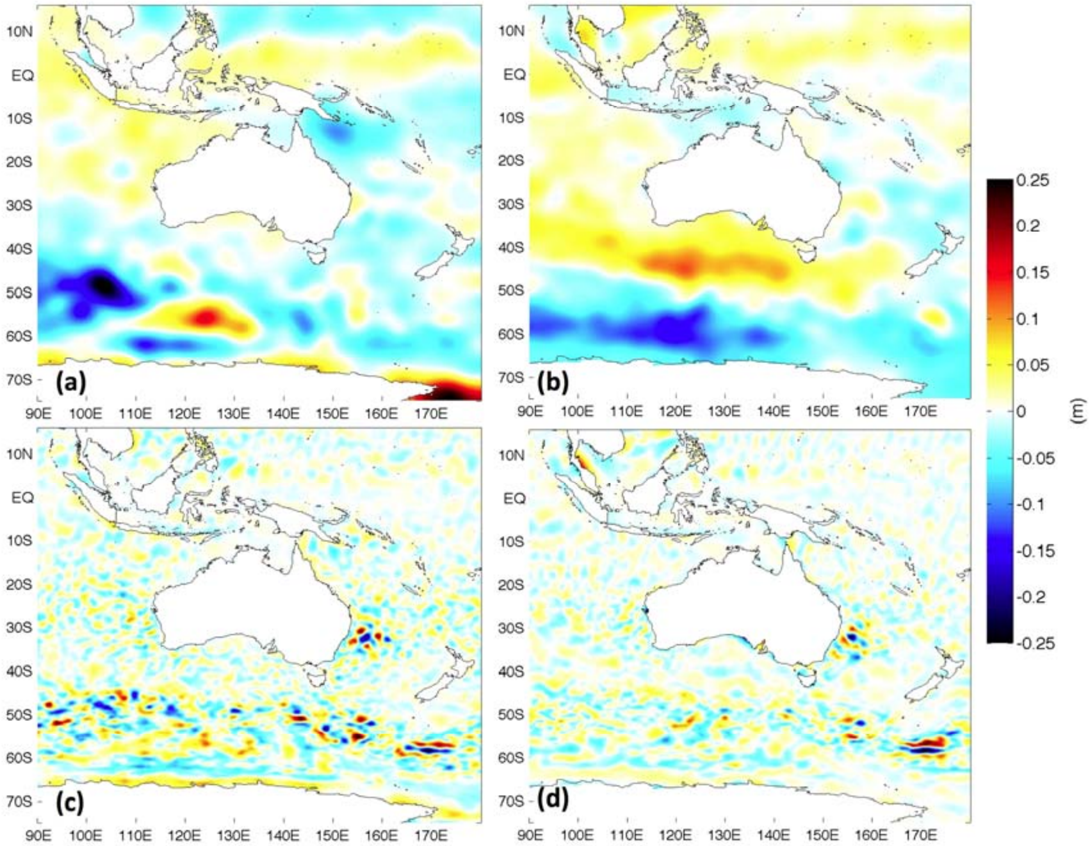

Fig. 31. Hanning filtered mean analysis increment for the period 20101201 - 20110320 (a) OMv1 and (b) OMv2 and the residual (c) OMv1 and (d) OMv2.

The impact of the increment bias on the model hindcast can be estimated by taking the mean difference of the initialised model with the background model field as shown in Fig. 32a. Applying the same Hanning filter to Fig. 32a separates the broad and fine scales as shown in Fig. 32b and c respectively. The mean initialised field is clearly correlated to that in Fig. 31b and d however, with a significantly reduced magnitude. The fine scale bias, Fig. 32c is also correlated to the fine scales of the mean increment however, of a reduced magnitude. In both cases the model, forcing and initialisation reject the increment field. We hypothesise that the majority of the increment relates to barotropic forcing which radiates as gravity waves over each initialisation period.

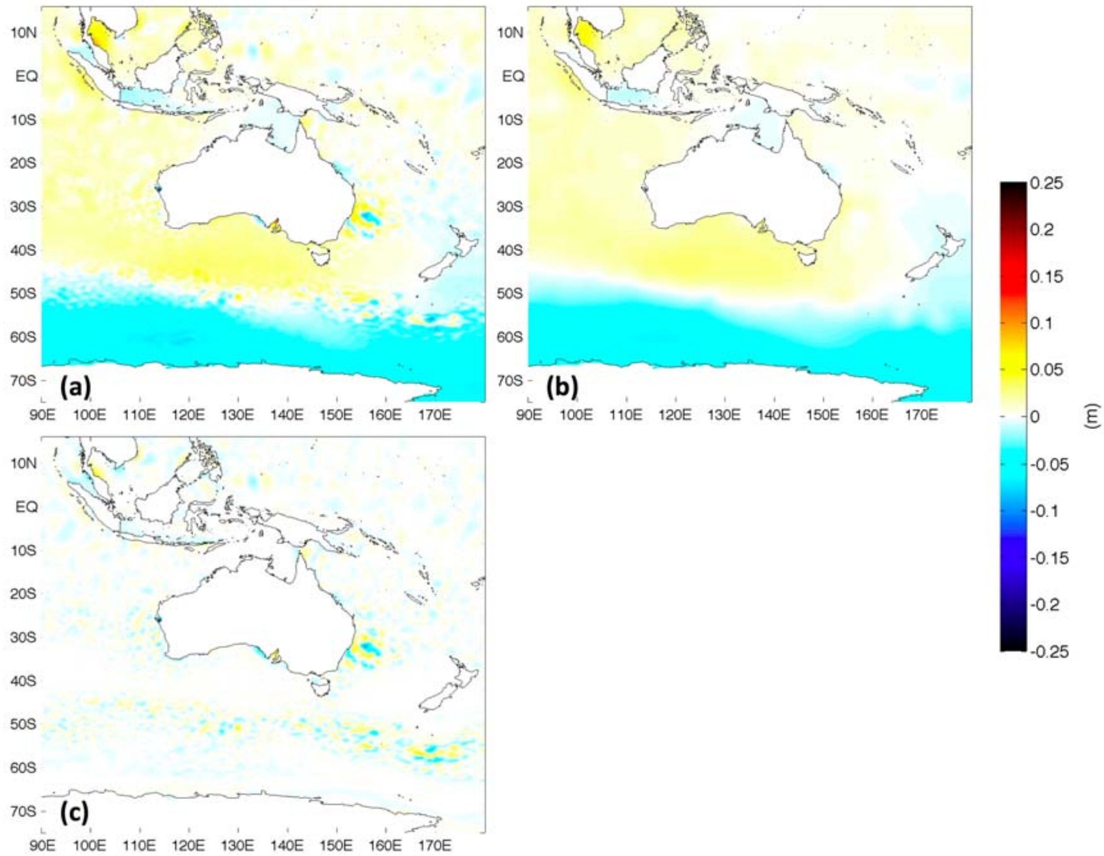

Fig. 32. (a) Mean hindcast increment after initialisation of OMv2 over the period 20101201 - 20010320, (b) the Hanning filtered mean hindcast increment and (c) the residual from the Hanning filter. The anomalies are presented using the same colorbar as Fig. 31.

Applying the same Hanning filter analysis described above we obtain the mean increments for SST and SSS as shown in Fig. 33. Figure 33a and c are largely uncorrelated from each other and from the broad scale pattern of SSHA, Fig. 31b. The SST pattern shows distinct bands that may relate to a bias in the representation of the seasonal cycle through heat fluxes that lags the observed warming in mid-latitudes during Austral-summer. The cool bias below the subantarctic front may relate to biases from the absence of sea ice processes or the atmospheric fluxes in this region. Figure 33b shows comparable fine scale residuals south of Chatham Rise and the southern Tasman Sea. The EAC shows a larger area of SST residuals compared with SSHA. There are higher magnitude residuals south of Cape Leeuwin and along the ACC which may be a result of sampling error and not long period biases. Figure 33d shows no significant fine scale residuals along the ACC or EAC separation region but comparable fine scale residuals south of Cape Leeuwin. Figure 33d also shows significant residual biases in the tropical ocean particularly in the western Pacific and South China Sea. There is also a notable persistent anomaly from a mooring in the TAO/TRITON array.

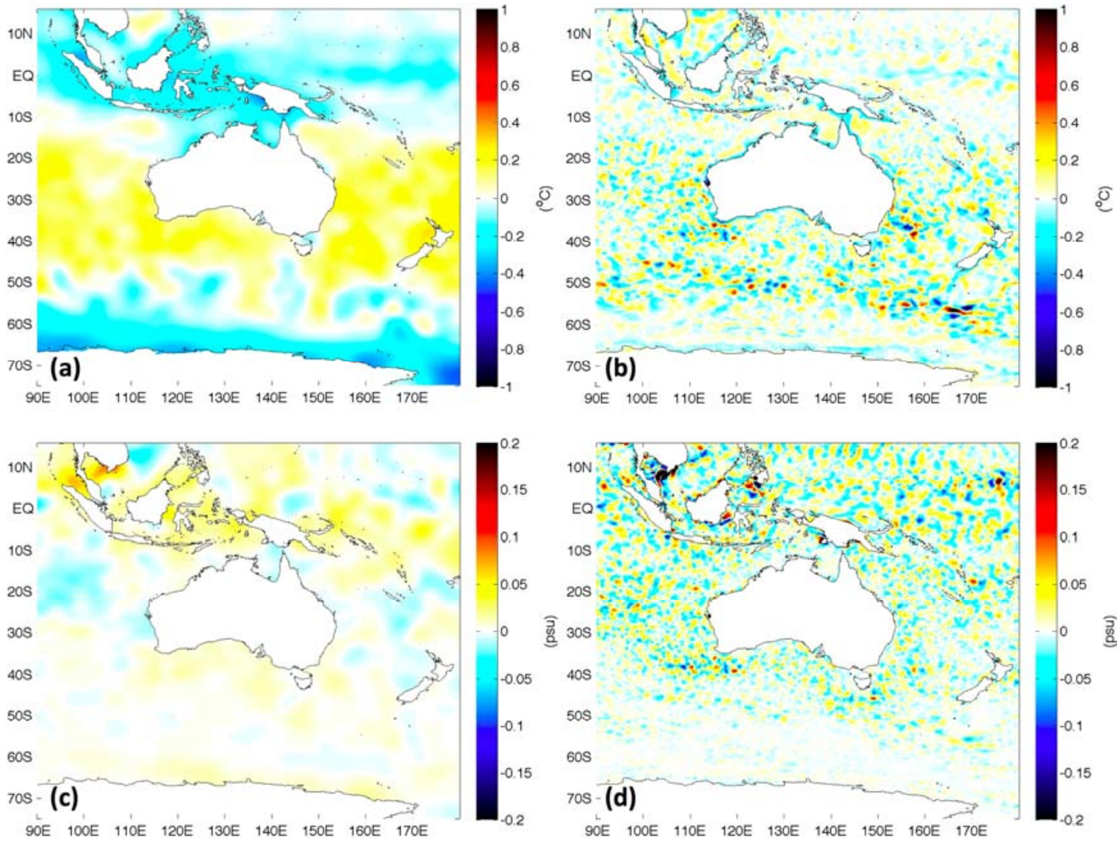

Fig. 33. Hanning filtered and residual for the mean analysis increment of sea surface temperature and sea surface salinity for the period 20101202 - 20110320 for OMv2. (a) SST filtered, (b) SST residual, (c) SSS filtered and (d) SSS residual.

4.2 OBSERVATION STATISTICS

The operational trial was performed using the same real-time observations available to the operational OMv1. The super-observations assimilated therefore varied throughout the trial period as shown in Fig. 34. Super-observations of satellite altimetry, Fig. 34a, shows one instance of a sustained decline of approximately 12% in January and a transient loss of a similar magnitude in February. Super-observations of satellite SST, Fig. 34b, show more consistent data volume throughout the trial period with a variation of up to 6% but no transient spikes. The relationship between these time series and the performance of the trial is examined in section 4.5.

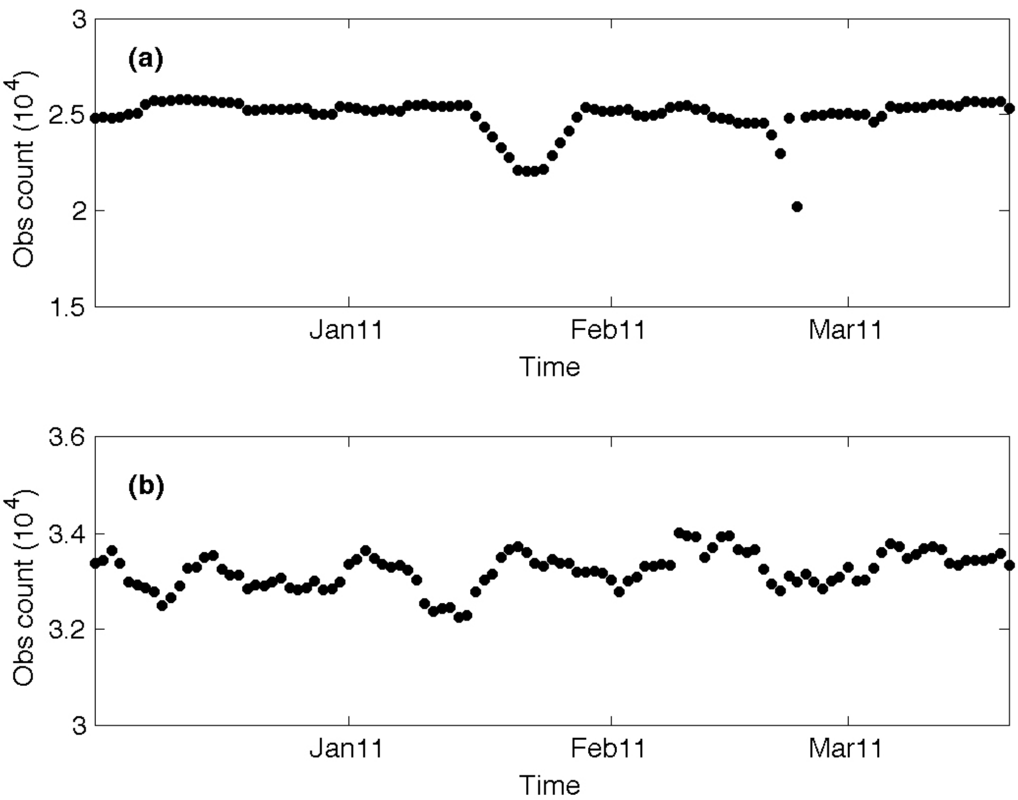

Fig. 34. The total number of super-observations assimilated in each BRT analysis from all four cycles represented as a time series (a) SSHA and (b) SST.

The forecast and analysis innovations provide a distribution from which we examine the statistical outliers. The set of all innovations from all of the BRT analyses throughout the trial are treated as a single population. The expected errors will scale with the ocean variability therefore we normalise the innovations by the variability estimated by the model. Outliers for the normalised forecast innovations indicate locations that have relatively large forecast error. Outliers for the normalised analysis innovations indicate observations that the analysis was unable to fit indicating that the observations contain information that is not represented by the scales of the model and ensemble statistics or has a large observation error. Outliers for both the forecast and analysis indicate that it is both difficult to forecast and unrepresentative. We define a statistical outliers as exceeding the 99.95 percentile. The location of the outliers for super-observations of SSHA are plotted in Fig. 35 with a unique colour for each type with those common in green. The distribution of outliers indicates that the EAC separation and Tasman Front region provides the most outliers common to both. The same location shows many forecast innovations indicating the model may be biased in the penetration of the EAC and related eddy dynamics compared with observations. The smaller number that are common indicate that either the errors are too large to fit in a single analysis or there is a bias in the ensemble statistics. Another concentration of point lies in the Indonesian region. In this case there are more outliers of the analysis innovations with a smaller number that are both. This indicates that some of the observations include processes that are not represented by the model or analysis statistics. Many of these observations are located close to the coast which can lead to lower quality observations. The criterion for removing coastal observations based on the 200 m isobath may be inadequate in this region as the continental shelf can be very narrow. A criterion based on distance from the nearest landmass may be worthwhile. A similar pattern can be seen with some of the observations in the South Pacific. There is an indication that outliers can also occur in the southeast Indian Ocean however, this appears to be infrequent.

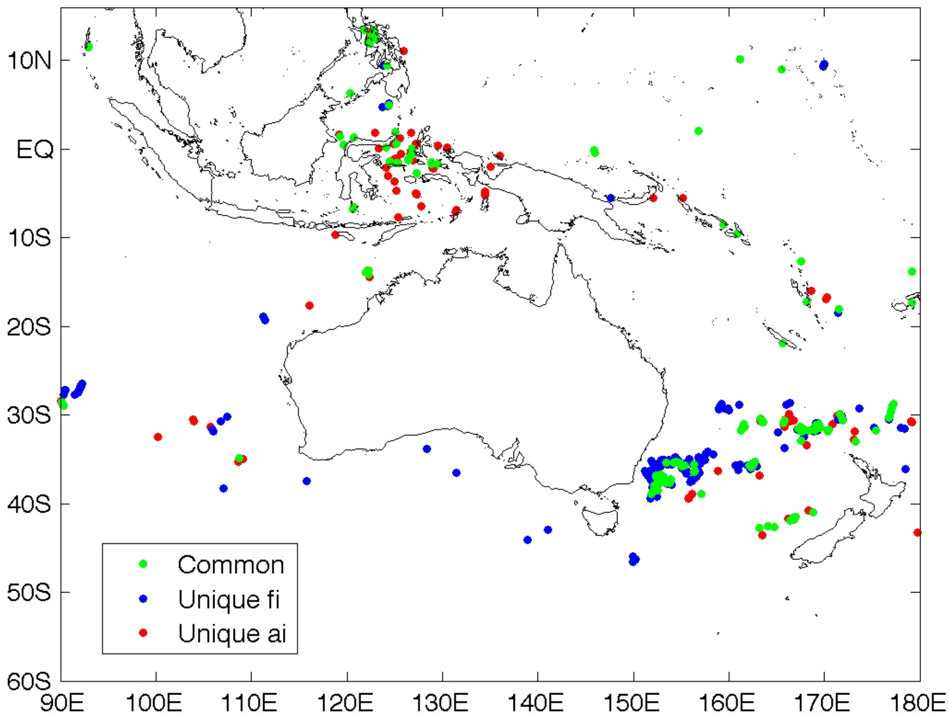

Fig. 35. SSHA super-observation outliers determined by the 99.95 percentile of analysis innovations (ai) and forecast innovations (fi) from the BODAS analysis normalised by the model variability for the period Dec 2010 - Mar 2011. Common outliers (green), unique fi outliers (blue) and unique ai outliers (red).

The same analysis applied to the super-observations of SST shown in Fig. 36 results in more outliers as the number of super-observations is larger and the locations potentially more variable. There is a large concentration of common outliers near the coast, which are obtained from AVHRR. This indicates these observations contain additional variability that cannot be represented by the model. Potentially the representative error near the coast is under-estimated. A concentrated set of common points lies almost zonal along 55S. This is not related to a transition in resolution or in super-observations but it is a location where there is a negative bias of the SSHA and might be related to the background error covariance. A second cluster of common points lies in the Pacific at ~10S, which is the location of the South Pacific Convergence Zone (SPCZ).

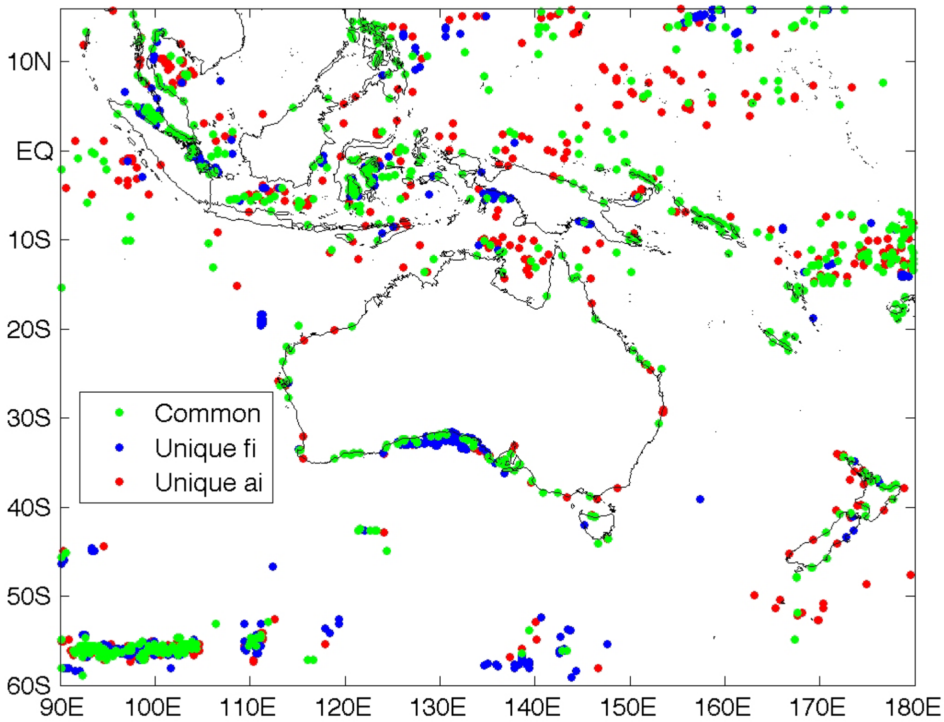

Fig. 36. SST super-observation outliers determined by the 99.95 percentile of analysis innovations (ai) and forecast innovations (fi) from the BODAS analysis normalised by the model variability for the period Dec 2010 - Mar 2011. Common outliers (green), unique fi outliers (blue) and unique ai outliers (red).

During the trial period, Austral-summer the SPCZ extends eastward increasing the amount of convection and precipitation. The number of AMSR-E observations during this period reduces to only 30-40 % as shown in Fig. 37 for the Austral-summer in 2006. However, the number of common outliers in Fig. 36 indicates that the algorithm for identifying rain contaminated points may need to be improved. Recent analyses comparing the new AMSR-E L2P product indicate that this reduces the number of "bad" data. The other regions in the tropics where the percentage of AMSR-E declines appears to correlate with the pattern of outliers in Fig. 36.

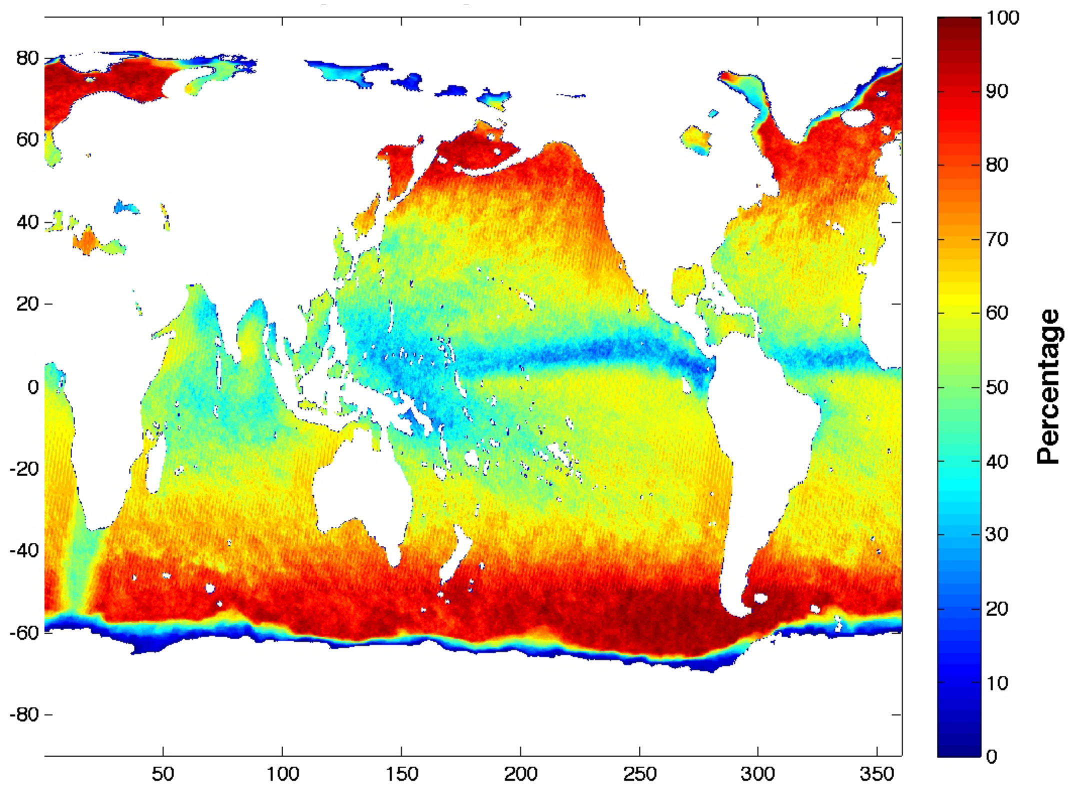

Fig. 37. The percentage of valid descending AMSR-E observations from the total number of passes during Austral-summer in 2006

4.3 ANALYSIS STATISTICS

The statistics from the BODAS2 analyses provides a convenient comparison of the performance of the two systems. The analysis cycle provides both a forecast innovation, $w^o - Hw^f$ based on the observations w^o minus the prior model forecast interpolated to the observation position, Hw^f and an analysis innovation $w^o - Hw^a$ where the analysis field is interpolated to the observation position, Hw^a. The observations, in this case, represent the quality controlled super-observations that are assimilated for each analysis. For the BRT cycle, observations are included from a time window centred on the analysis time. Different time windows are applied to each observation type (see Appendix B) and chosen to provide maximum spatial coverage from the most recent observations. The statistics derived below provide equal weighting to all observations. In principle older observations could be down weighted however, the specification of weights introduces unnecessary complexity for the purpose of the comparison here. As a result, the statistics presented are likely to under-estimate the system performance. The error is expected to scale with the distribution of ocean variability and could be normalised. However, due to unnecessary complexity introduced by the errors in the model estimate of variability the innovations are first presented unnormalized. As a result, the statistics will be biased by the performance in the regions with the largest variability as shown in **Error! Reference source not found.**.

In the case of OMv1 the behind real-time hindcast period alternates between 3 and 4 days while for the OMv2 uses a uniform 4 day hindcast. The statistics for OMv1 are therefore a mixture of errors; however, this should favour OMv1 as half the samples will have a 3-day hindcast period. The statistics for OMv1 is performed twice per week whilst for OMv2 we combine the four forecast cycles to provide a forecast innovation statistic for each day.

The root mean square error (RMSE) of the forecast innovation vector is thinned to only those observations that occur in the high resolution region, 90E-180E and 75S-16N. Performance outside this region is expected to be reduced and is not examined in detail. Figure 38 shows the RMSE forecast and analysis innovations for the super-observations of sea surface height anomaly for the BRT analyses from OMv1 and OMv2 for trial period of 2nd Dec 2010 to 20th Mar 2011.

The RMSE analysis innovations for OMv1 based on the OMv1 super-observations is consistently 1 cm lower than OMv2. This indicates that the OMv1 provides a closer fit to the SSHA observations. The statistics obtained from the analysis system are determined by the assumptions of the analysis system in particular the relative magnitude of the error covariance assigned to the observations and background. The performance is also related to the construction of the super-observations between the two systems. In OMv2, a higher resolution of super-observations is applied based on the improved computational performance. The performance of OMv1 is comparable to OMv2 when the same super-observations are used as shown later in Fig. 45. The RMSE forecast innovation for OMv1 ranges 1-2 cm higher than OMv2 over the trial period. Both the RMSE forecast innovation time series shown in Fig. 38 show significant variability, which will be investigated further for sensitivity to the super-observation coverage. The variability is summarised in Fig. 45 through the 99th percentiles.

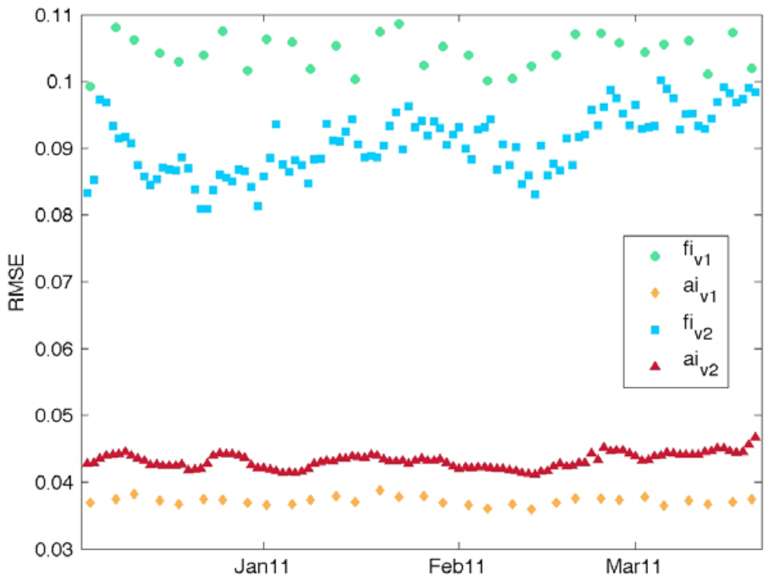

Fig. 38. RMSE sea surface height anomaly (m) for the analysis innovation and forecast innovation from the behind real-time analysis cycle for OMv1 (orange and green) and OMv2 (red and blue). The RMSE values represent the trial period Dec 2010 to Mar 2011.

The anomaly correlation represents a correlation of the super-observations with the background analysis $\mathrm{Ha} = \mathrm{o} - \mathrm{ai}$ or hindcast $\mathrm{Hf} = \mathrm{o} - \mathrm{fi}$. Figure 39 shows a comparable correlation for the analysis of ~0.91. The OMv2 hindcast correlation is initially ~0.15 higher than OMv1 but converges over the period of the trial to ~0.1. As noted for the RMSE, the hindcast anomaly correlations exhibit considerable variability whilst the analysis anomaly correlations are approximately constant.

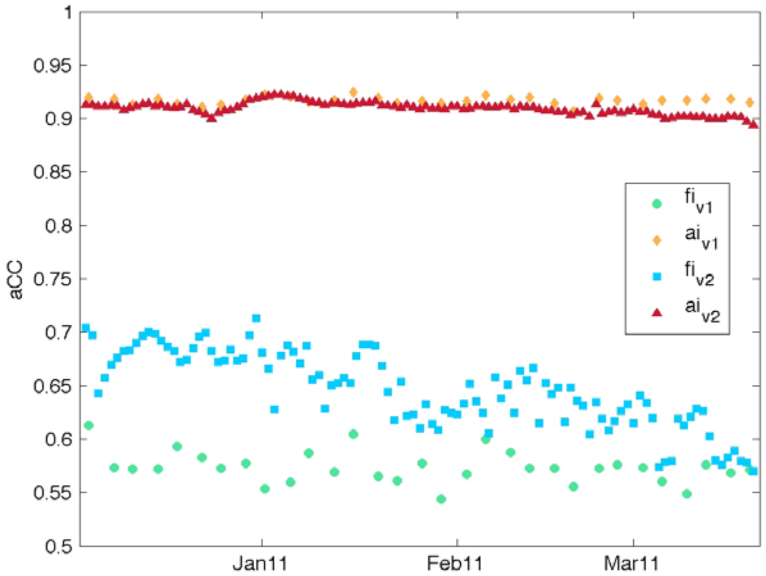

Fig. 39. Anomaly cross correlation sea surface height anomaly for the analysis innovation and forecast innovation from the behind real-time analysis cycle for OMv1 (orange and green) and OMv2 (red and blue). The aCC values represent the trial period Dec 2010 to Mar 2011.

All of the forecast innovations for SSHA during the trial period are normalised by the variability of the ocean model and used to construct a frequency distribution for OMv1 and OMv2 as shown in Fig. 40. OMv2 shows both a reduction in bias and a higher kurtosis indicating a reduction in the probability for large normalised forecast errors.

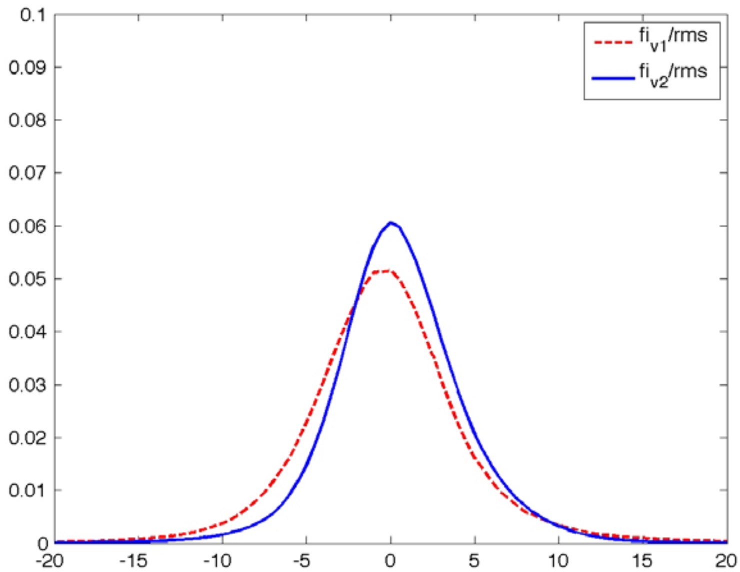

Fig. 40. Frequency distribution of the forecast innovations normalised by the variance of the OFAM1 or OFAM2 SPINUP respectively, from the four day hindcast of the behind real-time analysis cycle from OMv1 (red) and OMv2 (blue) for the period Dec 2010-Mar 2011.

The RMSE of the analysis innovations for SST, Fig. 41 are characterised by higher variability compared with the RMSE of SSHA analysis innovations, Fig. 38 particularly for

OMv2. The are two specific peaks in RMSE during the trial period that will be compared with the observation coverage in section 4.5. The performance of the OMv1 analysis innovation is consistently lower than OMv2; however, Fig. 48 shows the performance is comparable when compared to the OMv2 super-observations as was noted above for SSHA. The RMSE of OMv2 hindcast innovations are ~0.5 °C lower than OMv2. The variability in RMSE of the hindcast innovations for both OMv1 and OMv2 show a high correlation with the corresponding variability in RMSE for the analysis innovations. This indicates that the performance is largely determined by the initial error.

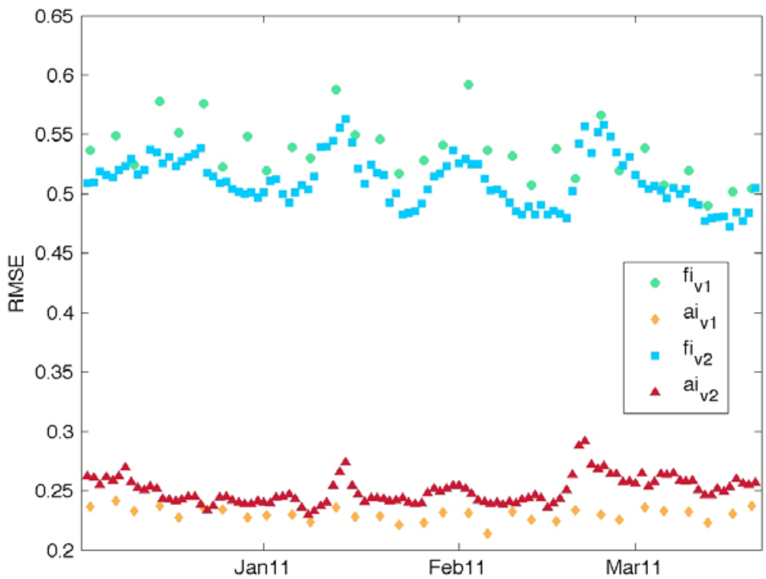

Fig. 41. RMSE SST for the analysis innovation and forecast innovation from the behind real-time analysis cycle for OMv1 (orange and green) and OMv2 (red and blue). The RMSE values represent the trials period Dec 2010 to Feb 2011.

The anomaly correlation for SST is constructed relative to the seasonal cycle i.e., corr(o-SST_{clim}, Hf-SST_{clim}) where corr represents a function for the correlation coefficient. The anomaly correlation for the analysis of OMv2 is lower that OMv1 throughout the trial with a range of 0.95-0.97 as shown in Fig. 42. The anomaly correlation of OMv2 also shows greater variability compared with OMv1. The anomaly correlations for the forecast innovations of OMv2 consistently exceed OMv1 throughout the trial period. The variability of the anomaly correlations is much greater with a range of 0.8-0.87 however, the time series appears to be lag-correlated with the analysis time series.

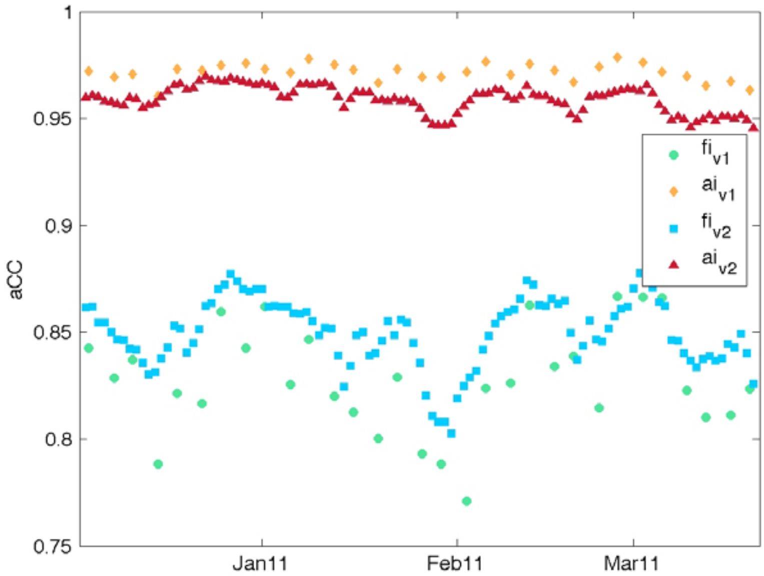

Fig. 42. Anomaly cross correlation sea surface temperature for the analysis innovation and forecast innovation from the behind real-time analysis cycle for OMv1 (orange and green) and OMv2 (red and blue). The aCC values represent the trial period Dec 2010 to Mar 2011.

All of the forecast innovations for SST during the trial period are normalised by the variability of the ocean model and used to construct a frequency distribution for OMv1 and OMv2 as shown in Fig. 43. Both OMv1 and OMv2 show a small bias however, OMv2 shows a higher kurtosis indicating a reduction in the probability for large forecast errors.

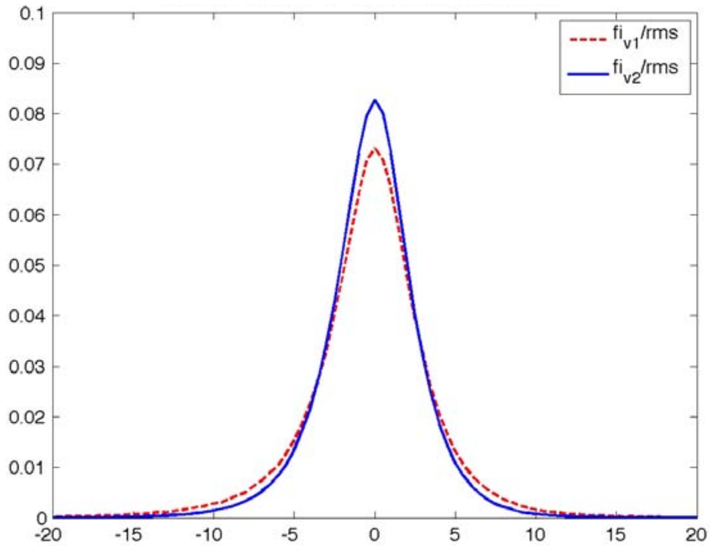

Fig. 43. Frequency distribution of the forecast innovations normalised by the variance of the OFAM1 and OFAM2 SPINUP respectively, from the four day hindcast of the behind real-time analysis cycle from OMv1 (red) and OMv2 (blue) for the period Dec 2010-Feb 2011.

4.4 FORECASTS STATISTICS

The daily cycle from OMv2 provides a BRT analysis and a set of super-observations for each day of the trial period (minus 9 days). This set of super-observations is used as the reference "truth" to quantify the errors of each day of the BRT, NRT and forecast cycles. Similar to section 4.3 each super-observation is applied with equal weighting. The results shown will overestimate the performance of the hindcasts where the super-observations are assimilated; however, this does provide a measure of the quality of the analysis and initialisation. As the NRT is performed 5 days behind real-time the super-observations are independent for the forecast cycle. The RMSE is calculated for all observations within the Australian region (90E-180E, 60S-16N). The RMSE for each analysis day of the trial period is shown in Fig. 44 where the BRT hindcasts (dark blue), NRT hindcast (blue) and forecast (light blue) shows a correlated time series with monotonically increasing error for each cycle. In all cases the first 24hrs BRT hindcast has a lower error than the equivalent NRT hindcast demonstrating the penalty of the missing altimetry observations. It is expected that in the absence of the BRT cycle the RMSE of the NRT cycle would be even higher. One of the four behind real-time analysis cycles (00, 01, 02 and 03) is performed each day. As expected, Fig. 44 shows that all four cycles provide comparable performance and can be combined into a single statistic. The successive cycles show consistent perturbations in performance indicating the perturbations (e.g., the observing system) impact multiple cycles through the overlapping observation windows.

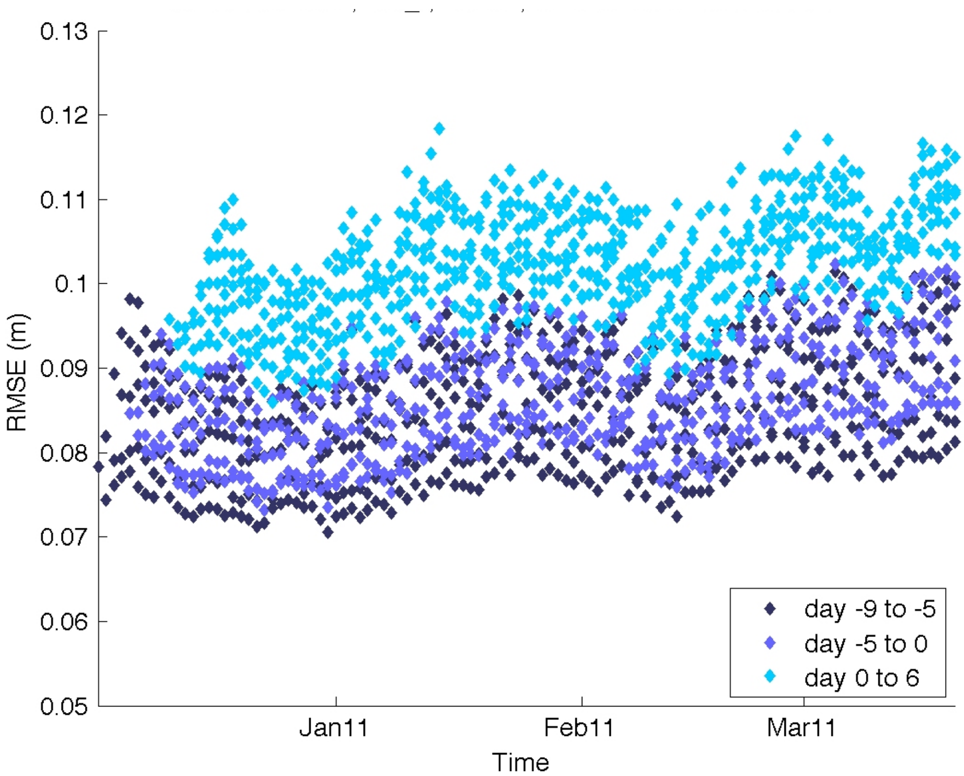

Fig. 44. The composite time series of RMSE of sea surface height anomaly from the four behind real-time analysis cycles. The shades of blue represent successive days of the daily mean output from OFAM2 for the behind real-time hindcast, near real-time hindcast and 7 day forecast. The RMSE is based on the Australian region and over the period 2nd Dec 2010 to 20 Mar 2011.

The performance of the OMv2 RMSE is summarised in Fig. 45 where the median and 99th percentile range of RMSE is shown as a bar for each day with a similar colour scheme. In this representation there is a monotonic increase in the median RMSE consistent with a skilful model. The hindcast RMSE also shows a more rapid initial error growth, which begins to asymptote with increasing forecast period. In addition the range of RMSE increases with increasing forecast period indicating a reduction in reliability. The RMSE for the BRT and NRT analyses is also shown in Fig. 45 in red. Both of these analyses are able to reduce the RMSE to the expected error of the observation of 5 cm. However, the RMSE of the 24 hr initialised model increases the RMSE by just under 3 cm. This is however a 50% improvement over OMv1, which is also shown in Fig. 45 in a similar pattern of grey scales. This is attributable to both an improved target analysis and the improved initialisation scheme described in section 3.5. The results for OMv1 shown in Fig. 45 demonstrate that the worst RMSE hindcast/forecast from OMv2 is now less than the best hindcast/forecast from OMv1. We note that the OMv1 does not preserve monotonicity indicating the influence of the uneven cycle pattern of 3 and 4 days. We also note that despite the obvious improvements in the model background field for each BODAS analysis, the statistics for BODAS are close to invariant. None the less we can assume that the reduction in forecast innovations results in more balanced analysis states and lower shock. The RMSE is therefore not sufficient in determining the quality of an analysis.

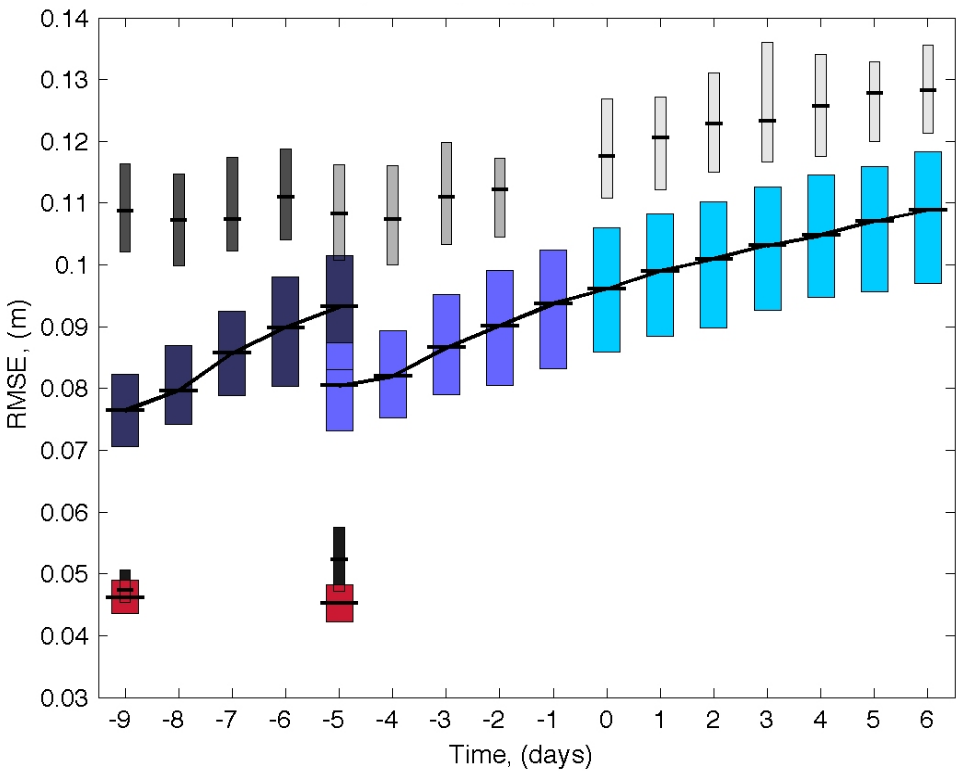

Fig. 45. The 99th percentile distribution RMSE of sea surface height anomaly from the composite of the four behind real-time analysis cycles. Red represents the distribution for the BODAS2 analysis and the shades of blue represent successive days of the daily mean output from OFAM2 for the initialisation and four day hindcast. The horizontal line represents the median RMSE for each distribution. The RMSE is based on the Australian region and over the period 2nd Dec 2010 to 20 Mar 2011. The 99th percentile distribution RMSE of sea surface height anomaly from the operational OMv1 system for the same period is shown in grey scale with difference shades representing the equivalent BRT, NRT and forecast cycles respectively.

The performance of the OMv2 anomaly cross-correlation (aCC) is summarised in Fig. 46 where the median and 99th percentile range of aCC is shown as a bar for each day with a similar colour scheme to Fig. 45. In this representation there is a monotonic decrease in the median aCC consistent with that expected of a skilful model. The hindcast aCC shows a rapid initial decline which begins to asymptote with increasing forecast period. In addition to the growth in the median aCC, the range of aCC also increases with increasing forecast period. The aCC for the BRT and NRT analyses are also shown in Fig. 46 in red. Both of these analyses show an aCC exceeding 0.9 with low variation throughout the trial period. However, similar to the RMSE, the aCC of the 24 hr initialised model decreases the aCC by just under 17%. This is however, a significant improvement over OMv1, which is also shown in Fig. 45 in a similar pattern of grey scales and a reduction of 36%. This is similar to the RMSE results and attributable to both an improved target analysis and the improved initialisation scheme. Although the distribution of OMv2 is consistently less than OMv1 the range of aCC for OMv2 overlaps with that of OMv1. This suggests that the pattern of eddies and fronts represented in OMv1 was closer to the observed, however, the amplitudes were significantly damped. Therefore the majority of improvement is in the introduction of more intense eddies/fronts into the model. The persistence of the performance indicates that the initialised information is being retained by the model. Similarly to the RMSE results the aCC statistics for BODAS are close to invariant. The aCC is therefore also not sufficient in determining the quality of an analysis.

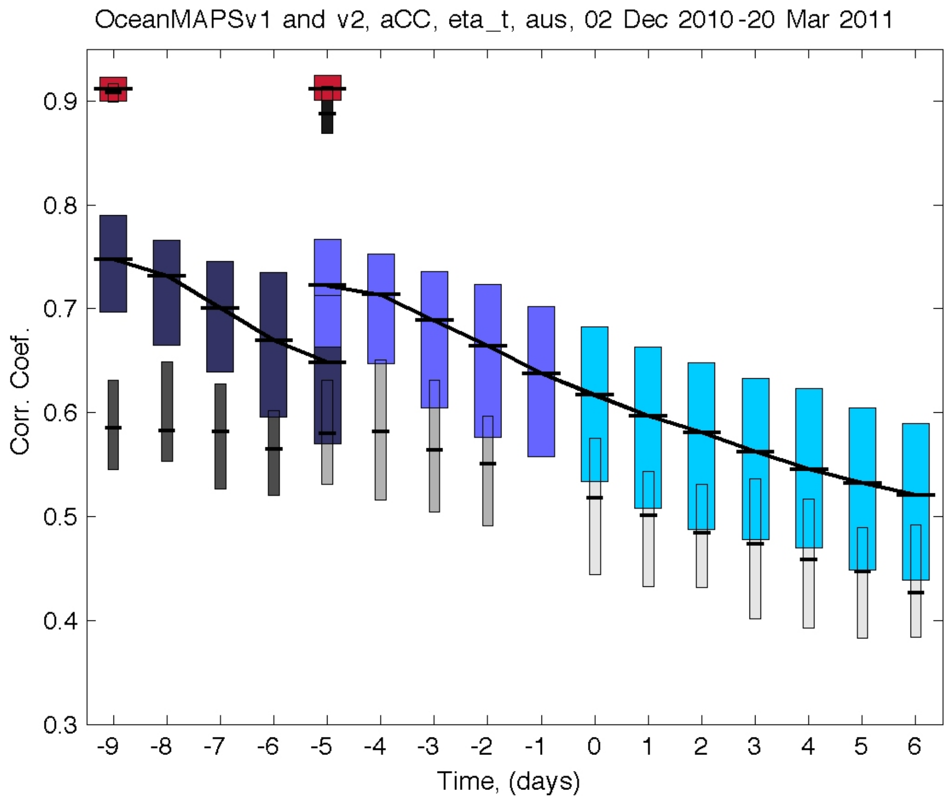

Fig. 46. The 99th percentile distribution of aCC of sea surface height anomaly from the composite of the four behind real-time analysis cycles. Red represents the distribution for the BODAS2 analysis and the shades of blue represent successive days of the daily mean output from OFAM2 for the initialisation and four day hindcast. The horizontal line represents the median RMSE for each distribution. The RMSE is based on the Australian region and over the period 2nd Dec 2010 to 20 Mar 2011. The 99th percentile distribution aCC of sea surface height anomaly from the operational OMv1 system for the same period is shown in grey scale with difference shades representing the equivalent BRT, NRT and forecast cycles respectively.

The OMv2 RMSE statistics for SST provides the time series in Fig. 47. Similar to the results for SSHA, the time series show a consistent monotonic increase in error for each cycle. The variability in RMSE time series for each day of the cycle is highly correlated with the errors in the initialised SST. The RMSE of the initialised BRT hindcast is approximately 0.05°C lower than the initialised NRT hindcast. This indicates that the initialisation of SST into OFAM2 benefits from the assimilation of a full orbit of altimetry that is obtained in the BRT cycle. Any reduction in latency of the coverage of altimetry will improve the forecast skill of SST. We note that the rate of increase in error decreases with each day of the BRT, NRT and forecast cycles.

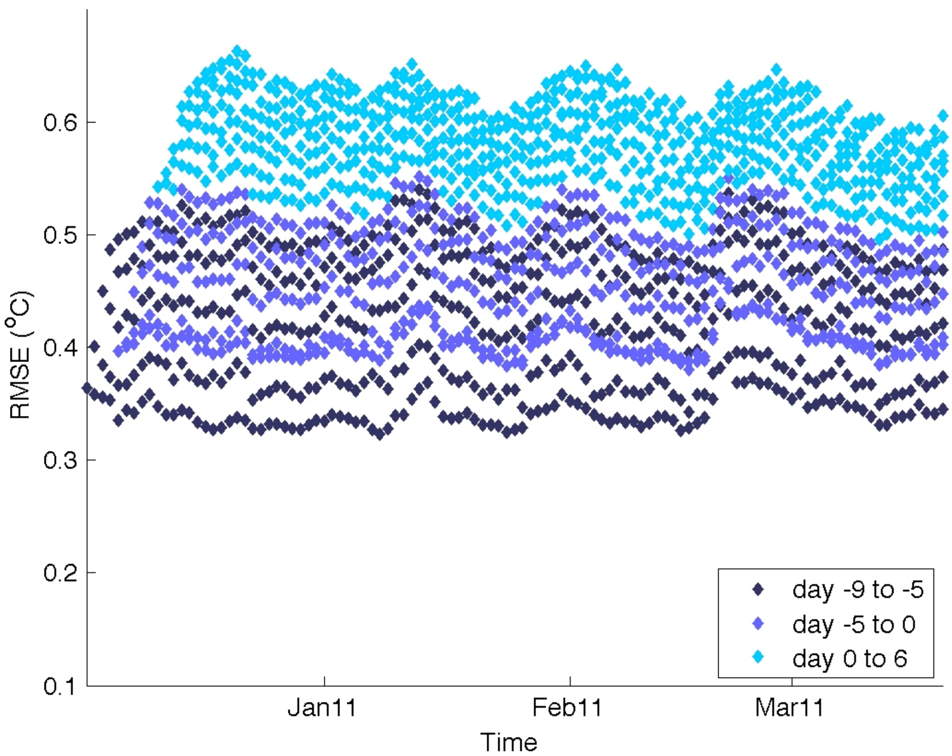

Fig. 47. Same as Fig.44 but for SST

The performance of the RMSE for SST is summarised in Fig. 48 where the median and 99th percentile range of RMSE is shown as a bar for each day with a similar colour scheme. There is a monotonic increase in the median RMSE consistent with that expected for a skilful model. Similarly, the hindcast RMSE grows rapidly initially and then asymptotes with increasing forecast period. Unlike the RMSE for SSHA, the range of RMSE does not increase significantly with increasing forecast period indicating a more reliable spread in forecast errors. This is in contrast to the spread for OMv1 shown in grey. The RMSE for the BRT and NRT analyses is shown in**Error! Reference source not found.** in red, which is approximately 0.1°C less than analyses for OMv1 shown in black. The median RMSE for the 24hr initialised model for the BRT cycle is less than the median RMSE for the BRT analysis for OMv1. Similar to SSHA we attribute this improvement to both a more balanced target analysis and the new initialisation scheme.

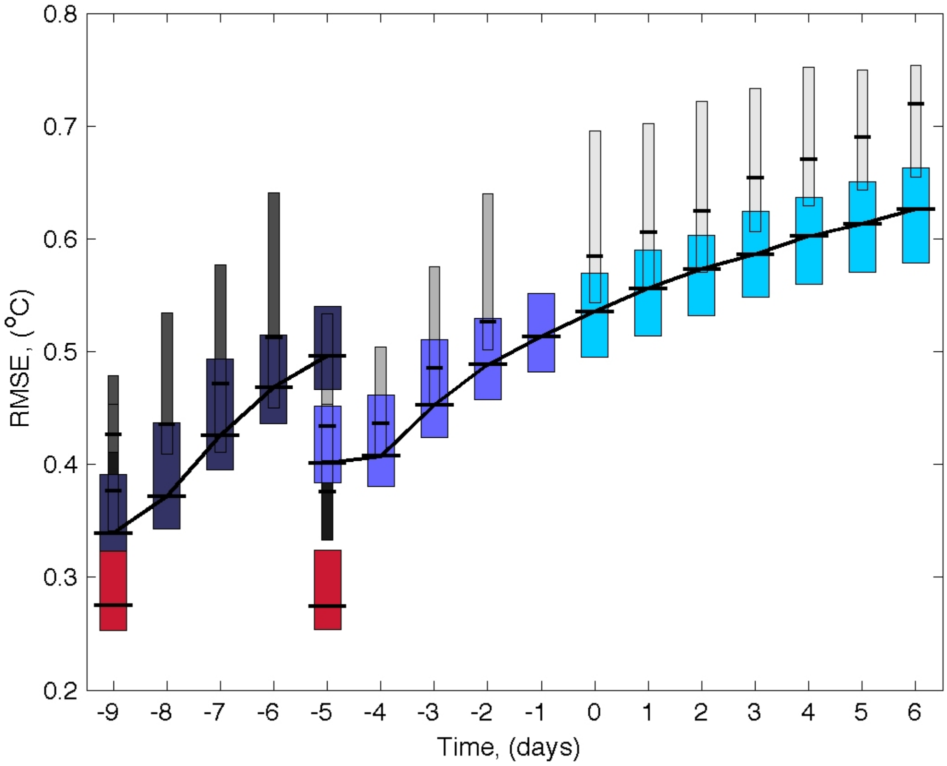

Fig. 48. Same as Fig.45 but for SST

The performance of the OMv2 aCC for SST is summarised in Fig. 49 where the median and 99th percentile range of aCC is shown as a bar for each day with a similar colour scheme to Fig. 48. In this representation there is a monotonic decrease in the median aCC consistent with that expected for a skilful model. Similar to the RMSE results, the hindcast aCC also shows a more rapid initial decline which begins to asymptote with increasing forecast period. Unlike the RMSE the range of aCC increases with increasing forecast period. The aCC for the BRT and NRT analyses are also shown in Fig. 49 in red. Both of these analyses show an aCC exceeding 0.95 with low variation throughout the trial period. The median aCC of the 24hr initialised model for both the BRT and NRT remain above 0.9. This shows a measurable improvement over OMv1, which is also shown in Fig. 49 in a similar pattern of grey scales. The decline in aCC with increasing forecast period shows that the model is retaining and skilfully propagating the information compared with OMv1.

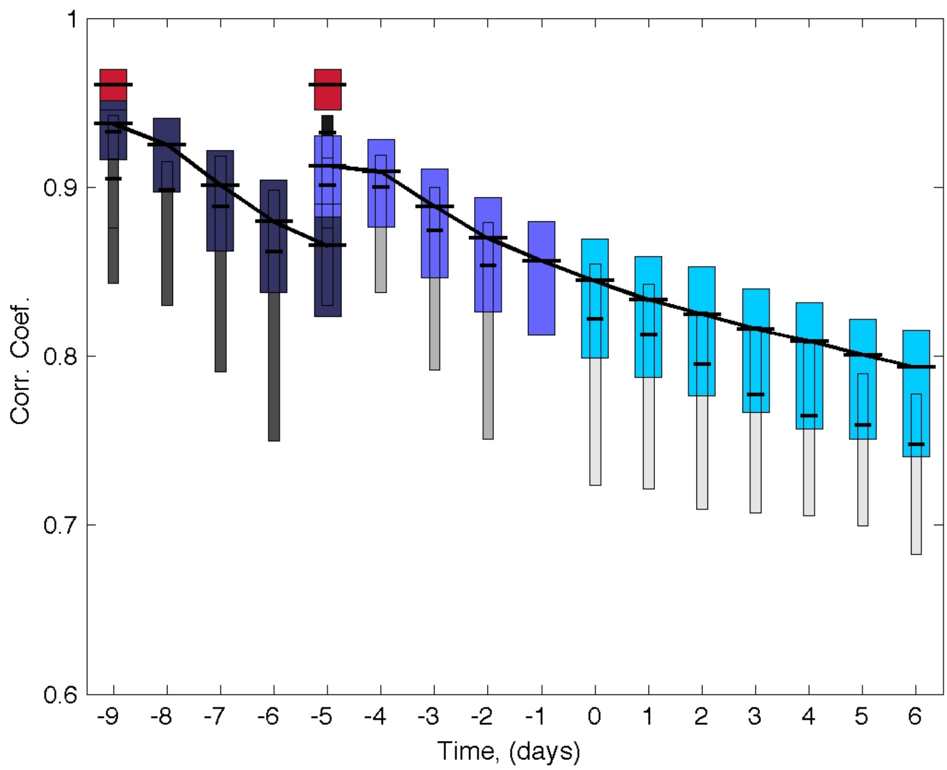

Fig. 49. Same as Fig. 46 but for SST where the anomaly cross-correlation is performed relative to the seasonal cycle.

4.5 SENSITIVITY OF PERFORMANCE

The performance of OMv1 as measured by RMSE for SSHA, Fig. 38 and SST, Fig. 41 show variability for the five day BRT hindcast is on the order of +9%/-11% and +9%/-6% respectively. The sensitivity of the forecast performance can be assumed to be related to the available coverage and quality of observations as well as the influence of atmospheric fluxes from weather systems. A gross measure of the relationship to observations is performed using a time-lagged correlation between the time series in Fig. 34 and the corresponding RMSE time series for each day of the BRT cycle as shown in Fig. 50. More formally, the correlation is given by,

$$\rho_\tau = \frac{\sum_{i=1}^{N} (\mathrm{no}_i - \overline{\mathrm{no}})(\mathrm{rmse}_{i+\tau} - \overline{\mathrm{rmse}})}{\left(\sum_{i=1}^{N} (\mathrm{no}_i - \overline{\mathrm{no}})^2 \sum_{i=1}^{N} (\mathrm{rmse}_{i+\tau} - \overline{\mathrm{rmse}})^2 \right)^{1/2}}$$

where no is the number of observation in Fig. 34, $\mathrm{rmse}_{i+\tau}$ is the time series of root mean square error, $i \in [-9,-6]$ represents the days of the BRT hindcast and $\tau \in [1,4]$ represents the timelag applied to the RMSE time series.

Figure 50a shows a negative correlation coefficient of approximately -0.3 for the first 24hrs of the hindcast for SSHA. This negative correlation also consistently propagates through successive days of the 48-96hr hindcasts lagged by the equivalent number of lagged days. The correlation coefficient continues to increase in magnitude for a further two days indicating that the change in performance due to observations continues to grow after the initialisation enhancing the correlation for SSHA. We interpret this as related to the large observation window and the long correlation timescales.

Figure 50b shows a similar negative correlation coefficient of approximately -0.3 for the first 24hrs of the hindcast for SST. This negative correlation also consistently propagates through successive days of the 48-96hr hindcasts by the equivalent number of lagged days. In each case the magnitude of the correlation increases indicating the model error grows from the initial perturbation. The magnitude of correlation for subsequent cycles following this initial shock declines more rapidly than for SSHA due to the shorter correlation time scale of SST as well as the shorter observation time windows.

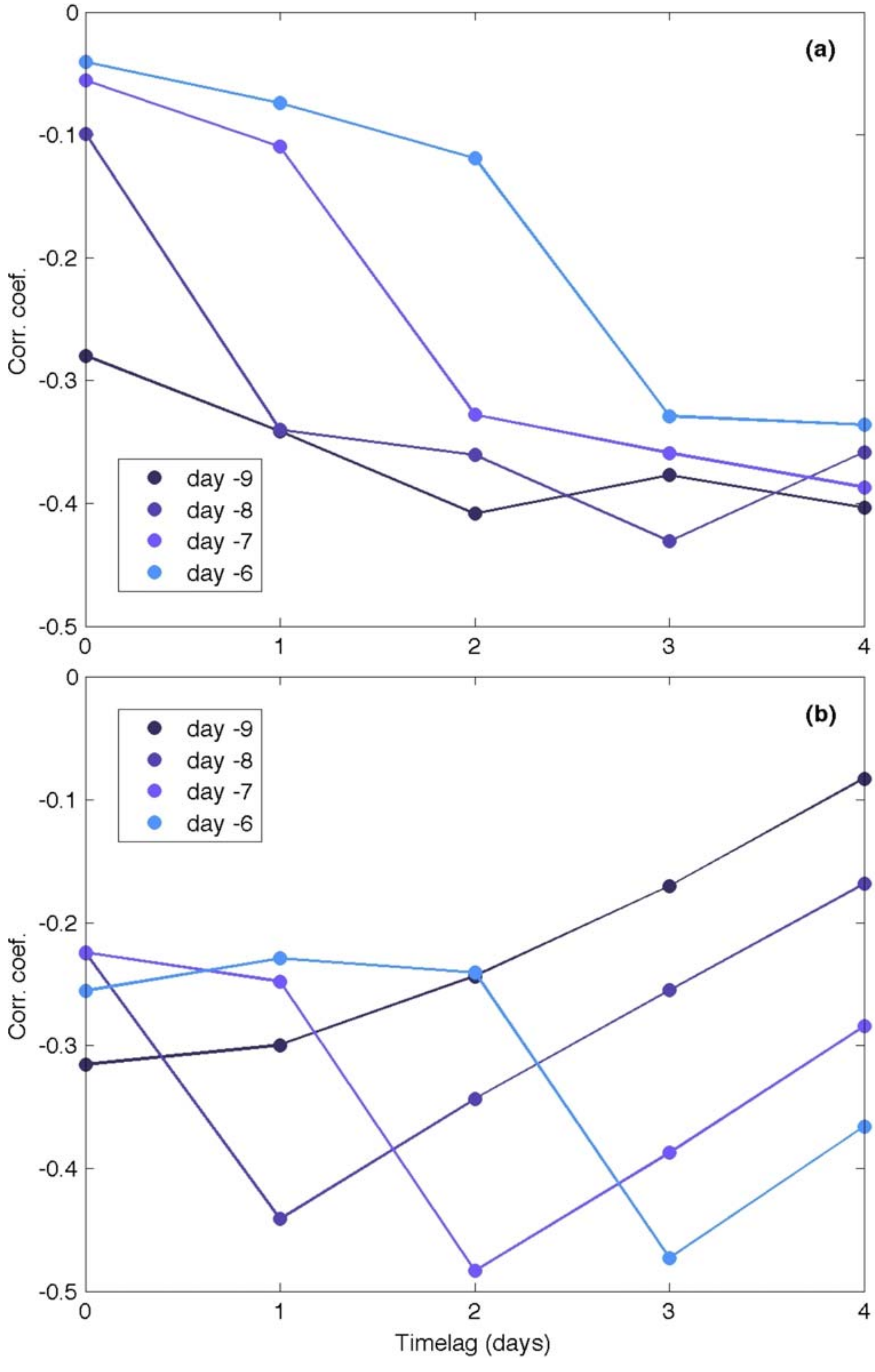

Fig. 50. Time lagged correlation of the total observation time series from Fig. 34 and the RMSE time series for (a) SSHA from Fig. 44 and (b) SST from Fig. 47.

4.6 INDEPENDENCE OF THE MULTI-CYCLE FORECASTS

The OMv2 has been constructed using four independent cycles to obtain a daily ocean forecast. This was adopted due to the coverage of altimetry to minimise the over-fitting as outlined in section 3.1.1 but was also a deliberate, though subtle, design choice to use as a 4-member multi-cycle lagged ensemble. A objective of this design is to increase the independence between the four cycles. The independence is measured by applying a singular value decomposition to the daily average forecasts of SSHA for the Australian region from the four cycles. The independence is then compared through the trial period by comparing the squared magnitude of the singular values as shown in Fig. 51. Initially there is very little independence as the four cycles were bootstrapped from the single hindcast of OMv1. Throughout the trial period the leading vector declines to approximately 70% with a corresponding growth in variance explained by the three other vectors. A similar distribution of variance is obtained for the 48hr and 72hr analyses (not shown) although a slight decline in the variance of the leading vector. By the end of the trial period the variance appears to reach an equilibrium where the leading vector remains significantly greater than the other three members and can be interpreted as the ensemble mean.

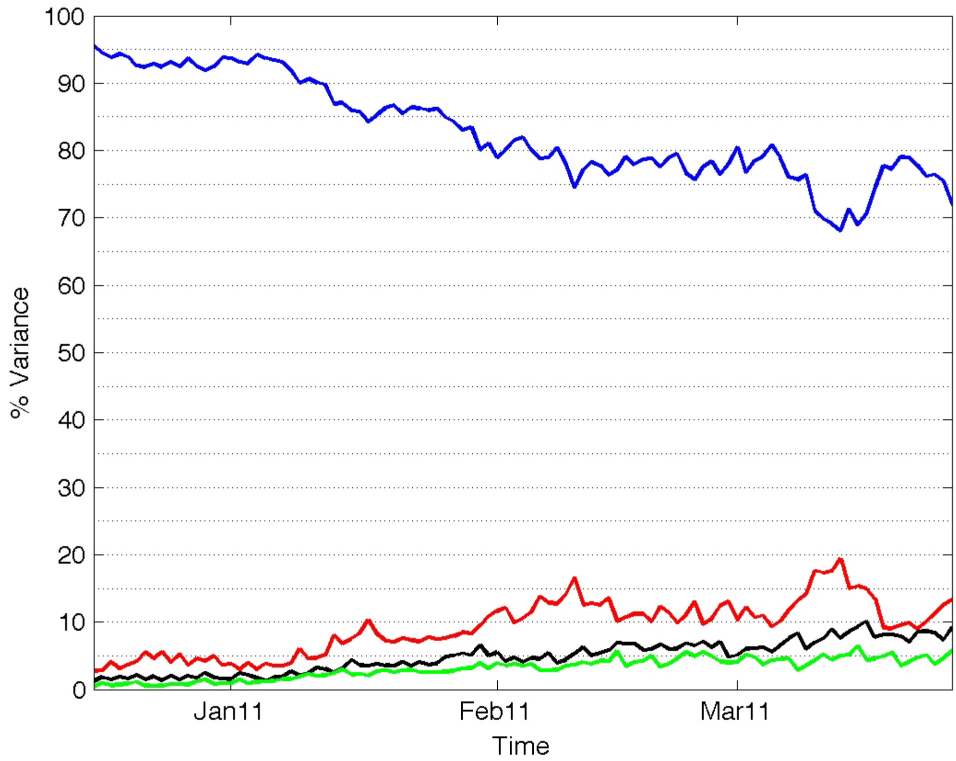

Fig. 51. The percentage variance in the singular values from a singular value decomposition of the 24 hr average forecast of SSHA from the four cycles. The percentages are calculated for each day of the trial period.

A similar analysis performed on the ensemble anomalies about the ensemble mean is shown in Fig. 52. The variance in the leading vector is initially approximately 60% and declines to a value of 50%. At the end of the trial period the two remaining vectors explain 30% and 20% of the variance respectively.

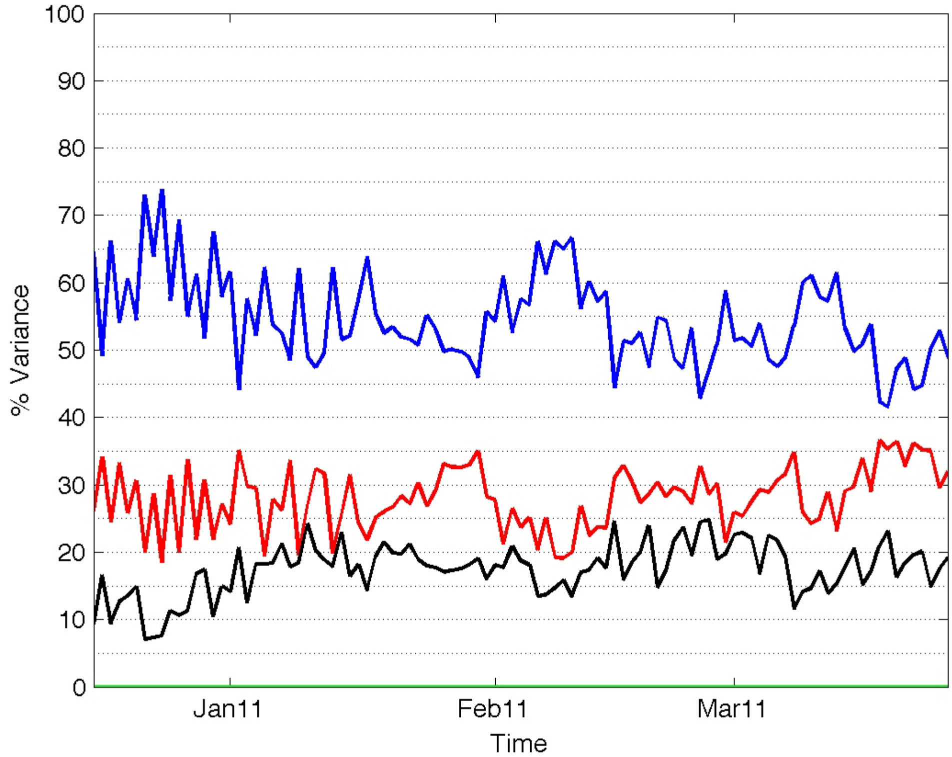

Fig. 52. The percentage variance of the singular values from a singular value decomposition of the ensemble anomalies from the 24 hr average forecasts from the four cycles. The forecasts correspond to the (24hr, 48hr, 72hr, 96hr) and time-lags of (0hr, 24hr, 48hr, 72hr). The percentages are calculated for each day of the trial period.

Extending the analysis to include two additional lagged ensemble members asymptotes to a total contribution of less than 10% of the total variance as shown in Fig. 53. The additional members are composed of longer lead time forecasts from earlier forecasts from two of the cycles already included in the analysis shown in, Fig. 52. Although the cycles have been initiated four days earlier and have accumulated additional error from the longer period forecast fluxes this is insufficient for either member to contribute substantially to the total variance. However, the contribution is not negligible and there is clearly a small gain from the use of up to an 8-member ensemble. In practice this is not possible as the current forecast period is 7 days such that the multi-cycle lagged ensemble for the first 24hrs would be limited to 7-members and the 48hr to 6-members etc.

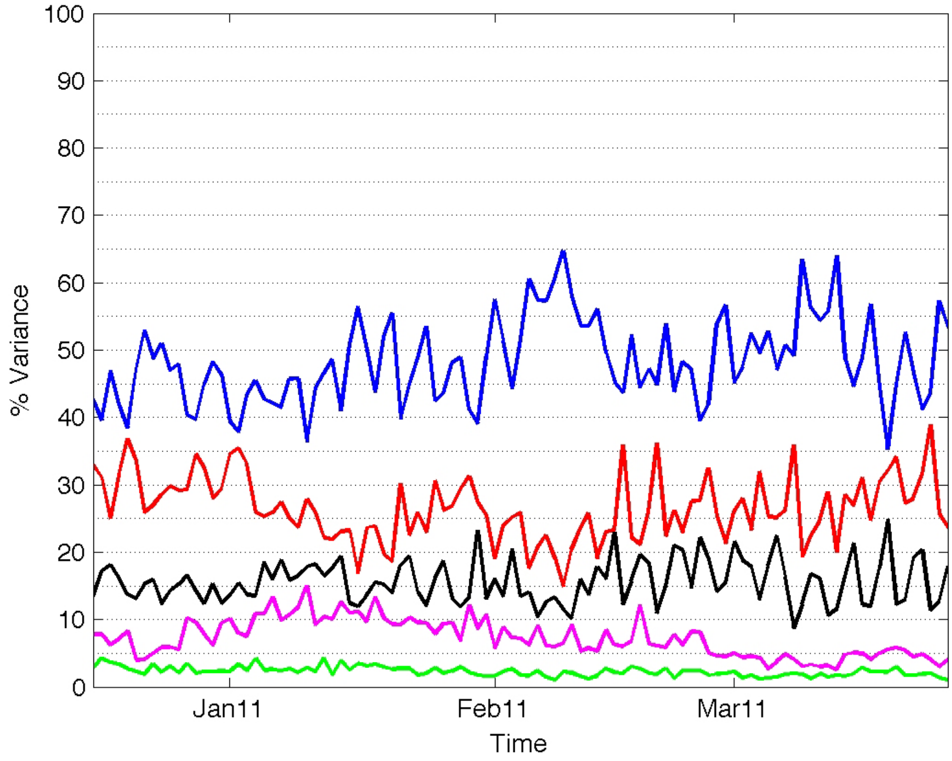

Fig. 53. The percentage variance of the singular values from a singular value decomposition of the ensemble anomalies from the 24hr average forecasts from the four cycles. The forecasts correspond to the (24hr, 48hr, 72hr, 96hr, 120hr, 144hr) and time-lags of (0hr, 24hr, 48hr, 72hr, 96hr, 120hr). The percentages are calculated for each day of the trial period.

The analysis shows that the 4-member multi-cycle lagged forecasts do provide significant independent information relative to the ensemble mean. This is a distinct improvement over the use of sequential time-lagged ensembles as has been used in the past for numerical weather prediction (e.g, Brankovic, et al., 1990 and Hoffman and Kalnay, 1983). The time-lagged ensemble shows great promise for all of the applications for ensembles such as guidance information on forecast spread and hybrid-data assimilation. This remains a poor-man's ensemble; however, it is an effective strategy. This design will likely remain in place for OMv3, which will target a computationally more expensive global 0.1 grid and whilst the available altimetry remains at the current coverage and latency or lower.

4.7 MULTI-CYCLE LAGGED ENSEMBLE FORECASTING

OceanMAPSv2 offers a wide range of potential products and services. There is now a number of possible best analyses: (a) a time series of the BRT BODAS analyses across all cycles, e.g., Fig. 54d (b) a time series of the BRT OFAM2 initialised hindcast across all cycles, e.g., Fig. 54c (c) a simple average of the BRT hindcasts, e.g., Fig. 54a or (d) a weighted average not shown. All of these products can be objectively compared against the observations as well as qualitatively compared with the CSIRO analysis as shown in Fig. 54b for the Tasman Sea for this example.

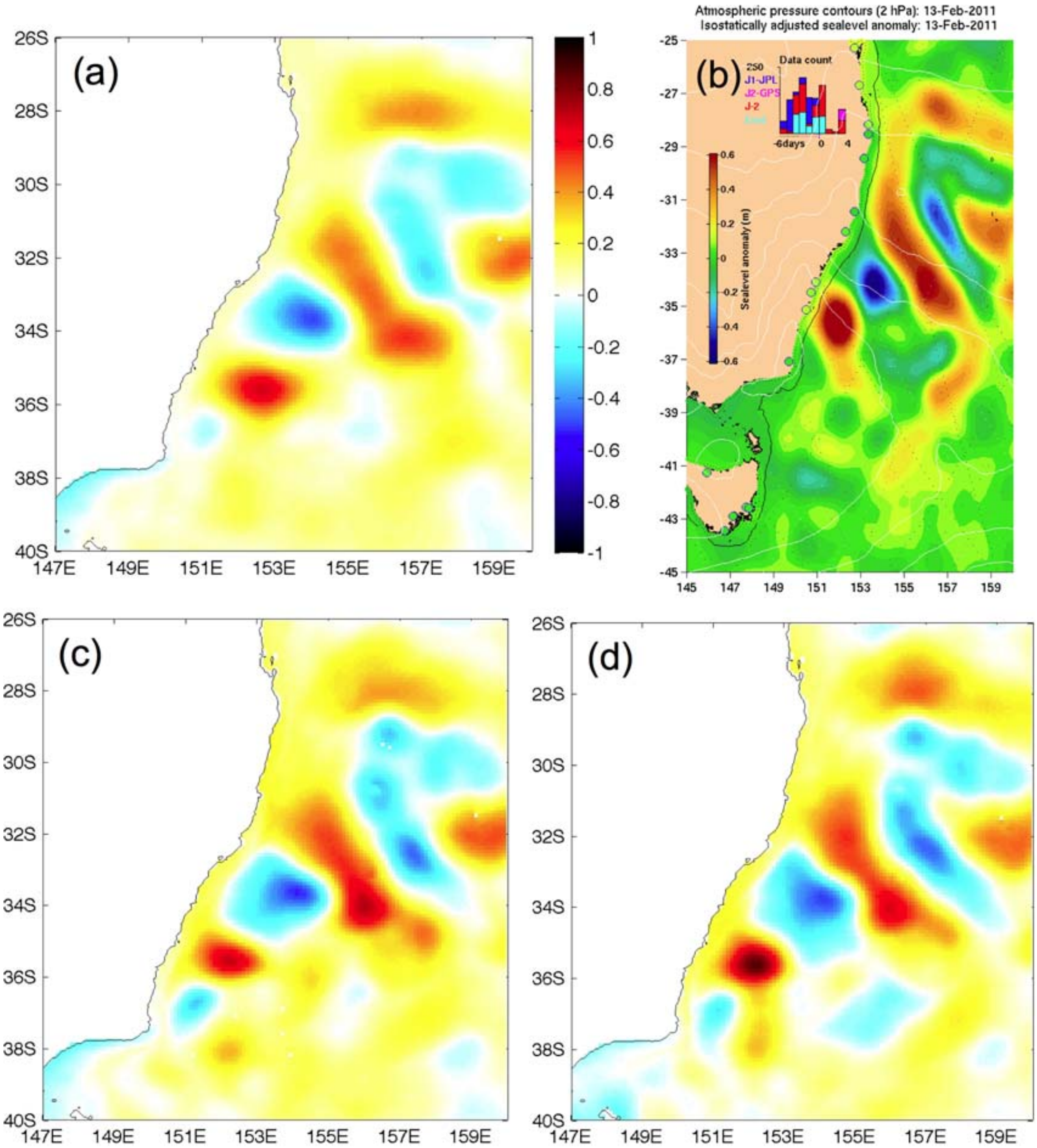

Fig. 54. An example of the type of analysis products that can be derived from the OMv2 (a) Ensemble mean, (b) corresponding CSIRO analysis (Griffin et al.,), (c) Initialised hindcast, (d) Hindcast analysis

For the forecasts there are several realisation for a given day that were shown, in section 4.6, to have sufficient independence to support a weighted multi-cycle lagged ensemble average and variance. For the present purpose we will follow the definition given in Brankovic et al., (1990) for a simple uniform weighted ensemble and revisit a weighted ensemble in future work.

Let F_i be a forecast field produced by one member of an ensemble (i=1,...,N). The ensemble mean is given by,

$$\overline{F} = \frac{1}{N}\sum_{i=1}^{N} F_i$$

The mean square spread of the ensemble is given by,

$$\Delta^2 = \frac{1}{N}\sum_{i=1}^{N}\left|F_i - \overline{F}\right|^2$$

and the anomaly correlation for the ensemble mean is given by,

$$\rho(\overline{F}) = \frac{\overline{F} \bullet A}{\left|\overline{F}\right| \bullet |A|} = \frac{\left|\overline{F}\right|^2 + |A|^2 - |E|^2}{2\left|\overline{F}\right| \bullet |A|}$$

where $\overline{E} = \overline{F} - A$ and A represent the verifying analysis.

Using a 4-member ensemble of the BRT hindcasts we estimate the variance for each day of the trial period and then take an average of these variances as shown in Fig. 55 for SSHA, SST and SSS. This provides the spatial distribution of the areas that both have the most frequent and largest amplitude variance or spread.

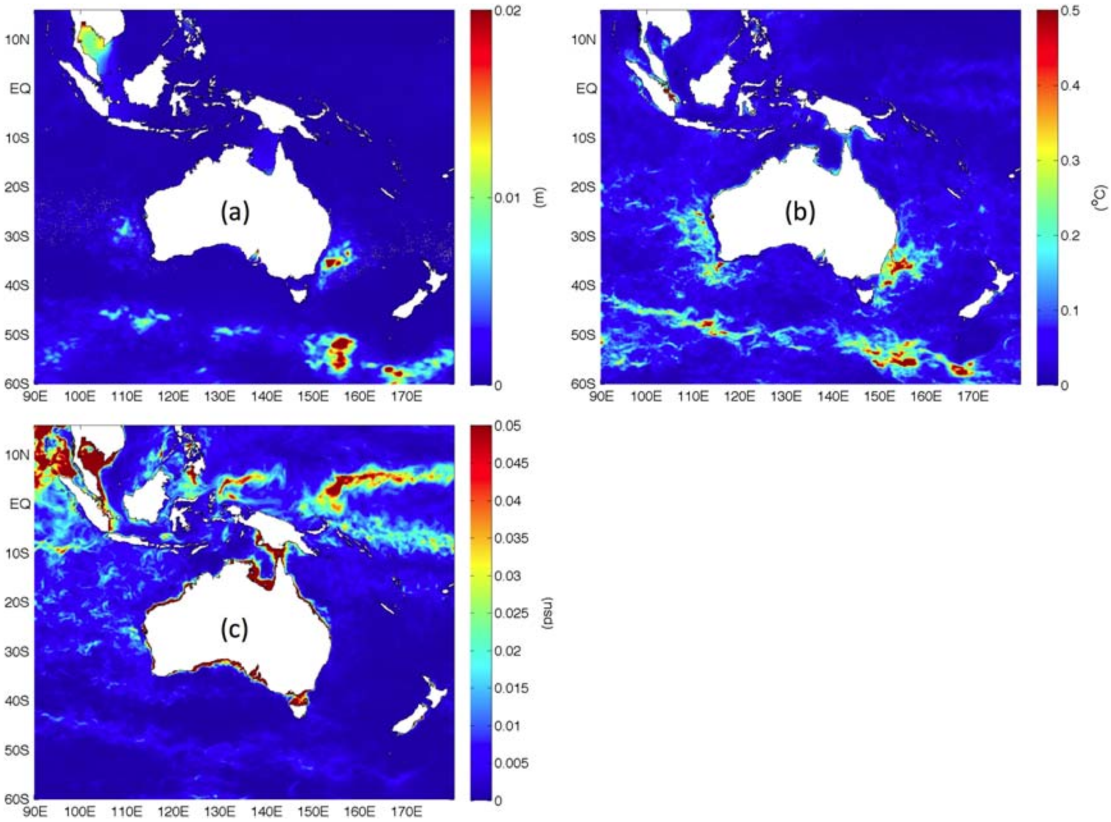

Fig. 55. Mean ensemble variance for the high resolution region for the period 2nd Dec to 20th March 2011, (a) SSHA, (b) SST and (c) SSS.

As expected there is some obvious correspondence between the distribution of ocean variability modelled by OFAM2 shown in Fig. 20 and the multi-cycle lagged ensemble variance. The ensemble variance is consistently largest where the modelled variability is largest as expected for a well behaved ensemble forecasting system. We note any correspondence is qualitative due to the difference in sample size, that is, a 14 year SPINUP time-lagged ensemble, 3 months (effectively one season and one La Nina).

Note that sea surface height variability in the coastal region is comparable to the open ocean in the OFAM2 spinup, Fig. 20. However, the multi-cycle lagged ensemble shows a decline in variance at the coast, Fig. 55a. This has been previously attributed to the relationship of this variability to atmospheric winds, which are common for all of the hindcasts. The multi-cycle lagged ensemble for the forecasts is expected to show higher variability in this region reflecting the errors in the applied forcing. The open ocean SSHA mean ensemble variance is dominated by a region in the southern Tasman Sea, which is also where the largest biased increments are applied, Fig. 31d. The other visible sources of ensemble variance is for the major ocean currents, East Australian Current, Leeuwin Current and Antarctic Circumpolar Current. A similar distribution can be seen for the ensemble variance of SST in Fig. 55b however, the structure appears to be a composite of fronts. The region in the southern Tasman Sea does not show up as a significant bias, which is also reflected in a smaller increment bias in Fig. 33b. Figure 55c shows that the SSS has a distribution unique from SSHA and SST where the ensemble variance is dominated by the variability in the tropics. There is however some significant ensemble variance shown in the Leeuwin Current

The ensemble variance can be used to provide guidance to applications on the regions of the ocean showing ensemble spread above threshold values. Such information could be used to guide decision making on the use of the products or whether to consider the use of the ensemble information. An example is shown in Fig. 56 for ensemble variance of SSHA exceeding 0.02 m for four successive days. The ensemble variance tends to be located in the core of eddies, e.g., 156E, 30S or along fronts e.g., 154E, 32S. The regions identified show good continuity throughout the four days, indicating they appear to be tracking features that are evolving.

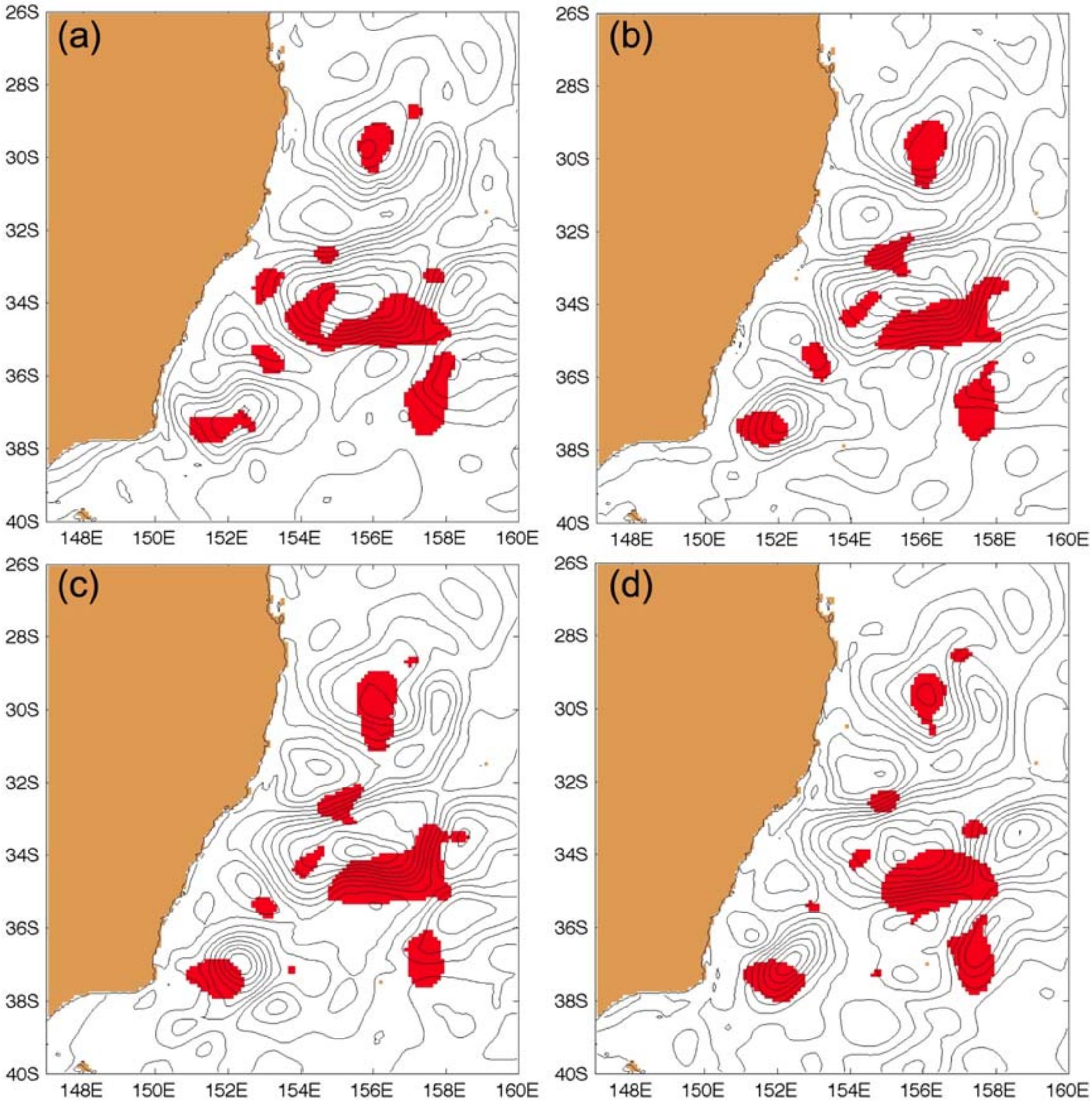

Fig. 56. Regions where the multi-cycle lagged ensemble variance of SSHA exceeds 0.02 m shown in red. The regions are overlayed on the contours of the ensemble mean of SSHA in the Tasman Sea for each day shown (a) 14th, (b) 15th, (c) 16th and (d) 17th March 2011.

5. CONCLUSIONS

The performance of OMv2 for all of the metrics presented is superior to OMv1

The median performance is lower for SSHA and SST with the worst SSHA performance for OMv2 measurably less than the best SSHA performance for OMv1. OMv2 includes several improvements such as upgrades to the ocean model, data assimilation system, initialisation and atmospheric forcing. This study has not attempted to identify or attribute improvements in performance to specific improvements to the system. The results however, do indicate that a significant portion of the improvement can be attributed to the initialisation and the retention of this information with slower error growth curves during the forecast period.

The BRT 24hr initialised performance is consistently less than the NRT for SSHA due to the impact of the full coverage. The retention of the full orbit of Jason 1 and Jason 2 has also a measurable impact on the performance of SST. The performance of the system is therefore improved through the maintenance of a best estimate ocean state. In practice this also provides greater robustness for delays or failures in the delivery of observations to be restored.

The performance measures used, apply equal weighting to all of the super-observations. This will underestimate the true performance of the systems.

A more precise measure could apply a weighting based on the observation errors assigned by the analysis which includes age penalties. However, for the purpose of differentiating OMv1 and OMv2 this is sufficient and avoids adding additional bias through the estimation of the error.

Since the super-observations were applied to the BRT and NRT cycles the performance of these analyses is expected to be inflated due to the lack of independence. The degree to which the analysis fits the super-observations is relevant to the evaluation of the system presented here and demonstrates the relative efficiency of the initialisation scheme. The observation windows applied for each data type determine the timescale by which the reference observations are completely independent. For both SSHA and SST this will occur from -2 days through to the full forecast. In the case of SSHA, we expect that due to the sparse nature of altimetry tracks the performance metrics of the nowcast and day 1 forecast will be reliable.

The performance of the system is anti-correlated with the coverage of the observations with correlations magnitude of up to 0.5. We conclude that there is no redundancy in the observing system for OMv2 and that analysis errors are sensitive to small changes in the observing system. The pattern of analysis errors is shown to be closely correlated with the subsequent forecast errors of sea level anomaly indicating it has a leading role in the forecast error for this variable. This is not the case for SST where the errors grow more rapidly and approach saturation from the errors of the surface fluxes and mixed layer parameterisation.

The four cycle design was implemented to achieve a daily forecast but also to minimise the over-fitting of SSHA observations from the large data windows. The benefit of this design was the potential increased independence of the cycles for use as a lagged ensemble. The analysis shows that the multi-cycle lagged forecasts provide significant independent information relative to the ensemble mean. This is a distinct improvement over the use of sequential time-lagged ensembles as has been used in the past. The multi-cycle lagged ensemble shows great promise as a guidance information on forecast spread and hybrid-data assimilation. This design will likely remain in place for OMv3, which will target a global 0.1 grid and whilst the available altimetry remains at the current coverage and latency or lower.

The new design provides a number of additional products and opportunities for multi-cycle lagged ensembles. This represents a much greater choice for the user, which will take some time to be fully exploited. Further detailed analyses on these products will help to guide the optimum choices.

Despite the clear improvement in performance of OMv2 there remain many opportunities for further improvement in all aspects. For example the observation errors do not exploit First-Guess at Analysis Time. The observation error model for altimetry could be further optimised relative to the observed variability. The adaptive initialisation scheme introduced is the first implementation and provides a number of parameters that could be further optimised. The time-lagged ensemble also provides opportunities to introduce errors of the day into a hybrid data assimilation scheme. Several strategies to improve the air-sea fluxes toward a fully coupled system were also discussed earlier. Many of these area will be examined during a follow-on project BLUElink-3.

The introduction of a daily forecast cycle provides multiple model representations for a single day and a wide-range of product options. A new and unique naming convention has been introduced to identify the data products. For example the four cycles are labelled 00, 01, 02 and 03. In addition, the data product metadata has been augmented to meet a number of conventions. A complete description can be obtained through, Bureau of Meteorology, (2011) and available online (http://www.bom.gov.au/marine/).

Finally we note for the user a word of caution relating to the robustness of the ocean observing system. In particular, coverage of satellite altimetry is expected to decline with both Jason-1 and Envisat ceasing in the next year or so. There are a couple of options to help minimise these losses: (a) Cryosat-2 will be made available; (b) AltiKa will occupy a similar orbit to Envisat and (c) the Chinese satellite HY-2B offers altimetry. It is anticipated that there will be a decline in performance for all global systems during the lifetime of OMv2.

6. ACKNOWLEDGMENTS

The authors gratefully acknowledge the contributions to the quality control system by Dr Konstantin Belyaev and the satellite altimetry by Dr Leon Majewski. The research and development critically depends upon the international space agencies, NOAA, ESA, CNES and NASA and the international science teams GHRSST and OSTST. The partners for the BLUElink-3 project, the Bureau of Meteorology, CSIRO and the Royal Australian Navy are also gratefully acknowledged.

7. REFERENCES

Andreu-Burillo, I., Brassington, G.B., Oke, P.R. and Beggs, H. 2009: Including a new data stream in BLUElink ocean data assimilation, *Australian Meteorological and Oceanographic Journal*, 59, 77- 86.

Balay, S., Brown, J., Buschelman, K., Eijkhout, V., Gropp, W.D., Kaushik, D., Knepley, M. G., Curfman McInnes, L., Smith, B.F. and Zhang, H. 2010: ' *PETSc Users Manual'*, ANL-95/11 Revision 3.1, Argonne National Laboratory.

Brankovic, C., Palmer, T.N., Molteni, F., Tibaldi S. and Cubasch, U. 1990: Extended-range predictions with ECMWF models: Time-lagged ensemble forecasting. *Q. J. R. Meteorol. Soc*., 116, 867-912.

Brasseur, P. and Verron. J. 2006. The SEEK filter method for data assimilation in oceanography: A synthesis. *Ocean Dynamics,* 56:650–661.

Brassington, G.B., Pugh, T., Spillman, C., Schulz, E., Beggs H., Schiller A. and Oke, P.R. 2007: BLUElink> Development of operational oceanography and servicing in Australia, *Journal of Research and Practice in Information Technology*, 39, 151-164.

Brassington, G.B., Hines, A., Dombrowsky, E., Ishizaki, S., Bub, F. and Ignaszewski, M. 2010: "Short To Medium-Range Ocean Forecasts: Delivery And Observational Requirements" in *Proceedings of OceanObs'09: Sustained Ocean Observations and Information for Society (Vol. 1),* Venice, Italy, 21-25 September 2009, Hall, J., Harrison, D. E. & Stammer, D., Eds., ESA Publication WPP-306, doi:10.5270/OceanObs09.pp.08.

Brassington, G.B. 2011: System design for operational ocean forecasting, In: A. Schiller and G. B. Brassington, Operational Oceanography in the 21st Century, doi 10.1007/978-94-007-0332-2_18, *Springer Science+Business Media* B. V. 2011, pp441-486.

Bureau of Meteorology, national meteorological and oceanographic group, 2007: Implementation of OceanMAPS (BLUElink> Ocean Forecast System), numerical prediction operations bulletin no.69, 18 October 2007.
(available http://web.bom.gov.au/nmoc/stan/opsbull/apob69.pdf).
Bureau of Meteorology. 2011. The Ocean Model And Prediction System (OceanMAPS) Revision 2.0, OFAM2 Product Specification, 1st June 2011
(available http://www.bom.gov.au/marine/).

Carval, T., Keeley, B., Takatsuki, Y., Yoshida, T., Loch, S., Schmid, C., Goldsmith, R., Wong, A., McCreadie, R., Thresher A. and Tran, A. 2003. Argo data management: User's manual, version 2.01, 2003, ar-um-02-01.

Chassignet, E.P., Hurlburt, H.E., Metzger, E.J., Smedstad, O.M., Cummings, J., Halliwell, G.R., Bleck, R., Baraille, R., Wallcraft, A.J., Lozano, C. and others. 2009. US GODAE: Global Ocean Prediction with the HYbrid Coordinate Ocean Model (HYCOM). *Oceanography* 22(2):64–75.

Cummings, J.A. 2005. Operational multivariate ocean data assimilation. *Quarterly Journal of the Royal Meteorological Society* 131:3,583–3,604.

Cummings, J.A., Brassington, G., Keeley, R., Martin, M. and Carval, T. 2010: GODAE ocean data quality control intercomparison project. Proceedings, Ocean Obs '09, Venice, Italy. 5 pp. in *Proceedings of OceanObs'09: Sustained Ocean Observations and Information for Society (Vol. 1)*, Venice, Italy, 21-25 September 2009, Hall, J., Harrison, D.E. and Stammer, D., Eds., ESA Publication WPP-306, doi:10.5270/OceanObs09.pp.08.

Cummings, J.A. 2011: Ocean data quality control, In: A. Schiller and G. B. Brassington, Operational Oceanography in the 21st Century, doi 10.1007/978-94-007-0332-2_18, *Springer Science+Business Media B. V.* 2011, pp91-121.

Dai, A. and Trenberth, K.E. 2002: Estimates of freshwater discharge from continents: Latitudinal and seasonal variations. *J. Hydrometeorology*, 3, 660–687.

Davidson, F., Allen, A., Brassington, G.B., Breivik, O., Daniel, P., Kamachi, M., Sato, S., King, B., Lefevre, F., Sutton M. and Kaneko, H. 2009: Application of GODAE ocean current forecasts to search and rescue and ship routing, *Oceanography*, 22(3), 176-181.

Dee, D.P. 2005: Bias and data assimilation. *Q. J. R. Meteorol. Soc.*, 131:3323– 3342, 2005.

Dee, D.P., Uppala, S.M., Simmons, A.J., Berrisford, P., Poli, P., Kobayashi, S., Andrae, U., Balmaseda, M.A., Balsamo, G., Bauer, P., Bechtold, P., Beljaars, A.C.M., van de Berg, L., Bidlot, J., Bormann, N., Delsol, C., Dragani, R., Fuentes, M., Geer, A.J., Haimberger, L., Healy, S.B., Hersbach, H., Hólm, E.V., Isaksen, L., Kållberg, P., Köhler, M., Matricardi, M., McNally, A.P., Monge-Sanz, B.M., Morcrette, J.-J., Park, B.-K., Peubey, C., de Rosnay, P., Tavolato, C., Thépaut, J.-N. and Vitart, F. 2011: The ERA-Interim reanalysis: configuration and performance of the data assimilation system, *Q. J. Roy. Soc. Meteorol.*, 137, 553-597, doi: 10.1002/qj.828.

Desai, S.D., Haines, B.J. and Case, K. 2003: Near real time sea surface height anomaly products for Jason-1 and Topex/Poseidon user manual, JPL D-26281, Jet Propulsion Laboratory, California Inst. Of Tech.

Divakaran, P. and Brassington, G.B. 2011: Arterial ocean circulation of the Southeast Indian *Ocean Geophys. Res. Lett.*, doi:10.1029/2010GL045574.

Dombrowsky, E., Bertino, L., Brassington, G.B., Chassignet, E.P., Davidson, F., Hurlburt, H.E., Kamachi, M., Lee, T., Martin, M.J., Mei S. and Tonani, M. 2009: GODAE systems in operation, *Oceanography*, 22(3), 80-95.

Donlon, C.J., Minnett, P., Gentemann, C., Nightingale, T.J., Barton, I.J., Ward B. and Murray, J. 2002: Towards improved validation of satellite sea surface skin temperature measurements for Climate Research, *J. Climate*, 15, No. 4, 353-369.

Donlon, C., Casey, K., Robinson, I., Gentemann, C., Reynolds, R., Barton, I., Arino, O., Stark, J., Rayner, N., Le Borgne, P., Poulter, D., Vazquez-Cuervo, J., Armstrong, E. Beggs, H., Llewellyn-Jones, D., Minnett, P., Merchant C. and Evans, R. 2009: The GODAE High-Resolution Sea Surface Temperature Pilot Project, *Oceanography*, 22, 34-45

Griffies, S.M., Harrison, M.J. and Pacanowski. R.C. 2008. A Technical Guide to MOM4. *GFDL Ocean Group Technical Report No 5*. NOAA/Geophysical Fluid Dynamics Laboratory

Griffies, S.M. 2010: Elements of MOM4p1, *GFDL OCEAN GROUP TECHNICAL REPORT NO. 6*, NOAA/Geophysical Fluid Dynamics Laboratory Feb 2010. pp444.

Hall, J., Harrison D.E. and Stammer, D., Eds., 2011: Proceedings of OceanObs'09: Sustained Ocean Observations and Information for Society *(Vol. 1)*, Venice, Italy, 21-25 September 2009, *ESA Publication* WPP-306, doi:10.5270/OceanObs09.pp.08

Hoffman R. and Kalnay, E. 1983: Lagged average forecasting, an alternative to Monte Carlo forecasting, Tellus, 35A, 100-118

Hurlburt, H.E. and Hogan, P.J. 2000: Impact of 1/8° to 1/64° resolution on Gulf Stream model–data comparisons in basin-scale subtropical Atlantic Ocean models, *Dynamics of Atmospheres and Oceans*, 32, 283-329

Hurlburt, H.E., Brassington, G.B., Drillet, Y., Kamachi, M., Benkiran, M., Bourdalle-Badie, R., Chassignet, E.P., Jacobs, G.A., Le Galloudec, O., Lellouche, J.-M., Metzger, E.J., Oke, P.R., Pugh, T.F., Schiller, A., Smedsted, O.M., Tranchant, B., Tsujino, H., Usui N. and Wallcraft, A.J. 2009: High resolution global and basin-scale ocean analyses and forecasts, *Oceanography*, 22(3), 110-127

Ingleby, B. and Huddleton, M. 2007: Quality control of ocean profiles –historical and real-time data, *J. Marine Systems*, 65, 158-175

Kallberg, P., Simmons, A., Uppala, S. and Fuentes, M. 2004. The ERA-40 archive, European Centre for Medium-range Weather Forecasts (ECMWF), ECMWF Re-Analysis Project (ERA), ERA-40 Project Report Series 17, 31 pp

Koblinsky, C.J. and Smith, N.R. Eds., 2001: Observing the oceans in the 21st Century, Uniprint, Melbourne, 604pp.

Large, W.G., Danabasoglu, G., Doney S. and McWilliams, J.C. 1997: Sensitivity to surface forcing and boundary layer mixing in a global ocean model: Annual-mean climatology, *J. Phys. Oceanogr.*, 27, 2418-2447

Martin, M.J., Hines, A. and Bell. M.J. 2007. Data assimilation in the FOAM operational short-range ocean forecasting system: A description of the scheme and its impact. *Quarterly Journal of the Royal Meteorological Society* 133:981–995.

Maximenko, N.A., Bang, B. and Sasaki, H. 2005: Observational evidence of alternating zonal jets in the world ocean, *Geophys. Res. Lett*., 32, L12607, doi:10.1029/2005GL022728.

Madec, G. 2008. NEMO Ocean Engine. *Report 27*, ISSN No. 1288-1619. Institut Pierre-Simon Laplace (IPSL), France, 197 pp.

Oke, P.R., Brassington, G.B., Griffin D.A. and Schiller, A. 2008: The Bluelink ocean data assimilation system (BODAS), *Ocean Modelling*, 21, 46-70

Oke, P.R., Brassington, G.B., Griffin D.A. and Schiller, A. 2009: Ocean data assimilation: a case for ensemble optimal interpolation, *Australian Meteorological and Oceanographic Journal*, 59, 67-76

Pascual, A., Boone, C., Larnicol G. and Le Traon, P.-Y. 2009: On the quality of real time altimeter gridded fields: comparison with in situ data, *J. Atmos. Ocean Technol*., 26, 556-569

Puri K., Xiao, Y., Sun, X., Lee, J., Engel, C., Steinle, P., Le, T., Bermous, I., Logan, L., Bowen, R., Sun, Z., Naughton, M., Roff, G., Dietachmayer, G., Sulaiman, A., Dix, M., Rikus, L., Zhu, H., Barras, V., Sims, H., Tingwell, C., Harris, B., Glowacki, T., Chattopadhyay, M., Deschamps, L., Le Marshall, J., Fraser, J., Fernon, J., Blockley, I., Sanders, C., Qi, L., Mavromatis, A., Turco, A., Sonntag, K., Howard, D., Wain, A., Warren, G., Huang, X., Zhong, A., Entel, M., Wu, X., Bridge C. and Skinner, T. 2010: Preliminary results from Numerical Weather Prediction implementation of ACCESS. *CAWCR Research Letters Issue 5*, 15-22

Ridgway, K.R. and Godfrey, J.S. 1997: Seasonal cycle of the East Australian Current, *J. Geophys. Res*., 102, C10, 22921-22936

Ridgway K.R., Dunn, J.R. and Wilkin, J.L. 2002: Ocean interpolation by four-dimensional least squares -Application to the waters around Australia, *J. Atmos. Ocean. Tech*., 19, 1357-1375

Roemmich, D., Boebel, O., Desaubies, Y., Freeland, H., Kim, K., King, B., LeTraon, P.-Y., Molinari, R., Owens, W.B., Riser, S., Send, U., Takeuchi K. and Wijffels, S. 2001: Argo: the global array of profiling floats, 248-258, in Koblinsky, J. and Smith, N. R., 2001: Observing the oceans in the 21st century, Uniprint Pty, Ltd, Melbourne.

Sandery, P. and Brassington, G.B. 2008: Upper ocean heat content in the Australian region and potential impacts on tropical cyclone intensification, *BMRC research letter*, 8, 35-43 (http://www.bom.gov.au/bmrc/pubs/researchletter/reslett_08.pdf)

Sandery, P., Brassington, G.B., Craig A. and Pugh, T. 2010a: Impacts of ocean-atmosphere coupling on tropical cyclone intensity change and ocean prediction in the Australian region, *Mon. Wea. Rev*., 138, 2074–2091. doi: 10.1175/2010MWR3101.1

Sandery, P.A., Brassington G.B. and Freeman, J. 2010b: Adaptive nonlinear dynamical initialization, *J Geophys. Res*. doi:10.1029/2010JC006260

Schiller, A., Oke, P.R., Brassington, G.B., Entel, M., Fiedler, R., Griffin, D.A. and Mansbridge, J. 2008: Eddy-resolving ocean circulation in the Asian-Australian region inferred from an ocean reanalysis effort, *Progress in Oceanography*, 76, 334-365

Seaman, R., Bourke, W., Steinle, P., Hart, T., Embery, G., Naughton, M. and Rikus, L. 1995. Evolution of the Bureau of Meteorology's Global Assimilation and Prediction System, Part 1: Analyses and Initialization, *Aust. Met. Mag*., 44, 1-18.

Smith, W.H.F. and Sandwell, D. 1962. Global seafloor topography from satellite altimetry and ship depth soundings, *Science*, 277, p.1956-1962, 1997

Taylor, A., Brassington G.B. and Nader, J. 2010: Assessment of BLUElink OMv1.0b against coastal tide gauges, *CAWCR Technical Report No. 030*, pp86.

(http://www.cawcr.gov.au/publications/technicalreports/CTR_030.pdf)

APPENDIX A OFAM2 OPTIONS

Table 13 The Modular Ocean Model version 4 namelist options used in the Ocean Forecast Australia Model version 2

Namelist	**Option**	**Value**
ocean_solo_nml	months	0
	days	5 [1]
	date_init	1990,1,1,0,0,0
	hours	0
	minutes	0
	seconds	0
	calendar	‘julian’
	dt_cpld	10800
	restart_interval	0,0,4,0,0,0 [2]
ocean_model_nml	time_tendency	'twolevel'
	vertical_coordinate	'zstar'
	dt_ocean	600
	baroclinic_split	1
	surface_height_split	1
	barotropic_split	100
	debug	.false.
	layout	8.18
data_override_nml		
fms_io_nml	threading_read	'multi'
	threading_write	'single'
	fileset_write	'single'
fms_nml	clock_grain	'LOOP'
ocean_adv_vel_diag_nml	diag_step	60
	verbose_cfl	.false.
	max_cfl_value	100.0
	large_cfl_value	10.0
ocean_advection_velocity_nml	max_advection_velocity	50
ocean_barotropic_nml	zero_tendency	.false.
	debug_this_module	.false.
	barotropic_pred_corr	.true.
	barotropic_leap_frog	.false.
	pred_corr_gamma	0.2
	smooth_eta_t_biharmonic	.false.
	smooth_eta_t_laplacian	.true.
	barotropic_time_stepping_mom4p0	.true.
	barotropic_time_stepping_mom4p1	.false.
	pbot_offset	1e-12
	vel_micom_lap	0.07
	vel_micom_bih	0.01
	truncate_eta	.true.
	eta_max	9.0

[1] Forecast cycle has days = 7.
[2] Only present in analysis cycle.

	verbose_truncate	.false.
	frac_crit_cell_height	0.25
	diag_step	10
ocean_bbc_nml	uresidual	0.05
	cdbot	1.5e-3
ocean_bbc_OFAM_nml	read_tide_speed	.false.
	uresidual2_max	1.0
ocean_bih_friction_nml	bih_friction_scheme	'general'
ocean_bih_tracer_nml	use_this_module	.false.
ocean_bihcst_friction_nml	use_this_module	.false.
ocean_bihgen_friction_nml	k_smag_iso	3.0
	k_smag_aniso	3.0
	vel_micom_iso	5.e-3
	vel_micom_aniso	5.e-3
	vel_micom_bottom	0.01
	bottom_5point	.false.
	use_this_module	.true.
ocean_convect_nml	use_this_module	.true.
	convect_full_scalar	.true.
	convect_full_vector	.false.
	convect_ncon	.false.
ocean_coriolis_nml	use_this_module	.true.
	acor	1.0
ocean_density_nml	linear_eos	.false.
ocean_domains_nml		
ocean_drifters_nml	use_this_module	.false.
	output_interval	10
ocean_form_drag_nml	use_this_module	.false.
ocean_frazil_nml	use_this_module	.false.
ocean_grids_nml	debug_this_module	.false.
ocean_increment_eta_nml	use_this_module	.false.
	days_to_increment	0
	secs_to_increment	3600
	fraction_increment	1.0
ocean_increment_tracer_nml	use_this_module	.false.
	days_to_increment	0
	secs_to_increment	3600
	fraction_increment	1.0
ocean_increment_velocity_nml	use_this_module	.false.
	days_to_increment	0
	secs_to_increment	3600
	fraction_increment	1.0
ocean_lap_friction_nml	lap_friction_scheme	'const'
ocean_lap_tracer_nml	use_this_module	.false.
ocean_lapcst_friction_nml	use_this_module	.false.
ocean_lapgen_friction_nml	use_this_module	.false.
ocean_mixdownslope_nml	use_this_module	.false.
	debug_this_module	.false.
ocean_momentum_source_nml	rayleigh_damp_exp_time	43200.0
	rayleigh_damp_exp_scale	100.0
	rayleigh_damp_exp_from_bottom	.true.
	use_this_module	.false.
ocean_nphysics_mom4p0_nml	use_this_module	.false.

	debug_this_module	.false.
ocean_nphysics_mom4p1_nml	use_this_module	.false.
ocean_nphysics_nml	use_this_module	.false.
	debug_this_module	.false.
ocean_obc_nml		
ocean_overexchange_nml	use_this_module	.false.
ocean_overflow_nml	use_this_module	.false.
	debug_this_module	.false.
ocean_passive_nml		
ocean_polar_filter_nml	use_this_module	.false.
ocean_pressure_nml		
ocean_rivermix_nml	use_this_module	.true.
	debug_this_module	.false.
	river_insertion_thickness	15.0
	river_diffusion_thickness	0.0
	river_diffusivity	0.0
	river_diffuse_salt	.false.
	river_diffuse_temp	.false.
ocean_riverspread_nml	use_this_module	.true.
ocean_sbc_nml	temp_restore_tscale	0.0
	salt_restore_tscale	30.0
	use_waterflux	.true.
	read_restore_mask	.false.
ocean_sbc_OFAM_nml	river_temp_OFAM	.false.
	restore_mask_OFAM	.false.
ocean_shortwave_csiro_nml	use_this_module	.true.
	zmax_pen	5000.0
	read_depth	.true.
ocean_shortwave_gfdl_nml	use_this_module	.false.
	debug_this_module	.false.
	read_chl	.true.
	zmax_pen	100.0
	enforce_sw_frac	.true.
ocean_shortwave_csiro_OFAM _nml		
ocean_shortwave_nml	use_this_module	.true.
	use_shortwave_gfdl	.false.
	use_shortwave_csiro	.true.
ocean_sigma_transport_nml	use_this_module	.true.
ocean_sponges_eta_nml	use_this_module	.true.
ocean_sponges_tracer_nml	use_this_module	.true.
	damp_coeff_3d	.false.
ocean_sponges_velocity_nml	use_this_module	.true.
	damp_coeff_3d	.false.
ocean_sponges_tracer_OFAM_ nml	use_adaptive_restore	.true. [3]
	use_normalising	.true.
	use_hard_thump	.false.
	athresh	0.9
	taumin	1200

[3] .false. for forecast cycle

	lambda	0.0083
	npower	1.0
	days_to_restore	1
	secs_to_restore	0
ocean_sponges_velocity_OFAM_nml	use_adaptive_restore	.true. [3]
	use_normalising	.true.
	use_hard_thump	.false.
	athresh	0.9
	taumin	1200
	lambda	0.0083
	npower	1.0
	days_to_restore	1
	secs_to_restore	0
ocean_sponges_eta_OFAM_nml	use_adaptive_restore	.true. [3]
	use_normalising	.true.
	use_hard_thump	.false.
	athresh	0.0
	taumin	1200
	lambda	0.0083
	npower	1.0
	days_to_restore	1
	secs_to_restore	0
ocean_submesoscale_nml	use_this_module	.false.
ocean_tempsalt_nml	temperature_variable	'potential_temp'
	pottemp_2nd_iteration	.true.
	reinit_ts_with_ideal	.false.
	t_min	-5.0
	t_max	55.0
	s_min	0.0
	s_max	55.0
	t_min_limit	-1.5
	t_max_limit	32.0
	s_min_limit	5.0
	s_max_limit	42.0
ocean_thickness_nml	update_dzwu_k0	.false.
	thickness_method	'energetic'
ocean_time_filter_nml		
ocean_topog_nml		
ocean_tracer_advect_nml	debug_this_module	.false.
	zero_tracer_advect_vert	.false.
	zero_tracer_advect_horz	.false.
	advect_sweby_all	.false.
ocean_tracer_diag_nml	tracer_conserve_days	1.0
	diag_step	60
	do_bitwise_exact_sum	.false.
ocean_tracer_nml	debug_this_module	.false.
	frazil_heating_after_vphysics	.true.
	zero_tendency	.false.
ocean_velocity_advect_nml		
ocean_velocity_diag_nml	debug_this_module	.false.
	diag_step	60

	energy_diag_step	60
	max_cfl_value	100.0
	large_cfl_value	10.0
ocean_velocity_nml	truncate_velocity	.false.
	truncate_velocity_value	0.2
	zero_tendency	.false.
	adams_bashforth_third	.true.
ocean_vert_chen_nml	use_this_module	.true.
	visc_cbu_limit	25.0e-4
	diff_cbt_limit	50.0e-4
	visc_con_limit	0.01
	diff_con_limit	0.1
	visc_cbu_iw	1.0e-4
	diff_cbt_iw	0.1e-4
	debug_this_module	.false.
ocean_vert_const_nml	use_this_module	.false.
ocean_vert_gotm_nml	use_this_module	.false.
ocean_vert_kpp_nml	use_this_module	.false.
ocean_vert_mix_nml	aidif	1.0
	vert_mix_scheme	'chen'
	bryan_lewis_diffusivity	.false.
ocean_vert_pp_nml	use_this_module	.true.
ocean_vert_tidal_nml	use_wave_dissipation	.false.
	use_drag_dissipation	.true.
	read_tide_speed	.false.
	read_roughness	.false.
	background_diffusivity	0.0
	background_viscosity	0.0
	drhodz_min	1e-10
ocean_xlandinsert_nml	use_this_module	.false.
	verbose_init	.true.
ocean_xlandmix_nml	use_this_module	.false.
	verbose_init	.true.
ocean_OFAM_diag_nml	do_eta_tendency	.false.
	debug_this_module	.false.

Table 14 The Modular Ocean Model version 4 namelist options used in the Ocean Forecast Australia Model version 2

APPENDIX B BODAS2 OPTIONS

Namelist	Option	Value
what_obs	assimilate_sla	.true.
	assimilate_tprof	.true.
	assimilate_sprof	.true.
	assimilate_sst	.true.
time_window	minus_eta	5.0
	plus_eta	5.0
	minus_sst	1.0
	plus_sst	1.0
	minus_ts	5.0
	plus_ts	5.0
	sla_super_ob_file	"super_sla.dat"
	sst_super_ob_file	"super_sst.dat"
	ts_super_ob_file	"super_ts.dat"
	default_super_ob_res_in_degrees	1.0
data_types	enact_ts	.false.
	bom_ts	.true.
	cars_ts	.false.
	argo_ts	.false.
	tao_ts	.false.
	ers_sla	.false.
	jason_sla	.true.
	topex_sla	.false.
	gfo_sla	.false.
	envisat_sla	.true.
	envisat_r_sla	.true.
	ctg_sla	.true.
	jason1_nrt_sla	.true.
	jason2_nrt_sla	.true.
	envisat_nrt_sla	.true.
	gfo_nrt_sla	.false.
	amsre_sst	.true.
	hr_rey_sst	.false.
	pw_cmr_sst	.false.
	pathfndr_sst	.false.
	read_amsre_asc	.false.
	avhrr_sst	.false.
	navo_sst	.true.
	amsre_l2p_sst	.false.
method	zonal_loc_len_scl_in_deg	8.0
	merid_loc_len_scl_in_deg	8.0
	vert_loc_len_scl_in_m	999999.0
	ratio_of_halo_to_len_scls	1.0
	inv_method	"petsc"
	normalise_by_obs_errors	.false.
	adaptive_domains	.true.
	approx_num_obs_per_inversion	3000

valid_ranges	valid_min_T	-1.0
	valid_max_T	40.0
	valid_min_S	0.0
	valid_max_S	40.0
	valid_min_U_inc	-2.0
	valid_max_U_inc	2.0
ensemble	n_ens	144
	alpha_ens	1.0
	iskip	2
	jskip	2
	remove_ensemble_mean	.true.
errors	RE_from_file	.true.
	RE_constant	.false.
	re_eta	0.1
	re_temp	0.0
	re_salt	0.0
	rep_error_fname	"Rep_Error.nc"
	super_ob	.true.
sla_errors	sla_min_obs_err	0.002
	e_L_age	3.0
	e_Lx	0.01
	e_Ly	0.01
	sla_qc_num_of_sigmas_check	5.0
	sla_qc_fore_innov_cut_off	1.0
	sla_qc_min_depth	200.0
t_errors	sst_min_obs_err	0.05
	t_sst_err	0.25
	t_amsre_sst_err	0.25
	t_rey_sst_err	1.0
	t_cmar_sst_err	0.25
	t_pathfndr_err	0.25
	t_path_nrt_err	0.5
	t_navo_err	0.25
	t_amsre_l2p_err	0.25
	sst_qc_fore_innov_cut_off	6.0
	sst_qc_min_depth	10.0
	t_ctd_instr	0.1
	t_xbt_instr	0.2
	t_Lx	0.01
	t_Ly	0.01
	t_Lz	5.0
	t_L_age	3.0
	t_rms_ratio	0.2
	t_qc_sigma	100.0
	t_qc_num	0
s_errors	s_ctd_instr	0.05
	s_Lx	0.01
	s_Ly	0.01
	s_Lz	5.0
	s_L_age	3.0
	s_rms_ratio	0.2
	s_qc_sigma	100.0
	s_qc_num	0

purpose	use_diagnosed_alpha	.false.
	load_balance	.true.
what2correct	calc_eta	.true.
	calc_t	.true.
	calc_s	.true.
	calc_uv	.true.
	update_eta	.false.
	update_t	.false.
	update_s	.false.
	update_uv	.false.
	bgf_is_daily_mean	.true.
	bgf_is_climatology	.false.
	store_increment	.true.
	store_analysis	.true.
	dynamic_height	.false.
	convect_adj	.true.
	num_time_steps	1
filenames	fname_grid	"grid_spec.nc"
	fname_anom	"ENS_001_eta_t.nc"
	fname_eta_restart	"ocean_freesurf.res.nc"
	fname_eta_mean	"eta_mean.nc"
	fname_eta_bg	"ocean_eta.nc"
	fname_ts_restart	"ocean_temp_salt.res.nc"
	fname_temp_bg	"ocean_temp.nc"
	fname_salt_bg	"ocean_salt.nc"
	fname_u_bg	"ocean_u.nc"
	fname_v_bg	"ocean_v.nc"
	fname_vel_restart	"ocean_velocity.res.nc"
	fname_eta_rms	"rms_eta_t.nc"
	fname_temp_rms	"rms_temp.nc"
	fname_salt_rms	"rms_salt.nc"
model	modeltype	"OFAM"
grid	gridtype	"RECTANGULAR"
	fname_gridmap	"grid_spec.nc"
verbosity	verbose	1

APPENDIX C CONTINUITY OF FLUXES ACROSS LAND-SEA MASKS

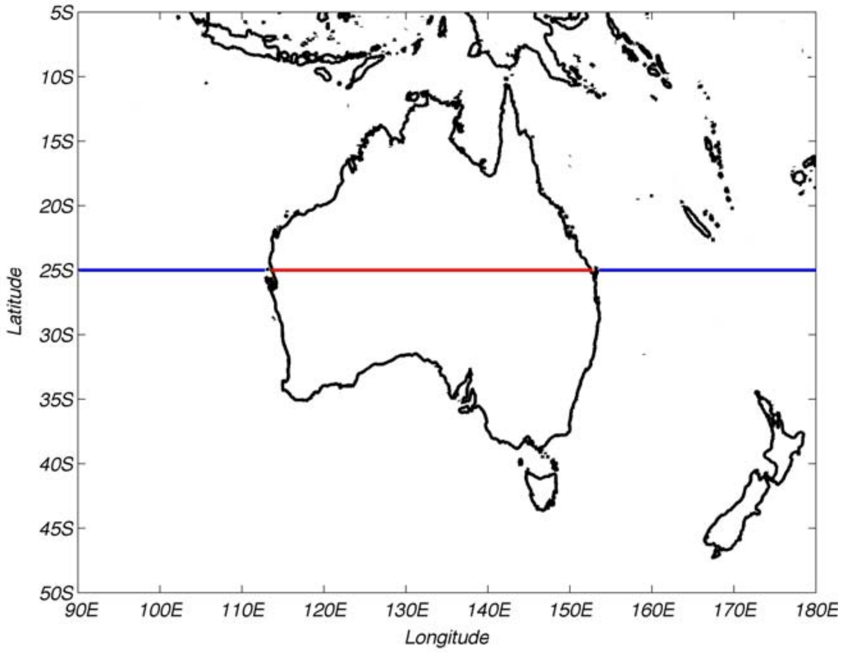

Fig. 57. Zonal section intersecting the Australian coastline that is used to determine the continuity of fluxes across land-sea boundaries

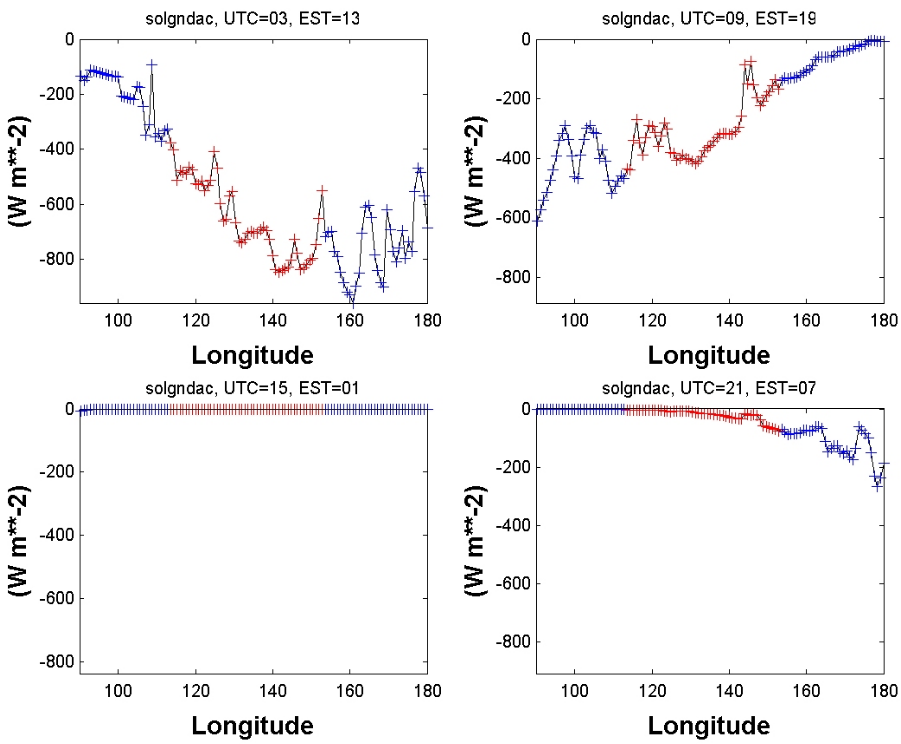

Fig. 58. Net downward shortwave radiation from GASP along a zonal section 25S for 12th February 2006. Fluxes corresponding to land (sea) mask are represented by red (blue) line and crosses.

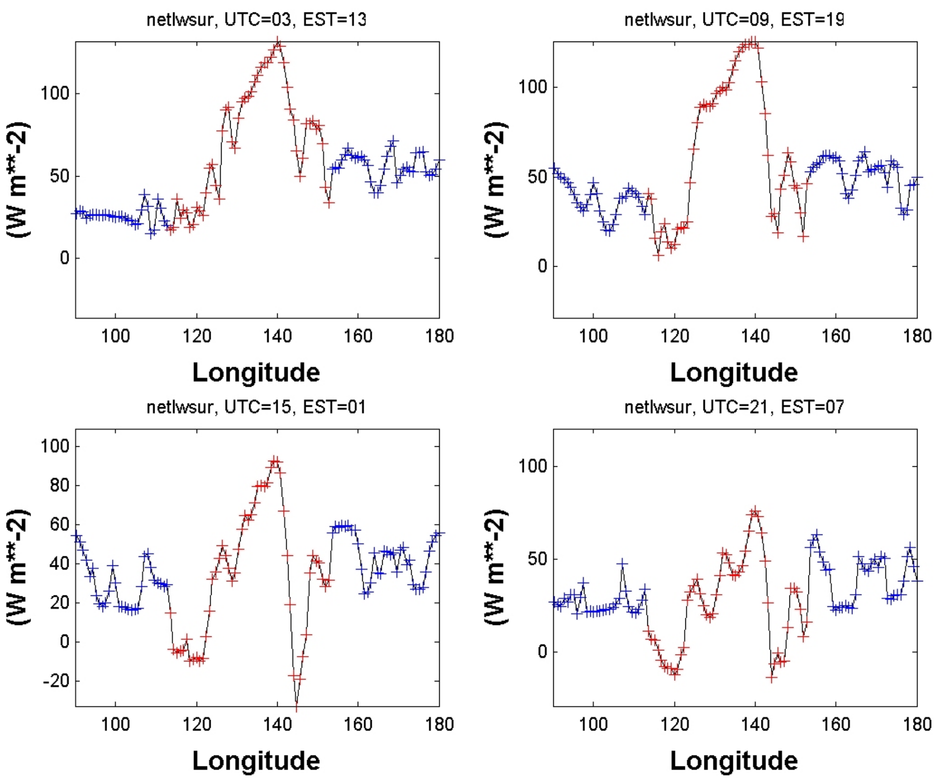

Fig. 59. Net longwave radiation from GASP along a zonal section 25S for 12th February 2006. Fluxes corresponding to land (sea) mask are represented by red (blue) line and crosses.

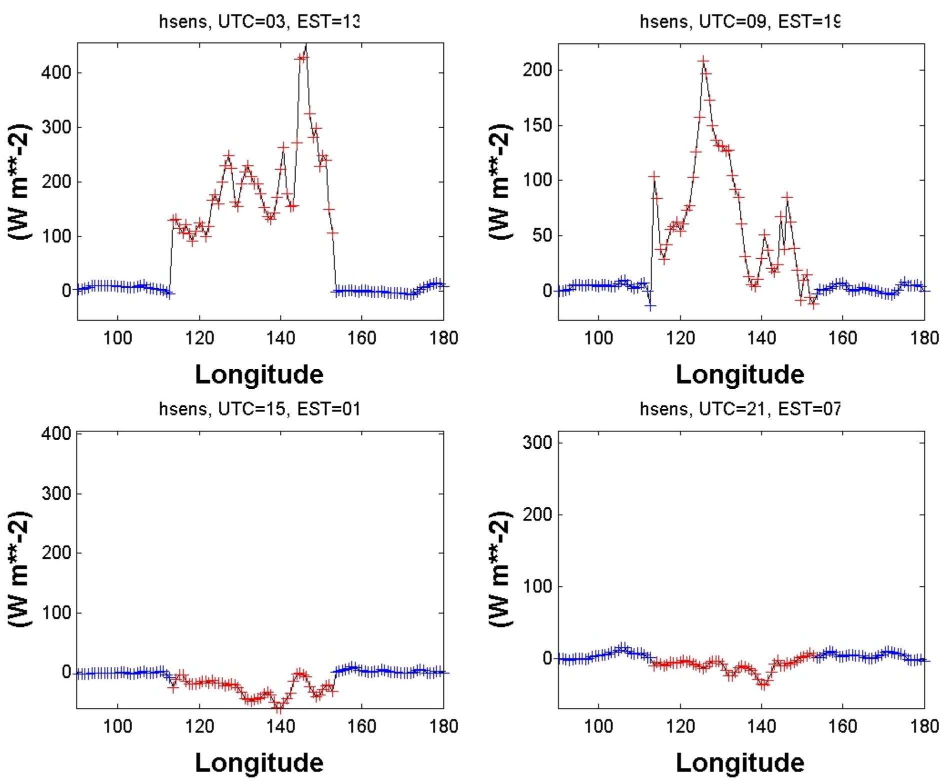

Fig. 60. Sensible heat flux from GASP along a zonal section 25S for 12th February 2006. Fluxes corresponding to land (sea) mask are represented by red (blue) line and crosses.

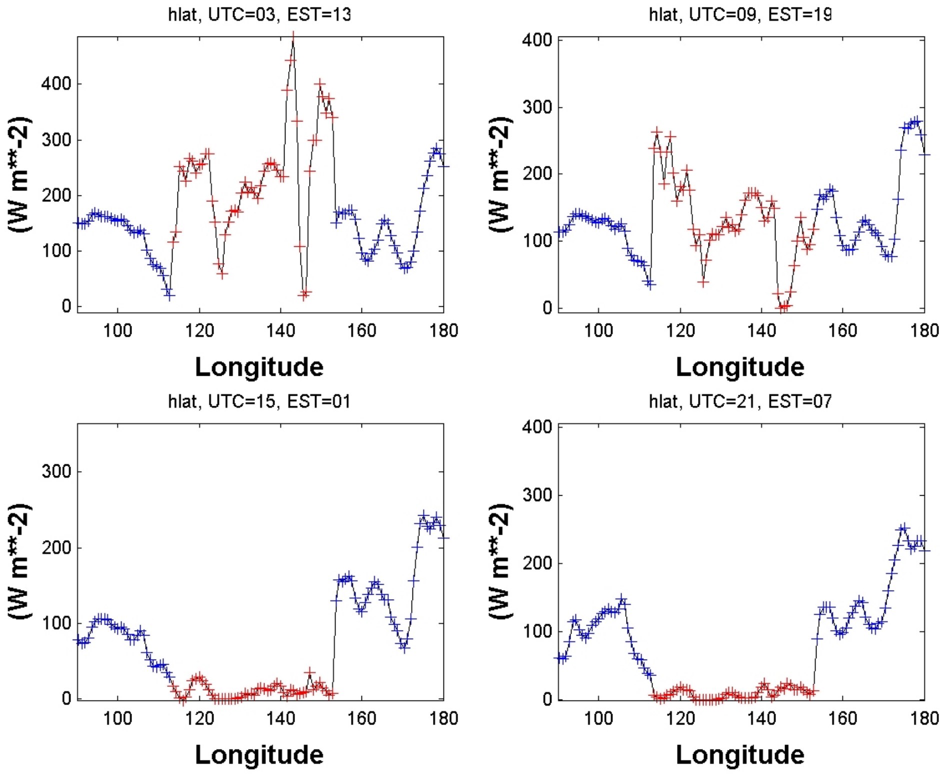

Fig. 61. Latent heat flux from GASP along a zonal section 25S for 12th February 2006. Fluxes corresponding to land (sea) mask are represented by red (blue) line and crosses.

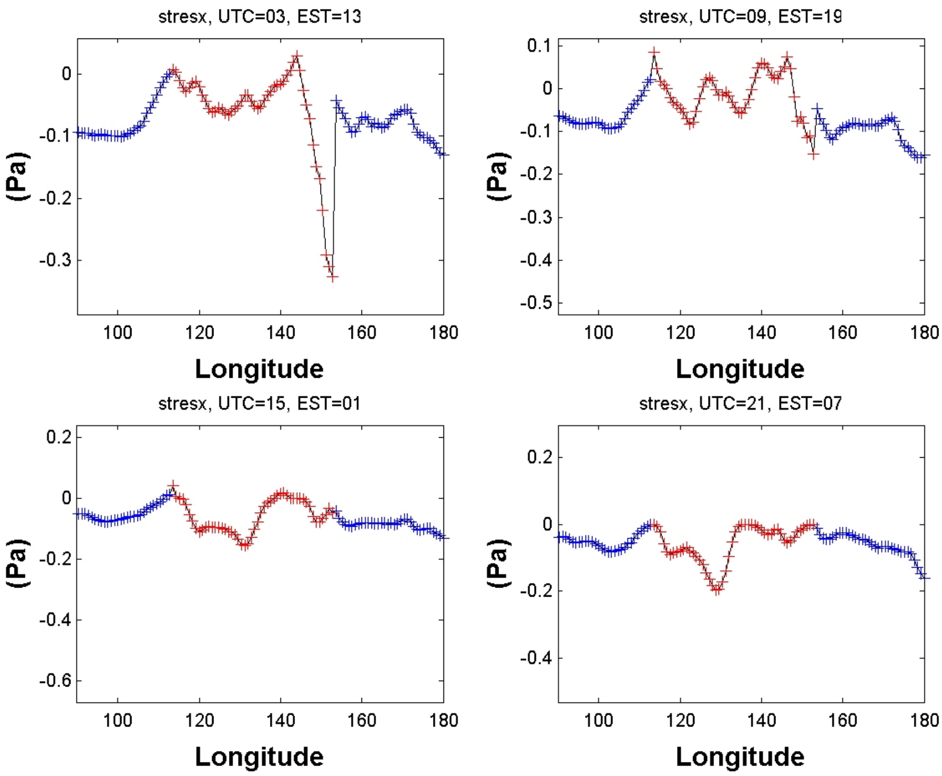

Fig. 62. Zonal stress from GASP along a zonal section 25S for 12th February 2006. Fluxes corresponding to land (sea) mask are represented by red (blue) line and crosses.

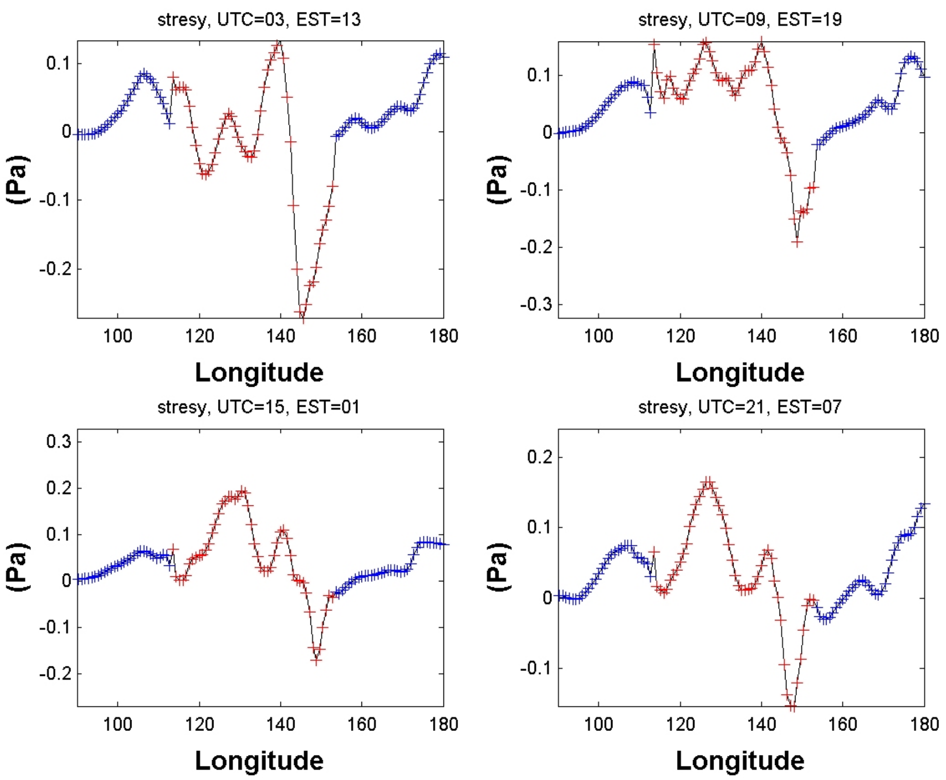

Fig. 63. Meridional stress from GASP along a zonal section 25S for 12th February 2006. Fluxes corresponding to land (sea) mask are represented by red (blue) line and crosses.

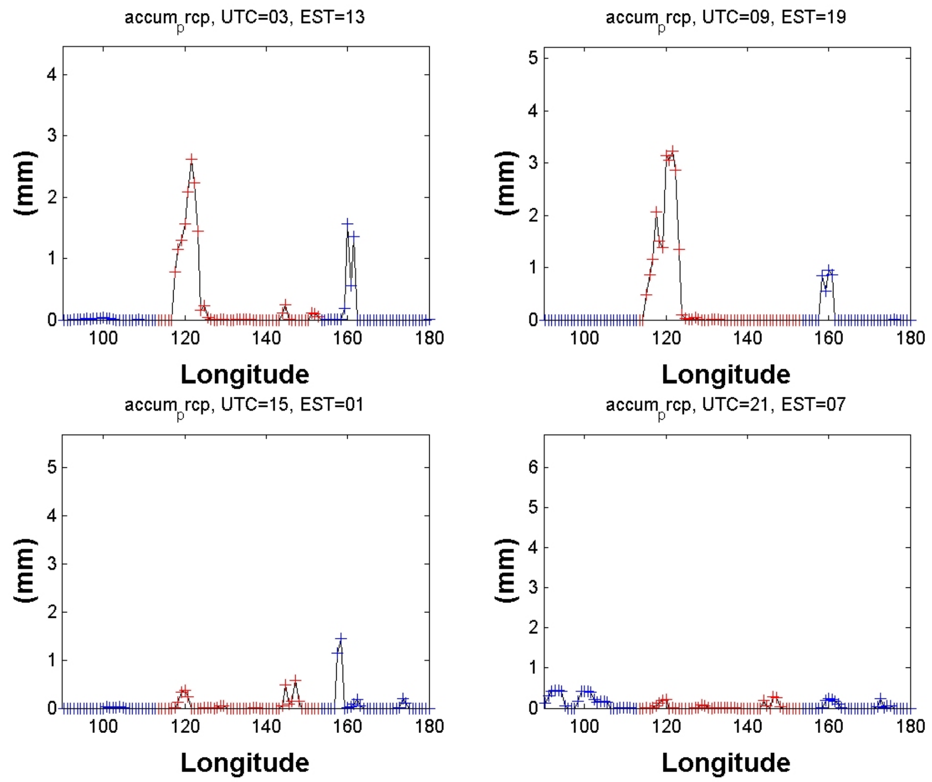

Fig. 64. Total precipitation from GASP along a zonal section 25S for 12th February 2006. Fluxes corresponding to land (sea) mask are represented by red (blue) line and crosses

APPENDIX D *IN SITU* QUALITY CONTROL METADATA

Name	Description	Dimension	Attributes
PRES_BLUELINK	The pressure used in the BLUElink> quality control system Equivalent to PRES (or PRES_ADJUSTED when this exists)	N_PROF,N_LEVELS	decibar
TEMP_BLUELINK	The temperature used in the BLUElink> quality control system Equivalent to TEMP (or TEMP_ADJUSTED when this exists)	N_PROF,N_LEVELS	Degrees C (In situ temperature)
TEMP_BLUELINK_QC	Quality control summary test determined by combining the results of the applied tests and includes the final ratio test Logic of test defined in manual	N_PROF,N_LEVELS	Logical 0 = pass, 1 = fail, -999 = FillValue
TEMP_BODAS_QC	The temperature used in the OceanMAPS analysis. Only TEMP_BLUELINK values assigned in TEMP_BLUELINK_QC state is pass. Missing_value	N_PROF,N_LEVELS	Degrees C (In situ temperature)

	otherwise.		
PSAL_BLUELINK	The salinity used in the BLUElink> quality control system Equivalent to PSAL (or PSAL_ADJUSTED when this exists)	N_PROF,N_LEVELS	psu
PSAL_BLUELINK_QC	Quality control summary test determined by combining the results of the applied tests and includes the final ratio test Logic of test defined in manual	N_PROF,N_LEVELS	Logical 0 = pass, 1 = fail, -999 = FillValue
PSAL_BODAS_QC	The pratical salinity used in the OceanMAPS analysis. Only PSAL_BLUELINK values assigned in PSAL_BLUELINK_QC state is pass. Missing_value otherwise.	N_PROF,N_LEVELS	psu
TEMP_CLIMATOLOGY_MEAN	Climatological temperature interpolated to the position and level defined for each level. The temperature are converted to in situ temperatures corresponding to pressure levels of the argo Values are produced for all profiles with sensible locations and pressures regardless of the quality control flags assigned to the profile. The highest temporal resolution permitted by the	N_PROF,N_LEVELS	Degrees C (In situ temperature)

	climatology source is used (i.e., monthly <200m) The climatology source is defined for each profile by CLIMATOLOGY_SOURCE.		
TEMP_CLIMATOLOGY_STD	Climatological temperature standard deviation interpolated to the position and level defined for each level The standard deviations are smoothed vertically and adjusted by a constant so that the deviations are greater or equal to all original values. The standard deviation is typically provided relative to the annual mean temperature Note the change in std. dev. in potential temperature or in situ are assumed negligible	N_PROF,N_LEVELS	Degrees C (Potential temperature)
PSAL_CLIMATOLOGY_MEAN	See TEMP_CLIMATOLOGY_MEAN (note no potential adjustment required)	N_PROF,N_LEVELS	psu
PSAL_CLIMATOLOGY_STD	See TEMP_CLIAMTOLOGY_STD	N_PROF,N_LEVELS	psu
CLIMATOLOGY_SOURCE	Climatological tests are performed relative to the best available sources (e.g., CARS 2005) The source is referred to by a	N_PROF	nondimensional flag_value = 1,2 flag_meaning = ‘CARS 2005’ WOA 2001’

QC_PERFORM_TEST	An array of 32bit flags that determines if each test has been applied. The test associated with each bit is outline below. Tests may or may not be applied according to the availability of dependent data or combinations of variables (e.g., computing density). A 32 bit integer is used to represent up to 32 individual tests Bit n = 0 Test not applied Bit n = 1 Test was applied	N_PROF, N_LEVELS	
QC_BLUELINK_FLAGS	An array of 32bit flags that determine the status of each test. The test associated with each bit is outlined below. A 32 bit integer is used to represent up to 32 individual tests Bit n = 0 (Pass) Bit n = 1 (Fail)	N_PROF, N_LEVELS	
HISTORY_BLUELINK_DATE	Date the history record was created	N_BLUELINK, N_PROF, DATE_TIME	long_name = "Date the history record was created" conventions = "YYYYMMDDHHMISS" _FillValue = " "

HISTORY_BLUELINK_SOFTWARE	Description of the software used to process the file	N_BLUELINK, N_PROF, STRING4	long_name=”Name of software which performed action” Conventions=”Institution dependent” _FillValue = “ ”
HISTORY_BLUELINK_SOFTWARE_RELEASE	Version/release of software	N_BLUELINK, N_PROF, STRING4	long_name="Version/release of software which performed action"
HISTORY_BLUELINK_DATE	Date the history record was created	N_BLUELINK, N_PROF, DATE_TIME	long_name = "Date the history record was created" conventions = "YYYYMMDDHHMISS" _FillValue = " "

The Centre for Australian Weather and Climate Research is a partnership between CSIRO and the Bureau of Meteorology.